UNIVERSITAT POLITÈCNICA
DE CATALUNYA
BARCELONATECH

High efficiency sensorless fault tolerant control of permanent magnet assisted synchronous reluctance motor

Tomasz Dobromir Michalski

High Efficiency Sensorless Fault Tolerant Control of Permanent Magnet Assisted Synchronous Reluctance Motor

Thesis submitted in partial fulfillment of the requirement for the PhD degree issued by the Universitat Politècnica de Catalunya, in its Electronic Engineering Program

Tomasz Dobromir Michalski

Director: *Dr. Jose Luis Romeral Martínez*

February 2021

To my beloved wife and children

Abstract

In the last decades, the development trends of high efficiency and compact electric drives on the motor side focused on Permanent Magnet Synchronous Machines (PMSMs) equipped with magnets based on the rare-earth elements. The permanent magnet components, however, dramatically impact the overall bill of materials of motor construction. This aspect has become even more critical due to the price instability of the rare-earth elements. This is why the Permanent Magnet Assisted Synchronous Reluctance Motor (PMaSynRM) concept was brought to the spotlight as it gives comparable torque density and similar efficiencies as PMSM although at a lower price accredited for the use of magnets built with ferrite composites. Despite these advantages, PMaSynRM drive design is much more challenging because of non-linear inductances resulting from deep cross saturation effects.

It is also true for multi-phase PMSM motors that have gained a lot of attention as they proportionally split power by the increased number of phases. Furthermore, they offer fault-tolerant operation while one or more phases are down due to machine, inverter, or sensor fault. The number of phases further increases the overall complexity for modeling and control design. It is clear then that a combination of multi-phase with PMaSynRM concept brings potential benefits but confronts standard modeling methods and drive development techniques.

This Thesis consists of detailed modeling, control design, and implementation of a five-phase PMaSynRM drive for normal healthy and open phase fault-tolerant applications. Special emphasis is put on motor modeling that comprises saturation and space harmonics together with axial asymmetry introduced by rotor skewing. Control strategies focused on high efficiency are developed and the position estimation based on the observer technique is derived. The proposed models are validated through Finite Element Analysis (FEA) and experimental campaign. The results show the effectiveness of the elaborated algorithms and methods that are viable for further industrialization in PMaSynRM drives with fault-tolerant capabilities.

Keywords - Permanent Magnet Machines (PMSM), Permanent Magnet Assisted Synchronous Reluctance Machines (PMaSynRM), Finite Element Analysis (FEA), cross saturation, space harmonics, skew, multiphase machines, vector control, fault tolerance

Resumen

En últimas décadas, las tendencias de desarrollo de accionamientos eléctricos compactos y de alta eficiencia en el lado del motor se centraron en las maquinas síncronas de imanes permanentes (PMSM) equipadas con imanes basados en elementos de tierras raras. Sin embargo, los componentes de imán permanente impactan dramáticamente en el coste de construcción del motor. Este aspecto se ha vuelto aún más crítico debido a la inestabilidad de precios de los elementos de tierras raras. Esta es la razón por la que el concepto de motor de reluctancia síncrona asistido por imán permanente (PMaSynRM) se ha tomado en consideración, ya que ofrece una densidad de par comparable y eficiencias similares a las de PMSM, aunque a un precio más bajo acreditado para el uso de imanes construidos con compuestos de ferritas. A pesar de estas ventajas, el diseño del drive PMaSynRM resulta muy complejo debido a las inductancias no lineales que resultan de los efectos de saturación cruzada profunda.

Esto también es cierto para los motores PMSM polifásicos que han ganado mucha atención en los últimos años, en los que se divide proporcionalmente la potencia por el mayor número de fases. Además, ofrecen operación tolerante a fallas mientras una o más fases están inactivas debido a fallas en la máquina, el inversor o el sensor. Sin embargo, el número de fases aumenta aún más la complejidad general del diseño de modelado y control. Está claro entonces que una combinación de multifase con el concepto PMaSynRM tiene beneficios potenciales, pero dificulta los métodos de modelado estándar y las técnicas de desarrollo del sistema de accionamiento.

Esta tesis consiste en el modelado detallado, el diseño de control y la implementación de un drive PMaSynRM de cinco fases para aplicaciones normales en buen estado y tolerantes a fallas de fase abierta. Se pone especial énfasis en el modelado del motor que comprende la saturación y los armónicos espaciales junto con la asimetría axial introducida por la inclinación del rotor. Se desarrollan estrategias de control enfocadas a la alta eficiencia y se deriva la estimación de posición basada en la técnica del observador. Los modelos propuestos se validan mediante Análisis de Elementos Finitos (FEA) y resultados experimentales. Los resultados muestran la efectividad de los algoritmos y métodos elaborados, que resultan viables para la industrialización de unidades PMaSynRM con capacidades tolerantes a fallas.

Palabras clave - Máquinas de imán permanente (PMSM), Máquinas de reluctancia síncrona asistidas por imán permanente (PMaSynRM), Análisis de elementos finitos (FEA), saturación cruzada, armónicos espaciales, sesgo, máquinas polifásicas, control vectorial, tolerancia a fallas

Acknowledgement

I would like to express my sincere appreciation to the director of this thesis and head of MCIA research group Dr. Luis Romeral for his invaluable guidance and precious advice throughout the development of this thesis. I am very grateful for his continuous trust in this study.

My acknowledgment also goes to Dr. Gerardo Mino for a warm reception, encouragement, and inspiration during my research stays in Benemérita Universidad Autónoma de Puebla in Mexico.

I would also like to thank Dr. Antoni Garcia for introducing and integrating me into the group of MCIA. My gratitude also goes to other professors, colleagues, and friends from Universitat Politecnica de Catalunya that supported me along with this research conduct.

My special heartfelt appreciation to my family, especially my beloved wife and children for patience, liveliness, and happiness.

Contents

List of figures

List of tables

Acronyms

DSC	Digital Signal Controller
DSP	Digital Signal Processor
DTC	Direct Torque Control
EKF	Extended Kalman Filter
EMF	Electromotive Force
EV	Electric Vehicle
FEA	Finite Element Analysis
FEM	Finite Element Model
FOC	Field Oriented Control
HIL	Hardware In the Loop
IM	Induction Motor
IPMSM	Interior-mounted Permanent Magnet Synchronous Motor
MEC	Magnetic Equivalent Circuit
MMF	Magneto Motive Force
MTPA	Maximum Torque Per Ampere
MTPV	Maximum Torque Per Voltage
PHEV	Plug in Hybrid Electric Vehicle
PI	Proportional Integral (regulator)
PM	Permanent Magnet
PMaSynRM	Permanent Magnet Assisted Synchronous Reluctance Motor
PMSM	Permanent Magnet Synchronous Motor
PWM	Pulse Width Modulation
RE	Renewable Energy
RN	Reluctance Netowrk
SIL	Software In the Loop
SPMSM	Surface-mounted Permanent Magnet Synchronous Motor
SRM	Synchronous Reluctance Motor
SVM	Space Vector Modulation
VR	Virtual Reluctance
VSD	Variable Speed Drive

Nomenclature

m	Number of phases	-
R_s	Stator phase resistance	Ω
U_d	*d*-axis voltage	V
U_q	*q*-axis voltage	V
U_x	Stator *x*-th phase to neutral point voltage	V
i_d	*d*-axis current	A
i_q	*q*-axis current	A
i_{d1} , i_{q1}	*dq*-axes flux linkages of the *1st* harmonic	A
i_{d3} , i_{q3}	*dq*-axes flux linkages of the *3rd* harmonic	A
i_x	Stator *x*-th phase voltage	A
$\vec{I}_{dq1(xx)}$	Current space vector of the *x*-th slice and seen by the *x*-th slice	A
ψ_d	*d*-axis flux linkage	Wb
ψ_q	*q*-axis flux linkage	Wb
ψ_{d1} , ψ_{q1}	*dq*-axes flux linkages of the *1st* harmonic	Wb
ψ_{d3} , ψ_{q3}	*dq*-axes flux linkages of the *3rd* harmonic	Wb
ψ_x	Flux linkage of the *x*-th phase	Wb
$\vec{\psi}_{(xx)}$	Flux linkage space vector of the *x*-th slice and seen by the *x*-th slice	
ω_r	Rotor angular electrical velocity	Rad/s
ω_m	Rotor angular mechanical velocity	Rad/s
θ_r	Rotor angular position	Rad
P_n	Rated power	W
$I_{\max}$	Maximum RMS current	A
V_{dc}	DC-link voltage	V

n_n	Based angular speed	rpm
L_d	*d*-axis inductance	H
L_q	*q*-axis inductance	H
L_{d1} , L_{q1}	*dq*-axes inductances of the 1^{st} harmonic	H
L_{d3} , L_{q3}	*dq*-axes inductances of the 3^{rd} harmonic	H
ψ_{PMq}	Permanent magnet flux component in q-axis	Wb
ψ_{PMq1} , ψ_{PMq3}	*dq*-axes permanent magnet flux of the 1^{st} and 3^{rd} harmonics	Wb
ψ_{PMnew}	Virtual constant permanent magnet flux	Wb
p	Number of pole pairs	-
T_e	Electromagnetic torque	Nm
T_L	Load torque	Nm
T_n	Rated torque	Nm
T_{e1} , T_{e1}	Torque of the 1^{st} and 3^{rd} harmonics	Nm
$T_{e(x)}$	Electromagnetic torque of the *x*-th skew segment	Nm
J	Moment of inertia	kgm^2
B	Friction factor (viscous)	-
l_{stack}	Active stack length	mm
D_{so}	Stator outer diameter	mm
D_{ro}	Rotor outer diameter	mm
d_{gap}	Airgap length	mm
N	Number of slots	-
β	Skew angle	rad
$\Re$	Magnetic reluctance	H^{-1}
F	Magneto-motive force	A
$\Re_{dn}$	*d*-axis virtual reluctance of the *n*-th harmonic	H^{-1}

$\Re_{qn}$	q-axis virtual reluctance of the n-th harmonic	H^{-1}
$\Re_{x}$	x-th phase virtual reluctance	H^{-1}

1

1. Introduction

This chapter outlines the main content of the thesis. The research topic is introduced, the research problem is formulated and the hypotheses are stated. Consequently, the research objectives are identified, followed by the thesis outline with a summary of each chapter.

CONTENTS:

1.1. Research topic

Permanent Magnet Synchronous Machines (PMSM) have become predominant in many branches of the industry in the early 21st century [3]. The trends of sustainable and environmentally friendly growth reinforced the need for very high efficiency and compact electro-mechanical conversion systems [4]. PMSMs offer high efficiency, high torque and energy density, and reliability. Due to these appealing features, they have been gaining volumes in propulsion systems such as in electric traction and electric vehicles (EV) drives [5]–[7], renewable energy (RE) sources, household appliances, power tools, to mention just a few of vast application types with PMSM motors.

The use of magnets based on rare-earth elements strongly impacts the overall bill of materials [16]. It is caused by the global price instability of these components. Followed by concerns about the shortage of supply, a Permanent Magnet Assisted Synchronous Reluctance Motor (PMaSynRM) has been put into the spotlight [17], [18]. It offers similar characteristics in terms of efficiency and energy density. PMaSynRMs are essentially rare-earth-free motors equipped with magnets based on ferrite composites [19]. Because of the wide availability of these resources the risks concerning supply chains can be mitigated [10]. However, PMaSynRM is much more challenging in terms of control algorithm development due to cross saturations.

In some high power systems, such as in ship propulsion or aerospace applications the reliability of drive becomes even more critical [8], [9]. Furthermore, the employment of three-phase PMSM machines is limited due to constraints arising from operating voltages and currents of power electronic switches [15]. This restriction was a motivating factor for the multi-phase motor to be invented [11]. In this kind of machine, power is split between a higher number of phases [12]. Additionally, the electromagnetic torque can be still generated even with some failures in the drive chain that lead to single or multiple open phase operations [13], [14].

This thesis presents the research about problems that emerged from the implementation of PMaSynRM motors in multi-phase drive systems. The motor modeling is studied, the issues arising from the non-linear aspects of cross saturation and space harmonics are addressed for three-phase and extended to five-phase PMaSynRM. A novel model, that comprises the aforementioned phenomena together with axial asymmetry introduced by skewing, is proposed, implemented, and developed. Then, high-efficiency control strategies considering Maximum Torque Per Ampere (MTPA) are derived. The effectiveness of the proposed techniques is verified versus Finite Element Analysis (FEA) and experimental tests with a prototype machine in healthy and open phase conditions. The fault tolerance is considered also regarding position sensor malfunctioning. Thus, an approach for position estimation is mathematically elaborated leading to sensorless control. The next sections present in detail the research stages carried out during the development of this thesis.

1.2. Research problem

Permanent Magnet Assisted Synchronous Reluctance Motor (PMaSynRM) has been initially proposed as Interior Permanent Magnet Synchronous Motor (IPMSM) with a transversally laminated rotor [20] and it has become very attractive in the last years because of high efficiencies, compactness, reliability, and its low cost [16]–[18]. Hence, PMaSynRMs in many applications are considered as a replacement for more expensive PMSM constructions [17], [19]. These motors, however, intrinsically exhibit anisotropy in the rotor due to the introduction of flux barriers and additional magnets saturate iron bridges. Because of the substantial armature reaction, they suffer from deep saturation [20]. These phenomena result very challenging to be included in analytical modeling for control algorithm design and drive development.

The conventional d-q model, well known in the literature, is valid for motors with constant inductances and PM flux only [1],[2]. Finite Element Analysis is widely adopted for geometrical optimization and performance prediction [36], [16]. While it requires a high computational burden, other fast and precise models were reported. For instance, Magnetic Equivalent Circuits (MECs) are an interesting option although for simple rotor structures only [21]–[24]. There are approaches based on variable inductance estimations [25] or modified d-q two-axis model [26]–[28] that considers nonlinear inductances. To date, the inverted flux map nonlinear model has become the state of the art for three-phase PMSM motors [29]–[31]. It requires identification of current dependent flux maps that are consequently inverted and projected in the motor model.

The multi-phase motors offer clear benefits in terms of power division [11] and fault-tolerant capability [8],[9]. There are solutions of Variable Speed Drives (VSD) established with vector control of polyphase PMSMs with respective multi-phase modulation techniques based on multiple d-q spaces concept [32], [33]. Multi-phase motors bring additional complexity caused by the decoupling of multiple air-gap field harmonics [8]. Regulation of individual MMF harmonics is possible for multiphase motors with constant inductances [34], [35] but was not yet addressed for multiple cross saturating motors such as PMaSynRM. It is recognized that before-mentioned flux map inversion is feasible in 2D or 3D d-q models however it is not viable for a higher number of dimensions that are intrinsically present in multi-phase machines.

The purpose of this thesis is to study the combination of PMaSynRM motor and multi-phase drive concept on a five-phase PMaSynRM prototype comprising modeling and implementation. The motor behavior with space harmonics, saturation phenomena, and axial asymmetry introduced by rotor skewing are in the focus of this research. It will propose a new high fidelity rapid models in 5D and 6D that are practically feasible and do not require flux map inversion. The model will be extended from three to five-phase motor and applied for control in healthy and open phase conditions. Maximum Torque Per Ampere

(MTPA) control is derived based on these models. Further, the effectiveness of a sensorless application will be discussed.

1.3. Hypotheses

Regarding the previous discussion, the general hypothesis is that the PMaSynRM motor can be considered as a replacement for classical PMSM in many multiphase electric drive applications due to power density, efficiency, and cost advantages. However, the implementation of multiphase PMaSynRM induces a new research topic that requires exploration of a novel solution. Following this rationale, the hypotheses have been formulated as:

- Development of PMaSynRM precise model comprising cross-saturations is crucial for the derivation of optimal control strategies towards high efficiency in a wide speed range.
- Incorporation of nonlinear cross-saturation in multi-phase PMaSynRM machine modeling is essential to determine the Maximum Torque per Ampere (MTPA) control approach.
- Multiphase detailed drive behavior in healthy and open phase conditions requires a high fidelity model that includes saturations, space harmonics, and skewing, when applicable.
- Vector control and sensorless multiphase PMaSynRM drive can be studied in transient and steady-state regimes provided analytical model accuracy with close to Finite Element Analysis (FEM) precision.

In consequence,

A novel, fast nonlinear model for multi-phase PMasynRM, that includes space harmonics and cross saturations, will improve multiphase healthy and faulty drive analysis and lead to high-efficiency drive development.

1.4. Aim and objectives

To provide an assessment of the research problem and address the research hypotheses, the main aim of this thesis is to design and develop high efficiency five-phase PMaSynRM drive and evaluate its behavior in static and dynamic conditions within healthy and faulty scenarios.

The drive analysis has to be performed under a solid analytical model basis that will offer the best compromise between precision (thus reflecting the prototype motor behavior in the most accurate way possible) and computational load. Then, rapid control analysis and development can be realized without precision loss.

Then, to accomplish the purpose of this thesis, the specific objectives are formulated:

a) First, the analysis of the conventional three-phase PMaSynRM model with constant inductances and permanent magnet flux linkage. The objective includes the revision of classic Field Oriented Control (FOC) with linear PI regulators and MTPA control strategy derived from the constant parameter model.

b) Compose a model of a five-phase PMaSynRM with constant parameters established for the first and third harmonic air-gap field decoupling, close control loops for both harmonics, and apply state of the art Pulse Width Modulation (PWM) technique for a five-phase inverter.

c) Build up a model of three-phase PMaSynRM with saturation and space harmonics based on 2D and 3D flux map extraction via Finite Element Analysis (FEA) identification and mathematical post inversion. Verify feasibility and apply this concept for the five-phase PMaSynRM with 4D and 5D maps. Propose methodology to correct maps and demonstrate the effectiveness of the proposed method with simulation and experimental tests. Compute high-efficiency control trajectories and apply them to the developed drive.

d) Derive a 6D flux map model that is able to accurately predict five-phase PMaSynRM motor behavior under single open phase and double open phase (adjacent and non-adjacent) scenarios. Run test campaign for experimental validation.

e) Develop a new fast and precise model that avoids flux map inversion by the transformation of flux maps to “virtual reluctance” maps. Corroborate simulation waveforms against FEA and test bench results.

f) Analyze the effectiveness of the developed models to define precise MTPA control, even in sensorless operation.

1.5. Thesis outline

To cover the defined objectives and properly assess the formulated hypotheses, the thesis will be organized as follows:

Chapter 2 shows a description of the three-phase and five-phase PMaSynRM drive, motor model with **constant inductances**, its advantages, and drawbacks. It also presents the design and implementation of the FOC control with conventional state of the art PWM technique.

Chapter 3 consists of the derivation of high accuracy flux map models of three-phase and five-phase PMaSynRM comprising **cross saturations, space harmonics, and cogging torque**. It shows hot to identify the maps and implement them in the analytical model. The concept is realized in multi-two-axes planes and natural stator phase reference for healthy and faulty motor analysis respectively. Finally, FEA validation is provided for both healthy and open phase conditions. Vector control with a high-efficiency **MTPA control strategy** is developed and implemented.

Chapter 4 deals with flux map correction due to axial asymmetry introduced by **rotor skewing**. Two methods are proposed to account for segmented rotor construction in the multi-plane and natural reference frame models. The simulation results are corroborated with FEA and with experimental tests performed in the test bench with the manufactured five-phase PMaSynRM prototype.

Chapter 5 presents a novel model established with the transformation of the flux maps to **"virtual reluctance" maps**. The techniques to avoid singularities and achieve stable simulations are discussed. The performance of the proposed model is evaluated with FEA and experimental analysis is provided.

Chapter 6 introduces a **sensorless PMaSynRM** drive design that is constructed with a rotor position and velocity observer based on the Kalman Filter structure developed on the model with constant parameters. Then, the projection on the saturating PMaSynRM model is implemented followed by a discussion of the parameter sensitivity.

Chapter 7 contains conclusions drawn from the thesis and future work initiated by this research.

Chapter 8 informs about thesis dissemination, published papers, and collaboration in public and private research projects in the scope of the thesis.

2

2. Conventional modeling and control of multiphase PMaSynRM motor

This chapter constitutes simulations of a three-phase and five-phase PMaSynRM drive, setup motor models established with constant inductances, and constant flux generated by permanent magnets. Then, FOC control is implemented with MTPA control strategy, linear current control, and classical PWM modulation technique. The advantages and limitations of this approach are discussed.

CONTENTS:

2.1. Review of electrical drive technologies

The electrical drives are the systems of electrical machines and other electric and electronic devices that permit to control the speed of rotation. A drive consists of a source, power converter, motor, load, sensors, and control and command units. The AC motor is the actuator of the electrical drive and its performance plays important role in the overall drive operation. Fig. 2.1 shows the general classification of the AC motors and an example of a special classification concerning EV application, it is clear that a variety of motor types can be employed. From the note of the history first drives were built with DC motors. Their main advantage is that they are practically the simplest ones to construct although poor efficiency and short period maintenance are practically disadvantageous. The modern control methods are to some extent equivalent to DC motor control [2].

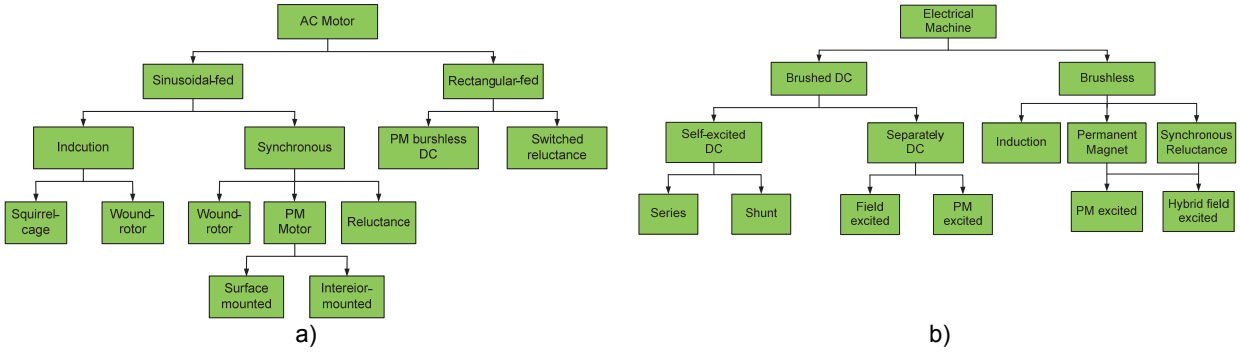

Figure 2.1. Classification of AC machines, a) general, b) with respect to EV application

However, induction machines (IMs) have become more important because of the reliability and inexpensive bill of materials in comparison to other units. These motors are simple in construction, robust, and able to operate in harsh conditions (pollution, explosive) contrary to DC machines. The absence of commutator and brushes makes the maintenance very low and the lifetime longer. This is why IM became replacing DC motors. However, at low loads, the power factor and efficiency are very low. There are some studies on control to improve IM efficiency [37], [38]. The other disadvantage is the small starting torque. The soft-start methods and first vector control were developed for induction machines in 1971 by Hasse and Blaschke [39] resulting in a very good performance.

Synchronous Machines (SM) and especially PMSMs with permanent magnets (no excitation field winding and no use of slip rings) are very efficient. PMSM motors have become extremely important in the industry in the last few decades. Their success is accounted mainly for high efficiency, high torque density, and reliability [1]–[3]. They are found to be implemented in versatile applications such as renewable energy (RE) power generation, hybrid electric vehicle (HEVs), power tools, household appliances, and heavy propulsion systems [4], [5], to mention a few.

2.1.1. PMaSynRM technology in motor classification

PMSMs of three or more phases are divided into surface mounted (SPMSM) and interior (IPMSM) types. IPMSMs have a smaller effective air-gap and the armature reaction effect is stronger, which makes them easier to operate in the field weakening region up to high speeds 80[40]. The price of rare earth magnets is a disadvantage [41]. The other important drawback is the temperature limitation of neodymium magnets i.e. they undergo demagnetization at around 90º C [42]. Therefore, an SRM motor gained a lot of interest. This is a simple and robust construction without rare-earth magnets so the higher temperature is allowable [43] but lower torque densities and higher ripples are observed. Some examples of PMSM cross-sections in the background of other motor types are depicted in Fig. 2.2.

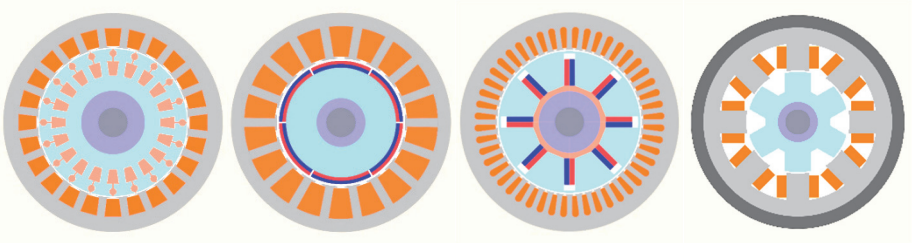

Figure 2.2. Cross section of selected motor types, from left: IM, SPMSM, IPMSM, SRM

SPMSM can generate electromagnetic torque while IPMSM develops the extra reluctance torque component due to magnetic asymmetry in the rotor construction. In this context, PMaSynRM belongs to the PMSM family, however with the main reluctance torque due to rotor anisotropy and an auxiliary torque originating from magnets installed in the rotor magnetic paths. Essentially, PMaSynRM may also be interpreted as a hybrid concept of PMSM and SRM combination. Usually, PMaSynRM is a rare-earth-less motor in which expensive Neodymium or Samarium-Cobalt magnets were replaced by less costly ferrite ones [44], [45]. The reluctance torque is dominant and it is improved by a higher saliency ratio obtained by the introduction of additional flux barriers in the low permeance axis [46], [47]. The magnets are mounted radially [48] or perpendicularly [49] and are magnetized in a positive or negative direction [50] as shown in Fig. 2.3.

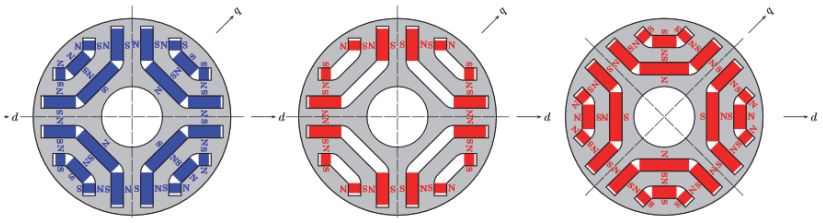

Figure 2.3. Rotor layout of PMaSynRM with several magnet arrangements [50]

Several pieces of researches have demonstrated PMaSynRM can achieve performance good enough to be considered as a real alternative for PMSM machines for electric traction [51], [52]. In summary, it offers the best compromise considering the performance to cost ratio [53].

2.2. Two axis three-phase PMaSynRM model with constant parameters

The conventional two-axis model for three-phase machines based on the Clarke-Park transforms is well known in the literature [1]–[3]. This analytical model was developed with some simplifying assumptions:

- permeability of iron is infinite i.e. saturation is neglected
- distribution of the air-gap flux density is sinusoidal
- constant inductances and permanent magnet flux (constant parameters)
- cogging torque (variation of magnetic co-energy) is negligible
- eddy currents and hysteresis losses are negligible
- there is no field current dynamics

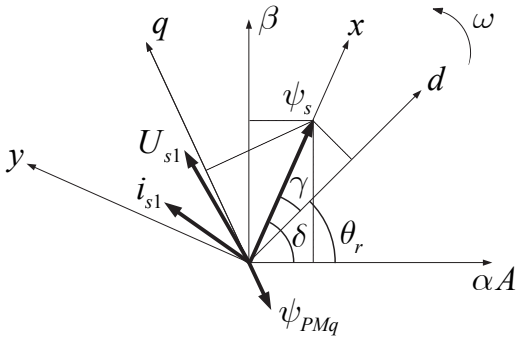

Figure 2.4. Classic two-axis phasor diagram of a three-phase PMaSynRM

In the basis of the considered classic model is the stator voltage equation. The analytical derivation starts from the formulation in the vector/matrix form considering AC quantities in *abc* phases of a three-phase motor. Then with the help of Clarke-Park transform the equations are converted to the *dq* rotor reference frame [1]–[3], in which AC magnitudes become DC "signals". The stator voltage equation of PMaSynRM is given in (2.1):

$$U_d = R_s i_d + \frac{d\psi_d}{dt} - \omega_r \psi_q$$
$$U_q = R_s i_q + \frac{d\psi_q}{dt} + \omega_r \psi_d \tag{2.1}$$

where R_s is the stator resistance, U_d and U_q denote stator *d* and *q* axes voltages, i_d and i_q correspond to *d* and *q* axes currents, ψ_d and ψ_q stand for *d* and *q* axes flux linkages and ω_r is the rotor angular electrical velocity. The flux linkages contain stator current and permanent magnet flux contributions (2.2):

$$\begin{aligned} \psi_d &= L_d \cdot i_d \\ \psi_q &= L_q \cdot i_q - \psi_{PMq} \end{aligned} \tag{2.2}$$

where L_d and L_q are stator *d* and *q* axes inductances and ψ_{PMq} is the permanent magnet flux component. The nomenclature of SRM is used [50] i.e. the low reluctance path is manifested by the *d* axis and the high reluctance by the *q* axis and the magnets act in the negative *q* axis direction as depicted in Fig. 2.4. Note that PM could theoretically also be placed in the d axis simultaneously however for simplicity this constellation is omitted. The electromechanical conversion generates torque obtained as a cross product of the fluxes and currents:

$$T_e = \frac{3}{2} p \left(\psi_d i_q - \psi_q i_d \right) \tag{2.3}$$

where *p* stands for the number of pole pairs. The torque can be as well calculated from (2.4):

$$T_e = \frac{3}{2} p \left(\left(L_d - L_q \right) i_d i_q + \psi_{PM} i_q \right) \tag{2.4}$$

In this form, the magnetic alignment torque is separated from the reluctance torque and the cogging torque (also referred to as detent torque) is not considered.

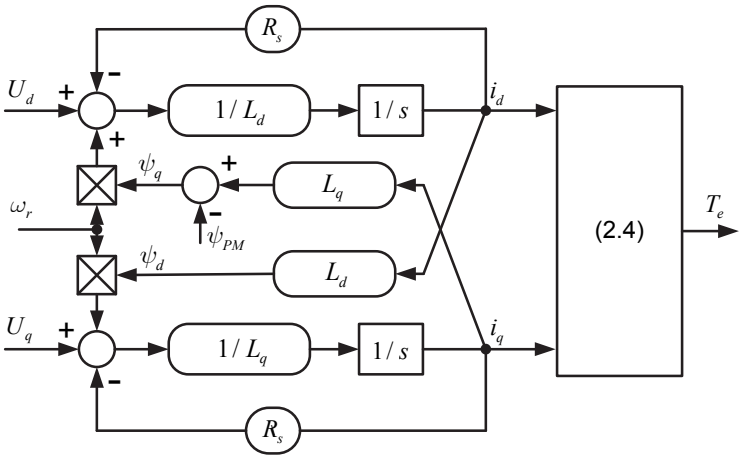

Figure 2.5. Classic three-phase PMaSynRM model in *dq* reference frame

The mechanical system is modeled as first order type considering the viscous friction factor *B* and moment of inertia *J*:

$$T_e = T_L + B\omega_m + J\frac{d\omega_m}{dt} \tag{2.5}$$

where T_L denotes load torque and ω_m rotor mechanical speed. Finally, the voltage model (2.1) is rearranged in such a way that the currents are calculated from the integration of the rate of change of fluxes divided by corresponding inductances as depicted in the complete conventional model in Fig. 2.5.

It needs to be recognized, that the model presented in this chapter is simplified and cannot predict motor behavior precisely. The phase inductances depend sinusoidally on the rotor position, thus all field ripples are neglected. Nevertheless, it is very fast and has become an industry standard for vector control algorithm implementations. Although, it has been recognized that it is inaccurate especially under saturation and particularly disadvantageous for the MTPA control strategy [29]–[31].

2.3. Three-phase PMaSynRM FOC control

The Field Oriented Control of a three-phase PMaSyRM is recapitulated in this section. It is implemented on a motor which parameters are given in Table 2.1. The saliency ratio is approximately equal to 4, which is achieved by a rotor design with several flux barriers that effectively impede flux distribution in the q axis direction. Additionally, permanent magnet flux saturates ribs between flux barriers.

Table 2.1. Three-phase PMaSynRM technical data

Quantity	Symbol	Unit	Value
Number of phases	m	-	3
Rated torque	T_n	Nm	3.4
Base speed	n_n	r/min	5000
Rated power	P_n	kW	2.25
Peak current	$I_{\max}$	A	10
Rated current	I_n	A	4.5
Stator resistance	R_s	Ω	2.2
DC-link voltage	V_{dc}	V	320
D-axis inductance	L_d	mH	28.1
Q-axis inductance	L_q	mH	6.92
Permanent magnet flux	ψ_{PM}	mWb	38

The three-phase PMASynRM vector control is depicted in Fig. 2.6. Currents are measured in two phases (the third phase is calculated from the rest because of motor winding star connection) and then transformed

from the natural *abc* system to first the *αβ* stationary reference frame and then to synchronously rotating *dq* rotor frame. Rotor position θ_r and angular velocity ω_r are obtained by the adequate sensor (resolver, incremental or absolute encoder, etc.). The outer speed loop is regulated by the PI controller which corrects the error of ω_r by a command torque. The reference torque and the actual speed are injected into the MTPA-MTPV which generates reference current in the *d* and *q* axes. The conventional control strategy to obtain optimum current references is derived from the motor equations and minimization of the voltage and current constraints [1], [2], [20].

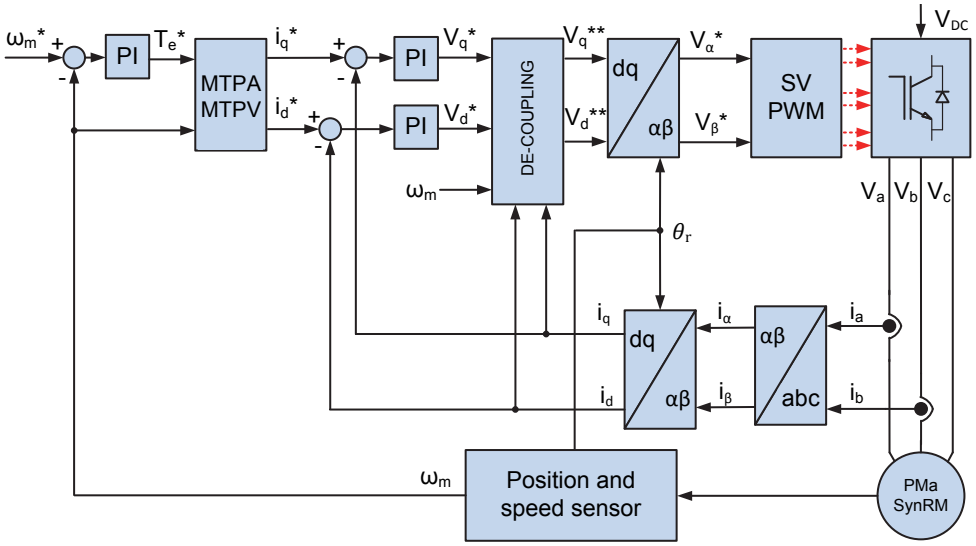

Figure 2.6. Field Oriented Control of a three-phase PMaSynRM

The currents in the *d* and *q* axes are as well controlled by the PI type compensators that generate voltage references in the *d* and *q* axes. The cross-coupling of the EMF terms (2.6) is performed in the decoupling block that compensates for self-induced voltages.

$$U_d^{**} = U_d^{*} - \omega_r \psi_q$$
$$U_q^{**} = U_q^{*} - \omega_r \psi_d \qquad (2.6)$$

where U_d^{*} and U_q^{*} denote voltage command from the PI outputs and U_d^{**}, U_q^{**} stand for the corrected reference voltages considering back-EMF in the motor terminals. The coupling flux linkages in (2.6) are calculated via (2.2). Then, the *d* and *q* axes reference voltages are transformed to stationary *αβ* references which are then synthesized in the modulation block. Standard modulation techniques include PWM, SVM, and the third harmonic injection [1], [2], [20]. Such a closed-loop system is able to correctly track reference signals provided the bandwidth is high enough to reject disturbances. In Fig. 2.7 the current response is shown. Fast and stable operation in *d* and *q* axes is obtained by correct tuning of the PI controllers (e.g. by

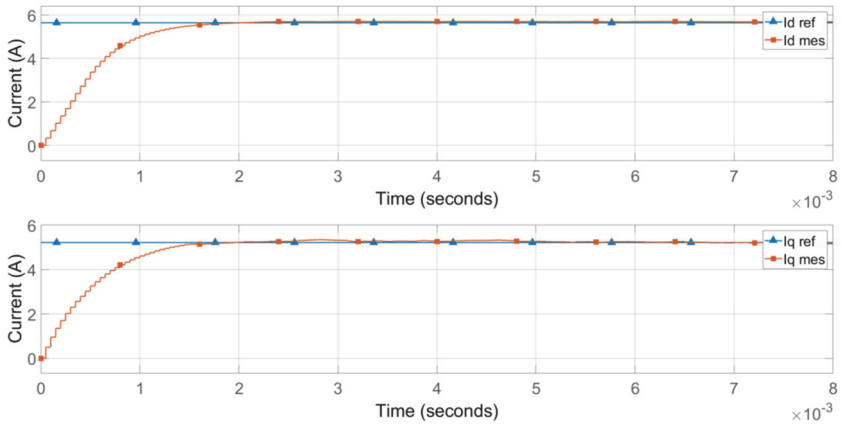

Figure 2.7. Current tracking in FOC of a three-phase PMaSynRM with constant parameters

pole placement or frequency response method). The final goal is achievable as long as motor inductance and PM flux are constant parameters (saturation is not considered).

2.4. Multi-plane five-phase PMaSynRM model with constant parameters

The introduction of a higher number of phases implies higher degrees of freedom in terms of motor modeling [11]. In the five-phase motor configuration, currents may flow not only of the 1st but also of the 3rd harmonic. Therefore, they should be controlled and two cases may arise, namely the presence or absence of the 3rd harmonic in the air-gap field. In the first case, the 3rd harmonic current can interact with the corresponding field harmonic and enhance the electromagnetic torque production, while in the second case the 3rd harmonic current should be controlled to avoid unnecessary losses [8], [14], [15]. When the motor parameters (inductances and PM fluxes) are constant, then the two harmonic fields can be decoupled and treated separately as two stand-alone motors rotating with synchronous and triple synchronous speed as it is illustrated in Fig. 2.8.

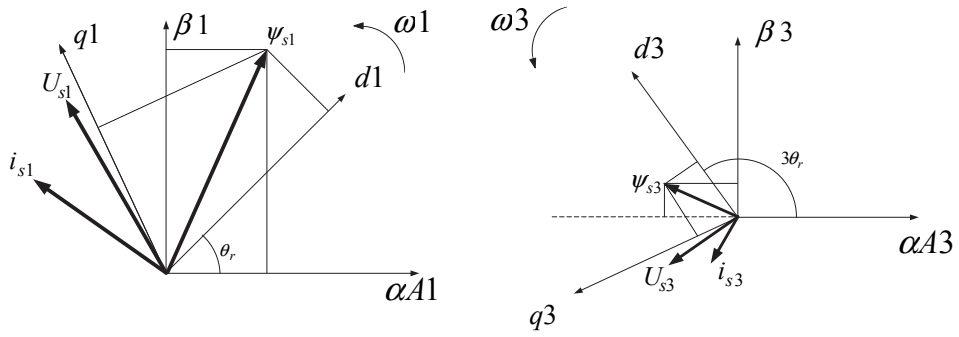

Figure 2.8. Decoupled phasor diagram of a five-phase PMaSynRM

The stator voltage equations (2.1) are valid only for the 1st harmonic, thus another set of equations according to Fig. 2.8 is needed. It is important to mention that the equations for the 3rd harmonic are completely decoupled from the 1st harmonic.

$$
\begin{aligned}
U_{d1} &= R_s i_{d1} + \frac{d\psi_{d1}}{dt} - \omega_r \psi_{q1} \\
U_{q1} &= R_s i_{q1} + \frac{d\psi_{q1}}{dt} + \omega_r \psi_{d1} \\
U_{d3} &= R_s i_{d3} + \frac{d\psi_{d3}}{dt} - 3 \cdot \omega_r \psi_{q3} \\
U_{q3} &= R_s i_{q3} + \frac{d\psi_{q3}}{dt} + 3 \cdot \omega_r \psi_{d3}
\end{aligned}
\tag{2.7}
$$

where ψ_{d1} and ψ_{q1} are the *d* and *q* flux linkages in first harmonic, ψ_{d3} and ψ_{q3} *dq* flux linkages in third harmonic, U_{d1}, U_{q1}, U_{d3} and U_{q3} denote *dq* voltages in first and third harmonics and i_{d1}, i_{q1}, i_{d3}, i_{q3} correspond to respective axis currents. The flux linkages can be calculated from constant inductances:

$$
\begin{aligned}
\psi_{d1} &= L_{d1} \cdot i_{d1} \\
\psi_{q1} &= L_{q1} \cdot i_{q1} - \psi_{PMq1} \\
\psi_{d3} &= L_{d3} \cdot i_{d3} \\
\psi_{q3} &= L_{q3} \cdot i_{q3} - \psi_{PMq3}
\end{aligned}
\tag{2.8}
$$

where L_{d1}, L_{q1}, L_{d3}, L_{q3} are stator *d* and *q* axes inductances of the first and third harmonic and ψ_{PMq1}, ψ_{PMq3} correspond to the permanent magnet fluxes of respective harmonics. The electromagnetic torque is a sum of torques generated separately by the 1st and 3rd harmonic:

$$
\begin{aligned}
T_e &= T_{e1} + T_{e3} \\
T_{e1} &= \frac{5}{2} p \left(\psi_{d1} i_{q1} - \psi_{q1} i_{d1} \right) \\
T_{e3} &= \frac{5}{2} p \left(\psi_{d3} i_{q3} - \psi_{q3} i_{d3} \right)
\end{aligned}
\tag{2.9}
$$

Similarly, as in (2.3), each torque component can be further decomposed to the current generated MMF field interaction and the anisotropic contribution due to reluctance:

$$
\begin{aligned}
T_{e1} &= \frac{5}{2} p \left(\left(L_{d1} - L_{q1} \right) i_{d1} i_{q1} + \psi_{PM1} i_{q1} \right) \\
T_{e3} &= \frac{5}{2} p \left(\left(L_{d3} - L_{q3} \right) i_{d3} i_{q3} + \psi_{PM3} i_{q3} \right)
\end{aligned}
\tag{2.10}
$$

Again torque ripple due to higher field harmonics is omitted and cogging torque is not considered either. The mechanical system is described with equation (2.5).

2.5. Five-phase PMaSynRM FOC control of first and third harmonic

The Field Oriented Control of a five-phase PMaSyRM is outlined in this section. It is implemented on a motor which parameters are given in Table 2.2. The inductances were identified by FEM analysis and are considered to be constant for any current excitation, thus there are no saturation phenomena. However, it is not the case of the prototype machine further studied in this thesis. The geometry and the cross-section of this motor will be given in the following chapter. At the moment it is considered to have constant parameters.

Table 2.2. Five-phase PMaSynRM parameters

Quantity	Symbol	Unit	Value
D1-axis inductance	L_{d1}	mH	26
Q1-axis inductance	L_{q1}	mH	6.92
D3-axis inductance	L_{d3}	mH	
Q3-axis inductance	L_{q3}	mH	
First harmonic PM flux	ψ_{PM1}	mWb	38
Third harmonic PM flux	ψ_{PM3}	mWb	

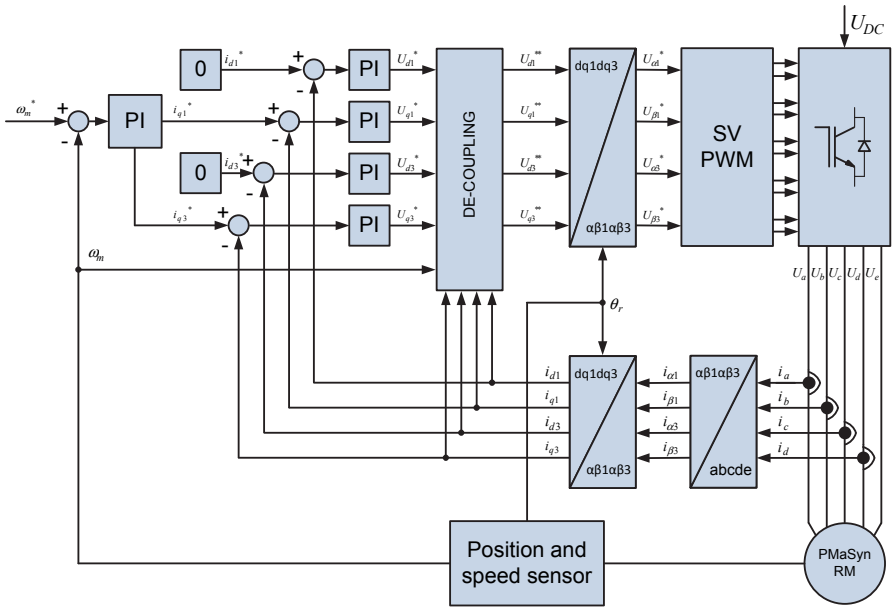

Figure 2.9. Classic Field Oriented Control of a five-phase PMaSynRM

The five-phase PMASynRM control is depicted in Fig. 2.9. It essentially is a vector control of two decoupled motors. Currents are measured in four phases (the fifth phase is derived from summation on the account of five-phase star connected system) and then transformed from the natural *abcde* system to two rotating frames of synchronous (*dq1*) and triple synchronous (*dq3*) angular velocity. Then, similarly to its three-phase counterpart, the outer speed loop is PI regulated. There are four currents in the inner loop that are as well compensated by voltages produced by linear PIs. However, each harmonic contains its cross-coupling term that introduces nonlinearity to the system, therefore the command voltages need to be corrected in the de-coupling block that implements (2.11),

$$\begin{aligned} U_{d1}^{**} &= U_{d1}^{*} - \omega_r \psi_{q1} \\ U_{q1}^{**} &= U_{q1}^{*} - \omega_r \psi_{d1} \\ U_{d3}^{**} &= U_{d3}^{*} - 3\omega_r \psi_{q3} \\ U_{q3}^{**} &= U_{q3}^{*} - 3\omega_r \psi_{d3} \end{aligned} \tag{2.11}$$

where magnitudes denoted with * stand for PI reference voltages and with ** correspond to the EMF corrected references that are transformed back to the stationary reference frame and injected into the modulation block. The flux linkages in (2.11) are calculated from (2.8) with constant inductances and PM fluxes as given in Table 2.2. A train of pulses is obtained through one of the selected modulation techniques. They are broadly described in the literature e.g. a linear five-phase PWM [54], SVM based on multiple *dq* spaces concept [32], or other multi-phase approaches [55], [56].

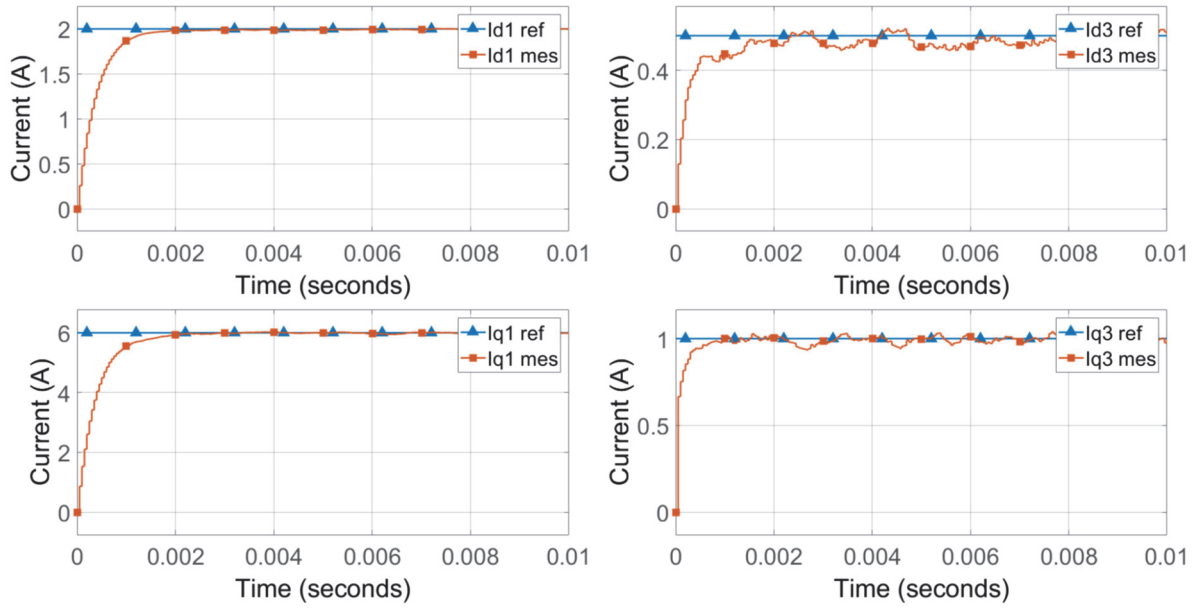

Figure 2.10. Current tracking in FOC of a five-phase PMaSynRM with constant parameters

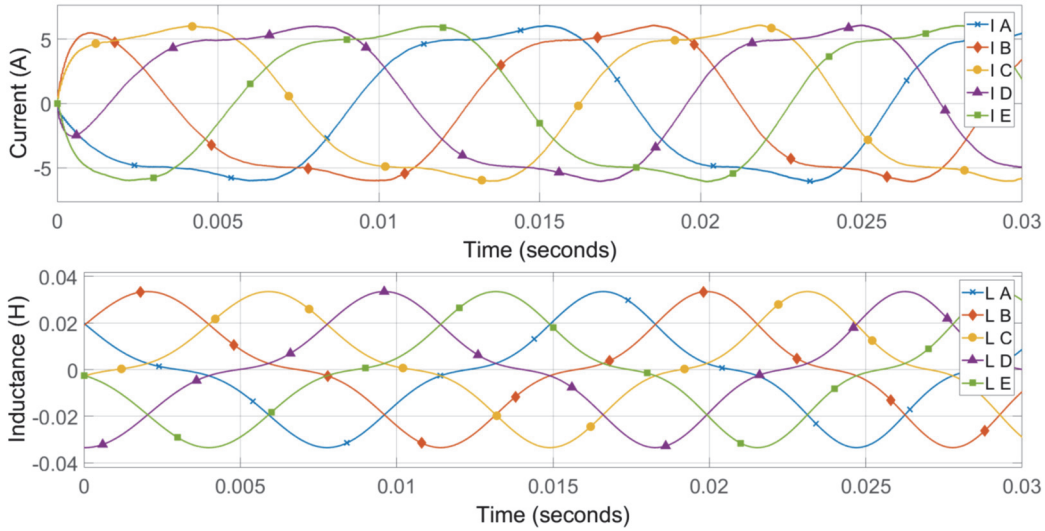

Figure 2.11. Phase current (top) and apparent phase inductance (bottom) in FOC of a five-phase PMaSynRM with constant parameters

The PI regulators, when properly tuned taking into account parameters from Table 2.2, are able to track reference currents in very fast settling time. The responses of the 1st (*dq1*) and 3rd (*dq3*) harmonic currents are depicted in Fig. 2.10, while Fig. 2.11 shows the phase currents and corresponding apparent phase inductances. The waveforms contain two discussed harmonics that are integral for this model with constant inductances. The saturation phenomena are not included and there are no higher order harmonics that originate from the field distortions.

2.6. Conclusions

In this chapter, a review of the state of the art PMaSynRM drive based on FOC control was given first for the classic three-phase motor and then for the five-phase one. The conventional modeling and development of the control system were recapitulated. In summary, these methods provide a very good response and can be applied to motors designed to work in linear magnetization zone before saturation. Moreover, the simplification does not account for the field's higher harmonics and distortion of voltage and current waveforms that impact the overall drive performance. The models with constant parameters are intrinsically limited and become erroneous especially when considering PMaSynRM in which cross saturation is a built-in feature of the motor.

3

3. Multiphase PMaSynRM flux map model with cross saturations and space harmonics

The previous chapter reviewed classic drive development with a conventional motor model. In this chapter, an improved model comprising cross saturations, space harmonics, and cogging torque is proposed. It is established on inverted flux maps with detailing of the selected nonlinear phenomena originated from three-phase and five-phase PMaSynRM. The concept is realized for healthy motors, three-phase PMaSynRM in the *dq* reference frame, and in the *dq1dq3* frame for a five-phase PMaSynRM as well as in natural stator phase variables for conditions with single open and double open phases. The models are contrasted with FEA analysis and a new improved FOC control is discussed.

CONTENTS:

3.1. Cross saturating 2D three-phase PMaSynRM model in *dq* rotor reference frame

In chapter 2 the standard model of three and five-phase PMaSynRM motor was presented. They consider neither space harmonics nor saturation and will be referred to as 0D models further on. The inductances are constant values and flux trajectories without power converter are circular in the steady-state regime. These are the fastest models to identify being inherently the least precise.

At first, the saturation will be considered in the motor model. The soft magnetic materials increase their magnetization in a non-linear fashion. The first segment of the *B(H)* characteristics is approximately linear while further increase in the magnetic field intensity does not substantially increase magnetization *B*. The saturation mechanism exists in all types of machines and is observed as no increment in the flux linkage of the associated phase at adequately high current excitations (see Fig. 3.1). It is analogously revealed in the decrease of the corresponding phase inductance, Fig. 3.2. Usually, to avoid excessive losses, the motors are designed to operate out of the saturation region. However, for a PMaSynRM it is already considered in the design stage for sake of the saliency ratio (between *d* and *q* inductances) as it is the major torque producing component. A drop in inductance may decrease the saliency ratio and imply lower torque performance.

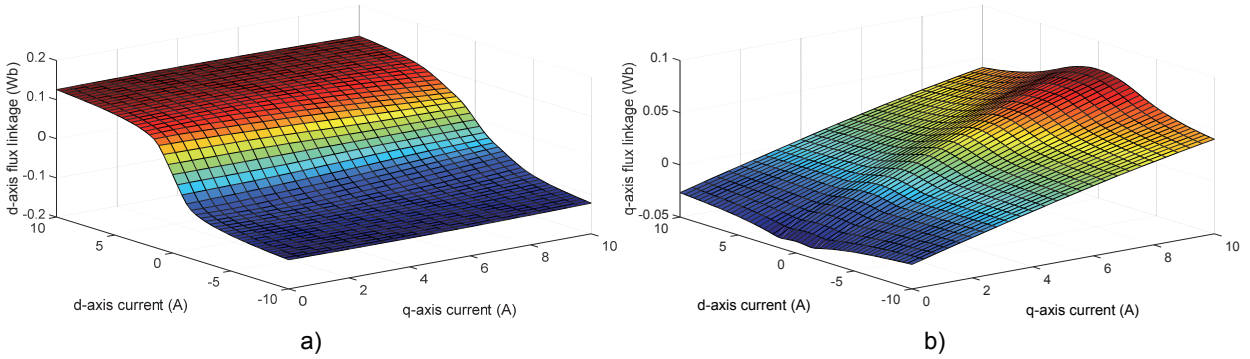

Figure 3.1. Three-phase PMaSynRM flux linkage map a) ψ_d , b) ψ_q

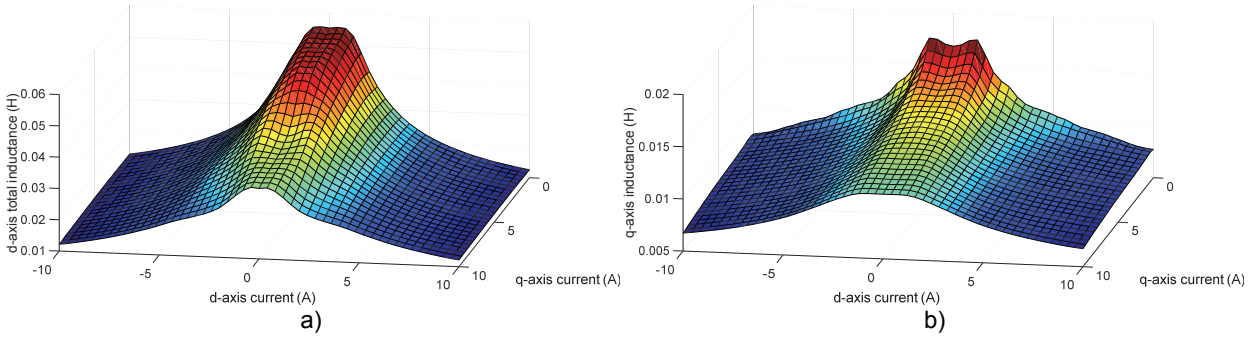

Figure 3.2. Three-phase PMaSynRM inductance map a) L_d , b) L_q

In the two-axis *dq* modeling, the inductances L_d and L_q can be analytically determined with help of the Winding Function Theory (WFT) [57], [58]. The other approach is to compute them with FEA analysis by flux linkage calculation at unitary current for *d* or *q* axis-aligned rotor [59]. Experimental evaluation is also possible in the locked rotor conditions by a measure of the first-order response time constant [60], [61]. These methods explain how to determine constant inductances. However, flux linkages and inductances of PMaSynRM vary according to stator current excitation in such a way that the d-axis flux linkage ψ_d is saturated not only by the *d*-axis current i_d but also by the *q*-axis current i_q. This is the so-called cross-coupling saturation [26]–[28] (and is analogically present in the *q*-axis). It can be perceived in Fig. 3.1 and 3.2. Because the flux linkages (and inductances) depend on two axis currents the model described in this section will be referred to as 2D saturation.

3.1.1. Inverted flux map model

The motor voltage equations in (2.1) are still valid and form the basis of the 2D model as well. However, instead of using inductances and PM flux, it is possible to operate on the flux linkages only.

$$\begin{aligned} \psi_d &= f_d\left(i_d, i_q\right) \\ \psi_q &= f_q\left(i_d, i_q\right) \end{aligned} \tag{3.1}$$

where *d* and *q* axis flux linkages ψ_d, ψ_q are functions of both *d* and *q* axis currents. Therefore, the nonlinear effect of saturation is included in the flux linkage functions. These functions (3.1) are acquired via FEM analysis through multi-static simulation sweep with current excitations combinations covering all operating conditions and they are either fitted to compound mathematical functions (exponential-polynomial) either stored as look-up tables (LUTs). In Fig. 3.1 the co-ordinate grid of currents was established to be <-10,10> for i_d and <0,10> for i_q with a step of 1A. In total there are 231 static FEM simulations performed. The negative d-axis current values may be omitted provided motor works close to the MTPA region. In the discussed model, the flux linkages are calculated by integration resulting from the voltage model (2.1), that gives:

$$\begin{aligned} \psi_d &= \int\left(U_d - R_s i_d + \omega_r \psi_q\right) \\ \psi_q &= \int\left(U_q - R_s i_q - \omega_r \psi_d\right) + \psi_{PM}\left(\theta_0\right) \end{aligned} \tag{3.2}$$

where θ_0 stands for the initial rotor position and ψ_{PM} is the PM flux. It is assumed that at the initial condition there is no current flowing in the bobbins and therefore the only flux is thrown by the permanent magnets and actually it is already saved in the q-axis flux linkage map with coordinates (0,0). Once the flux

linkages are calculated the current should be determined. To accomplish this, the flux linkage functions (3.1) needs to be inverted:

$$i_d = f_d^{-1}\left(\psi_d, \psi_q\right)$$
$$i_q = f_q^{-1}\left(\psi_d, \psi_q\right) \tag{3.3}$$

It is a 2D inversed problem that can be solved with mathematical techniques such as the inverse grid intersection [31]. The other option is to iteratively search for the minimum error between a seed and an

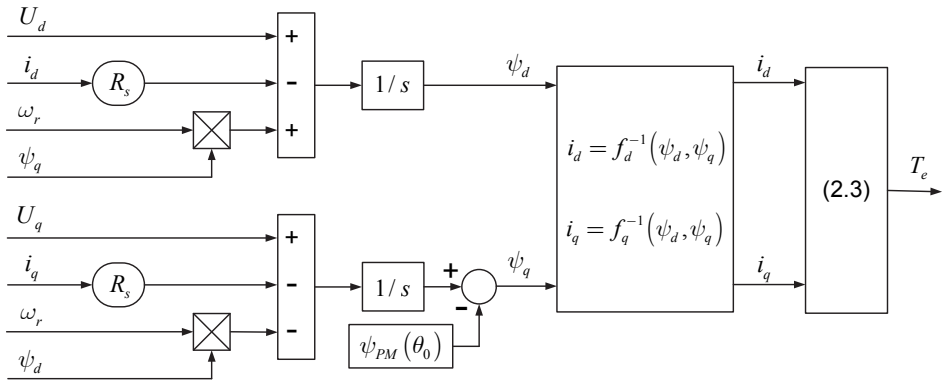

Figure 3.3. Three phase PMaSynRM 2D saturated model based on inverted flux maps

interpolated map value. The 2D map inversion of the pre-calculated flux linkage dataset is an additional operation. The model schematic is depicted in Fig. 3.3 and the inverted flux maps are illustrated in Fig. 3.4. It is seen that the edges fall out from the flux domain, however, they are present in the coordinate vectors. Therefore, in these areas, the maps are extrapolated from available data. This operation is performed to complete the dataset and has no impact on the model performance provided the current-flux domain is not crossed. The electromagnetic torque is computed with (2.3).

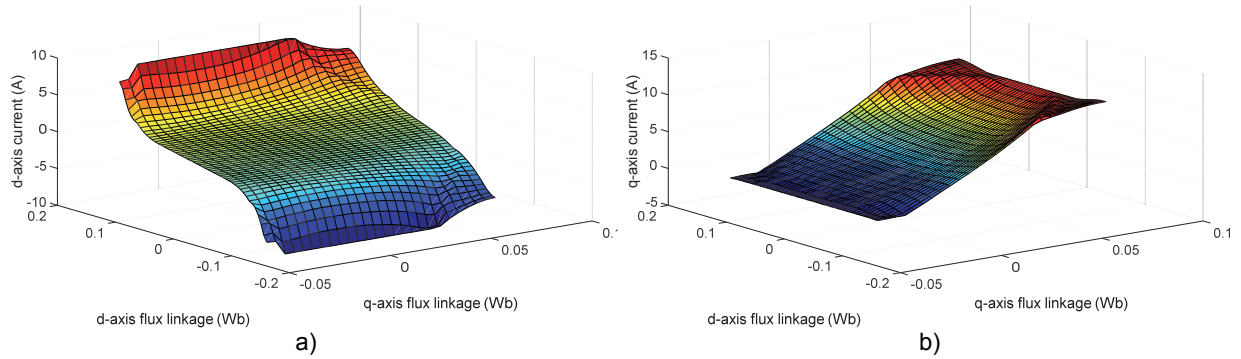

Figure 3.4. Three-phase PMaSynRM current (inverted flux) map a) i_d , b) i_q

3.1.1. Apparent inductance model

Instead of using (and to avoid computing) inverted flux maps (3.3) to calculate currents, it is possible to operate on *d* and *q* axis inductance maps (see Fig. 3.2) and permanent magnet flux map. To obtain them, the flux maps (3.1) resulting from FEM are necessary. First, to acquire the *d* axis inductance map each element of the *d* axis flux map is divided only by the *d* axis current from all currents provoking it. Permanent magnet flux ψ_{PM} map is cut out from the *q* axis flux linkage map with zero *q* axis current excitation and

$$\begin{aligned} U_d &= R_s i_d + \frac{d\left(L_d i_d\right)}{dt} - \omega_r \left(L_q i_q - \psi_{PM}\right) \\ U_q &= R_s i_q + \frac{d\left(L_q i_q - \psi_{PM}\right)}{dt} + \omega_r L_d i_d \end{aligned} \tag{3.4}$$

then it is subtracted from every element of *q* axis flux linkage map, and the result is divided by the *q* axis current to obtain *q* axis inductance map. In the nonlinear context of the flux linkages, the equation (2.2) can only be satisfied virtually i.e. it is impossible to separate PM flux from the phase fluxes induced in self inductances. In other words, the PM flux also changes when the winding is current excited. Although it is possible to work with the pre-calculated inductance maps. To avoid infinite inductances, the resolution in the vicinity of zero current excitation may be higher and the infinite inductance is replaced by its neighbor element. Numerical singularity problems may appear. Because inductances are dependent on both currents (and therefore time), they should not be taken outside derivation as shown in (3.4). Furthermore, the change of flux from permanent magnets also contributes to the derivation of the self-induced voltage term and it can be assumed to be dependent on counter axis i_d current as in Fig. 3.5, although, in reality, it may depend on both axes currents (however in most designs the q-axis is low permeant and self-axis current does not disrupt the field provoked by magnets). In summary, the variable parameters are obtained as below:

$$\begin{aligned} L_d &= \frac{\psi_d}{i_d} = f_{Ld}\left(i_d, i_q\right) \\ L_q &= \frac{\psi_q - \psi_{PM}}{i_q} = f_{Lq}\left(i_d, i_q\right) \\ \psi_{PM} &= \psi_q\left(i_d, 0\right) = f_{PM}\left(i_d\right) \end{aligned} \tag{3.5}$$

In any case, it is possible to further simplify the model so it works with the DC value of PM flux and projects its saturated fluctuation voltage into the self-induced ones. To do this, select a constant value for the magnet flux and subtract it from every element of the flux linkage map and then perform division as in (3.5). The constant value of ψ_{PM} should be selected with special care so that resulting L_d and L_q do not cross the zero plane, so there are no negative inductance elements. It should be noted that these new

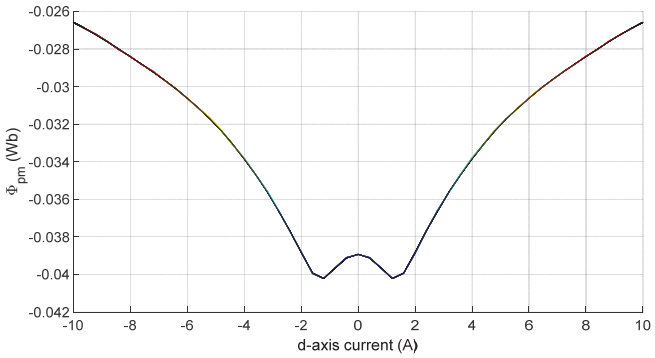

Figure 3.5. Permanent Magnet Flux due to saturation

inductances and magnet flux are abstract values i.e. they do not mean physical machine quantities any longer. A sum of their effects represents the real flux linkage. This simplification (3.6) is made to virtually satisfy the superposition theorem for the flux linkages. It makes the voltage model consistent and in terms of the electrical magnitudes equivalent and realistic. This model is depicted in Fig. 3.6 and similarly to the previous one, it needs to be provided with the initial condition. The negative sign of $\psi_{PM}(\theta_0)$ comes from the colocation of magnets on the negative q axes. The flux linkages are computed as in (3.2) and then divided by corresponding inductances to obtain dq currents. Electromagnetic torque can be calculated with (2.3) or equally as in (2.4).

$$L_q = \frac{\psi_q - \psi_{PMnew}}{i_q} = f_{Lqnew}(i_d, i_q)$$
$$\psi_{PMnew} = const. \tag{3.6}$$

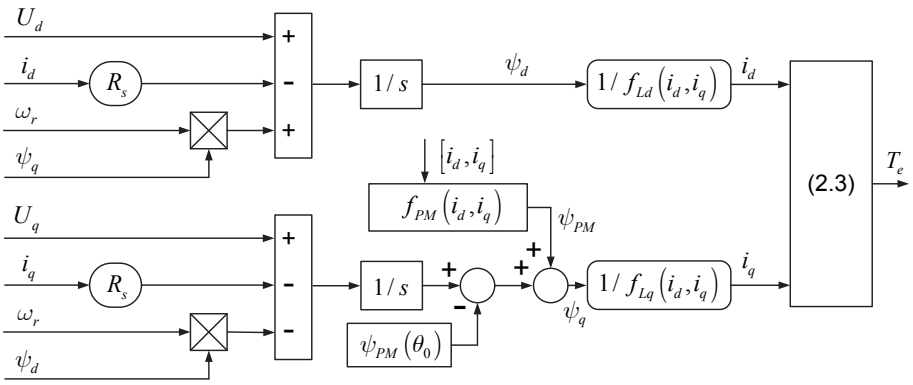

Figure 3.6. Three phase PMaSynRM 2D saturated model based on apparent inductances

In total two 2D inductance maps and one 1D permanent magnet flux map are required to run this model in the first embodiment while in the second it is reduced to the inductance maps only since PM flux is a constant value.

3.2. Space harmonics 3D three-phase PMaSynRM model in *dq* rotor reference frame

The flux maps in (3.1) depend on both d and q axes currents thus they reflect saturation as shown in Fig. 3.1. In reality, fluxes change according to the rotor position due to local permeance variation originated from the alternation of slots and teeth in the stator construction together with non-sinusoidal field distribution created by rotor magnets. These features distort the flux linkages and generate space harmonics. One can extend the flux maps (3.1) with additional sweep along rotor mechanical angle:

$$\begin{aligned} \psi_d &= f_d\left(i_d, i_q, \theta_r\right) \\ \psi_q &= f_q\left(i_d, i_q, \theta_r\right) \end{aligned} \tag{3.7}$$

This operation is a fundamental contribution to reflect not only the space harmonics but the saturation phenomena in combination with the space harmonics. In fact, the resultant distorted air-gap field is further

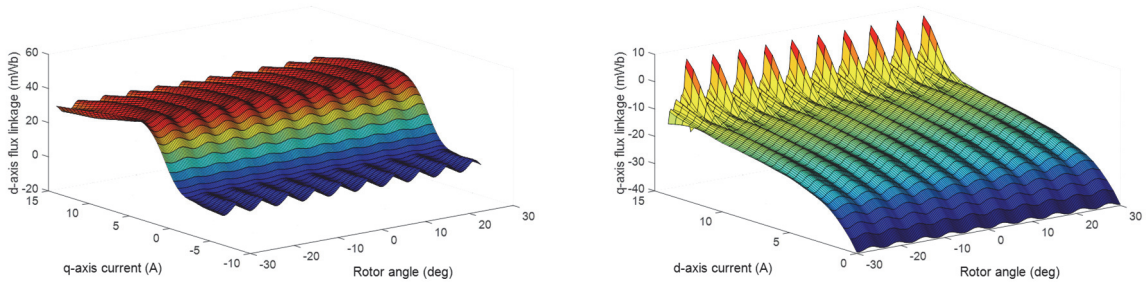

Figure 3.7. Three-phase PMaSynRM flux linkage 3D map a) ψ_d at $i_d = 0$, b) ψ_q at $i_q = 0$

affected by the local saturations that change reluctance in the iron paths (for example tooth tips). Accordingly, a 3D flux map inversion needs to be performed to obtain current maps:

$$\begin{aligned} i_d &= f_d^{-1}\left(\psi_d, \psi_q, \theta_r\right) \\ i_q &= f_q^{-1}\left(\psi_d, \psi_q, \theta_r\right) \end{aligned} \tag{3.8}$$

Then, the motor model is implemented as in Fig. 3.3 with respective current maps defined in (3.3). During FEM scan to obtain flux maps, it is also possible to extract torque for each current and rotor position and store it as a fitted function or a LUT:

$$T_e = f_T\left(\psi_d, \psi_q, \theta_r\right) \tag{3.9}$$

This approach is more precise than using equation (2.3) because torque ripple is a consequence of not only distorted field and currents but also the variation of the magnetic co-energy. The latter component is also referred to as cogging or detent torque and is included in (3.4). A piece of a torque map is illustrated in Fig. 3.8, where the oscillation due to all aforementioned effects can be perceived.

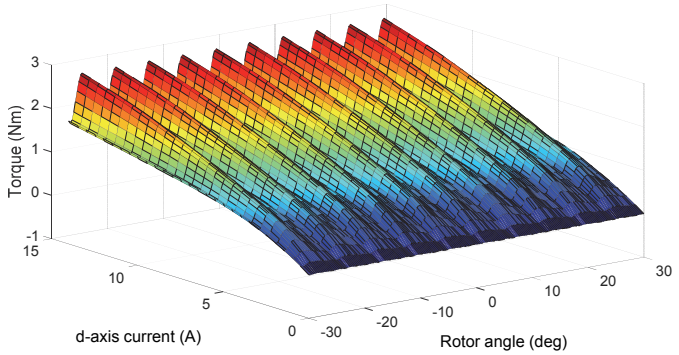

Figure 3.8. Three-phase PMaSynRM torque 3D map

3.3. Cross-wise saturating 4D five-phase PMaSynRM model in *dq1dq3* reference frames

The model of five-phase PMaSynRM with constant parameters was given in chapter 2.4. There are two planes fixed to the first and third harmonics of the rotating field. Conceptually, the 2D saturating flux map model for a three-phase motor can be applied for two rotating harmonics of a five-phase motor separately, to obtain a 4D model This will be demonstrated in this section. The model is elaborated on the five-phase 60-slot, 6-pole PMaSynRM prototype machine with parameters defined in Table 3.3, and the cross-section

Figure 3.9. Five-phase PMaSynRM prototype a) cross section, b) assembled stator, c) rotor layout

and stator and rotor assemblies are shown in Fig. 3.9. It can be applied with any rotor layout of PMaSynRM motors. The motor model (voltage equations) is described by equation (2.7). The *dq* fluxes of the 1st and 3rd harmonic depend on all harmonic currents. It means that additionally to cross-coupling between *d* and *q* axes there is also cross harmonic coupling i.e. the third harmonic currents may saturate the first harmonic

fluxes and vice versa. An example of how currents from the *dq3* plane alter magnetic flux lines distribution is illustrated in Fig. 3.10, where different density in teeth due to third harmonic currents is evident.

Table 3.1. Five-phase PMaSynRM prototype machine specification

Quantity	Symbol	Unit	Value
Number of phases	m	-	5
Rated torque	T_N	r/min	6.8
Base speed	n_N	kW	5000
Rated power	P_N	A	3.5
Peak current	$I_{\max}$	A	10
Rated current	I_N	A	4.5
Stator resistance	R_s	Ω	2.2
Number of pole pairs	p	-	6
Number of slots	N	-	60
Active stack length	l_{stack}	mm	26
Stator outer diameter	D_{so}	mm	148
Rotor outer diameter	D_{ro}	mm	114
Airgap length	d_{gap}	mm	6

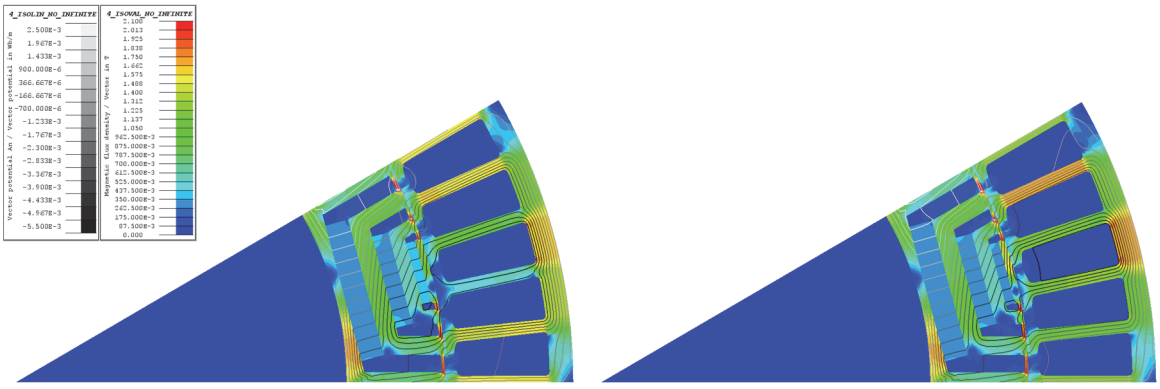

a) b)

Figure 3.10. Magnetic flux densities of five-phase PMaSynRM with constant first harmonic current and a) no third harmonic, b) constant third harmonic excitation

Thus, the flux linkage maps and their inverse function for all axes may be written as:

$$\begin{aligned}\psi_{dn} &= f_{dn}\left(i_{d1}, i_{q1}, i_{d3}, i_{q3}\right) \\ \psi_{qn} &= f_{qn}\left(i_{d1}, i_{q1}, i_{d3}, i_{q3}\right)\end{aligned} \Rightarrow \begin{aligned}i_{dn} &= f_{dn}^{-1}\left(\psi_{d1}, \psi_{q1}, \psi_{d3}, \psi_{q3},\right) \\ i_{qn} &= f_{qn}^{-1}\left(\psi_{d1}, \psi_{q1}, \psi_{d3}, \psi_{q3},\right)\end{aligned} \tag{3.10}$$

The flux functions (3.10) are established by FEM, conducting multi-static currents sweep comprising all working conditions. In the case of the prototype machine the ranges in this study for i_{d1}, i_{q1} are of $\langle -10,10 \rangle$ A, for i_{d3}, i_{q3} are of $\langle -3,3 \rangle$ A. Thanks to the small amplitude of *dq3* magnitudes, the span for this plane is substantially lower, which is beneficial in terms of a reduced dataset. It contains 21609 steps but on the cost of loss of space harmonics information. Therefore, the air-gap flux is sinusoidal and just the saturation phenomena are included and will be reflected with non-linear inductances

3.4. Space harmonics 5D five-phase PMaSynRM model in *dq1dq3* reference frame

The main drawback of the model presented in section 3.3 is the lack of space harmonics. As already discussed for the three-phase motor, the field distortions can be stored in the flux maps provided they are identified for the complete rotor revolution. This is the case when the 4D model with cross-harmonic saturations is extended to 5D including space harmonics. For the sake of clarity, the voltage equation for a five-phase system is the same and repeated below in a compact form:

$$\begin{aligned} U_{dn} &= R_s i_{dn} + \frac{d\psi_{dn}}{dt} - n\omega_r \psi_{qn} \\ U_{qn} &= R_s i_{qn} + \frac{d\psi_{qn}}{dt} + n\omega_r \psi_{dn} \end{aligned} \tag{3.11}$$

$$\begin{aligned} \psi_{dn} &= f_{dn}\left(i_{d1}, i_{q1}, i_{d3}, i_{q3}, \theta_r\right) \\ \psi_{qn} &= f_{qn}\left(i_{d1}, i_{q1}, i_{d3}, i_{q3}, \theta_r\right) \end{aligned} \tag{3.12}$$

where *n* denotes first (*n=1*) or third (*n=3*) harmonic space, *dn*, *qn* axes flux linkages ψ_{dn}, ψ_{qn} are functions of all *d1*, *q1*, *d3*, *q3* currents and the rotor position as well (3.12). Additional rotor angle θ_r sweep for the

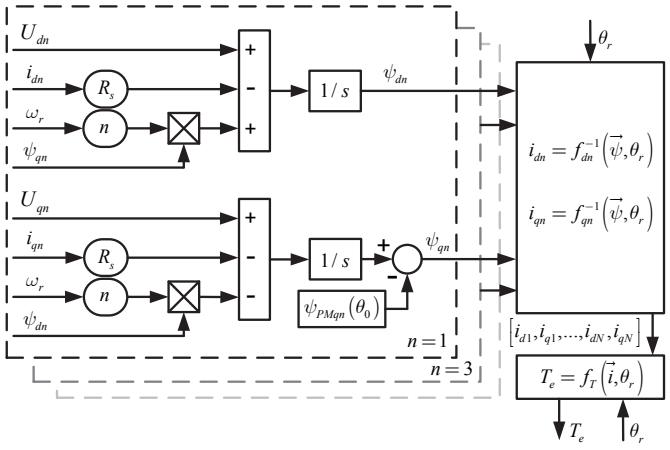

Figure 3.11. Five-phase PMaSynRM 5D model in *dq1dq3* reference frames

prototype machine is performed in the range of $\langle -180°, 180° \rangle$. Altogether there are 672525 steps to be simulated in the static FEM to fully identify this model. The torque in each plane can be computed as a cross vector product of corresponding fluxes and currents and then torque components from the *1st* and *3rd* harmonics are added. However, such approach does not account for the cogging ripple, therefore, to include this effect, it can be directly extracted from FEM and stored in the same way as flux linkages as a function (or LUT) of all currents and rotor position θ_r:

$$T_e = f_T\left(i_{d1}, i_{q1}, i_{d3}, i_{q3}, \theta_r\right) \tag{3.13}$$

The flux linkages from *dq1dq3* planes are calculated by integrals resulting from the voltage model (3.11) as follows:

$$\begin{aligned} \psi_{dn} &= \int \left(U_{dn} - R_s i_{dn} + n\omega_r \psi_{qn}\right) \\ \psi_{qn} &= \int \left(U_{qn} - R_s i_{qn} - n\omega_r \psi_{dn}\right) + \psi_{PMqn}\left(\theta_0\right) \end{aligned} \tag{3.14}$$

where *n* subscript denotes first or third harmonic. Concerning startup modeling, these integrals are supplied with the initial condition that is the flux linkage state at zero time. For no currents, it depends just on the position of the rotor θ_r and results from permanent magnets $\psi_{PMqn}\left(\theta_0\right)$. In the case of the studied machine, the PM flux acts only in the *q* axes. This data is already collected in (3.12). Still, the inverse functions of those in (3.12) are required to determine *dq1dq3* currents from *dq1dq3* flux linkages:

$$\begin{aligned} i_{dn} &= f_{dn}^{-1}\left(\psi_{d1}, \psi_{q1}, \psi_{d3}, \psi_{q3}, \theta_r\right) \\ i_{qn} &= f_{qn}^{-1}\left(\psi_{d1}, \psi_{q1}, \psi_{d3}, \psi_{q3}, \theta_r\right) \end{aligned} \tag{3.15}$$

In general, it is a complex (N-1)D (because rotor angles can be handled independently) inverse problem to solve. There are methods reported in the literature such as error minimization or inverse grid intersection

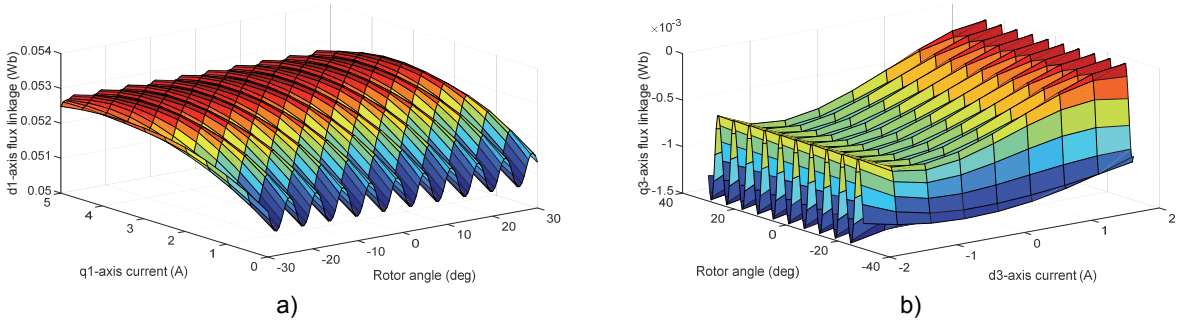

a) b)

Figure 3.12. Five-phase PMaSynRM flux linkage 5D map a) ψ_{d1} at $i_{d1} = 5$, $i_{d3} = i_{q3} = 0$, b) ψ_{q3} at $i_{d1} = 0.5$ $i_{q1} = 4.5$

that can be employed. The calculation of current maps takes about 11 hours on parallel local 8 worker cluster.

The model schematic is shown in Fig. 3.10. It is based on (3.11). The flux linkages are calculated with (3.14), the currents and the torque are obtained from functions/maps of (3.15) and (3.13) respectively. The flux map (3.12) examples concerning one axis current and mechanical angle are shown in Fig. 3.12. The initial condition from permanent magnets with no current excitation is explicitly shown in Fig. 2 and is determined from the function/map of (2). In sum, one 1D and five 5D maps are required to run the five-phase model.

3.5. Open phase saturating and space harmonic 6D five-phase PMaSynRM model in *abcde* frame

The previous 4D and 5D models were developed in the *dq1dq3* reference frames. The latter one is the most precise so far, as it contains saturation, field harmonics, and cogging torque. The Clarke-Park reference frame transformations assume symmetrical star connection. In the case of a single or double open phase fault, the system is not symmetric any longer, thus the models described in previous sections are not valid for such conditions. A new 6D model is proposed hereafter, it is implemented in the natural *abcde* reference frame. It also contains the slotting and winding distribution nonlinear effects together with local saturations as the fluxes in each phase depend on currents from all phases (mutual saturation effect). Moreover, the 6D model can reflect these phenomena in adjacent and non-adjacent open phase states. The voltage equation valid for each of the phases is given as:

$$U_x = R_s i_x + \frac{d\psi_x}{dt} \tag{3.16}$$

where x denotes one of the five phases (a, b, c, d or e). The flux linkages ψ_a, ψ_b, ψ_c, ψ_d, ψ_e are functions

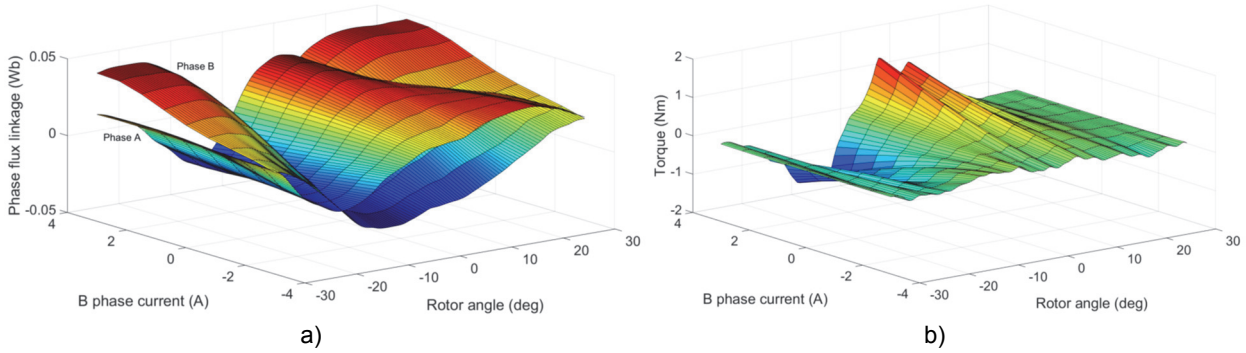

Figure 3.13. Five-phase PMaSynRM 6D map fragments a) flux linkage ψ_a and ψ_b, b) electromagnetic torque

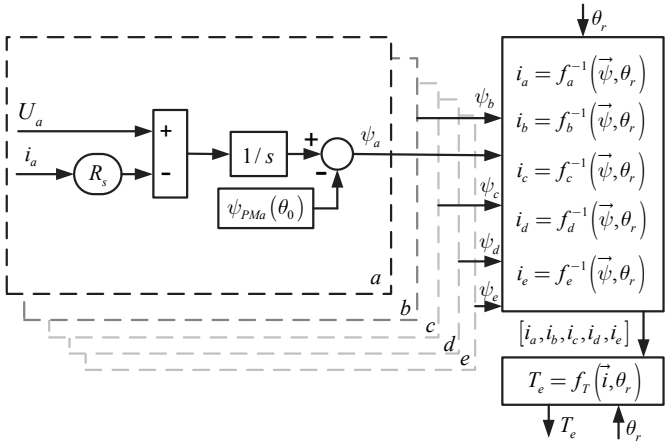

Figure 3.14. Five-phase PMaSynRM 6D model in natural phase abcde reference frame

of all *a*, *b*, *c*, *d* and *e* currents, and the rotor position θ_r as well:

$$\psi_x = f_x(i_a, i_b, i_c, i_d, i_e, \theta_r) \tag{3.17}$$

Respectively, the geometry induced and saturation induced harmonics are included in the flux linkage functions. The flux functions (3.17) are also identified by FEM analysis performing multi-static simulations. In the case of the analyzed prototype machine, the ranges for currents are of $\langle -6,6 \rangle$ A, and the rotor position is $\langle -180°, 180° \rangle$ .This is an extremely large LUT of more than 3M elements of flux linkages in total. In each FEM static calculation step, the torque is also computed in the same way:

$$T_e = f_T(i_a, i_b, i_c, i_d, i_e, \theta_r) \tag{3.18}$$

Segments of the 6D phase flux linkage map and torque map are depicted in Fig. 3.13. Then, the model calculates flux linkages from the input voltages and resistive voltage drops:

$$\psi_x = \int (U_x - R_s i_x) + \psi_{PMx}(\theta_0) \tag{3.19}$$

where *x* subscript denotes one of the five phases. In every phase, the flux linkage is fed with the initial condition that is for example during the start-up phase the currents in all phases are null, therefore the flux present is only due to permanent magnet interactions. It can be read from the maps (3.17) with all currents set to 0. Further, the resulting currents are obtained from inversed *abcde* flux maps:

$$i_x = f_x^{-1}(\psi_a, \psi_b, \psi_c, \psi_d, \psi_e, \theta_r) \tag{3.20}$$

The 6D inversion requires a very long computation time, which can be accelerated by parallel computing methods. The model schematic is shown in Fig. 3.14, where phase *A* is explicitly depicted. The flux linkages

are calculated with (3.19) and the initial conditions are injected for integration in each phase. In total, five 1D (flux initial conditions) and six 6D (inverted flux) maps are needed to construct this model.

3.6. Comparative study of five-phase PMaSynRM models

The flux map database was acquired in Altair Flux 12.3 FEA package on 8 parallel workers with 2D static simulations. Then, the dynamic analytical models 0D, 4D, 5D, and 6D were built in Matlab 2019a environment. To complete the scope of comparison of the 6D model versus the others, a validation with transient FEM 2D was performed. Because the dataset rises exponentially when the fine resolution of the coordinate currents and rotor position is selected, therefore a reasonably high step is recommended. After

Table 3.2. Computation dataset comparison of PMaSynRM models

		0D	4D	5D	6D
No. of steps		2	11025	672525	3601989
Current step	A	-	1	1	1.5
Angle step	elec°	-	-	1	1
Static FEM solution*	days	-	0.02	1	6
FEM post-processing	h	-	0.013	0.78	25
FEM data extraction	h	-	0.05	3	96

* cluster of 8 parallel workers

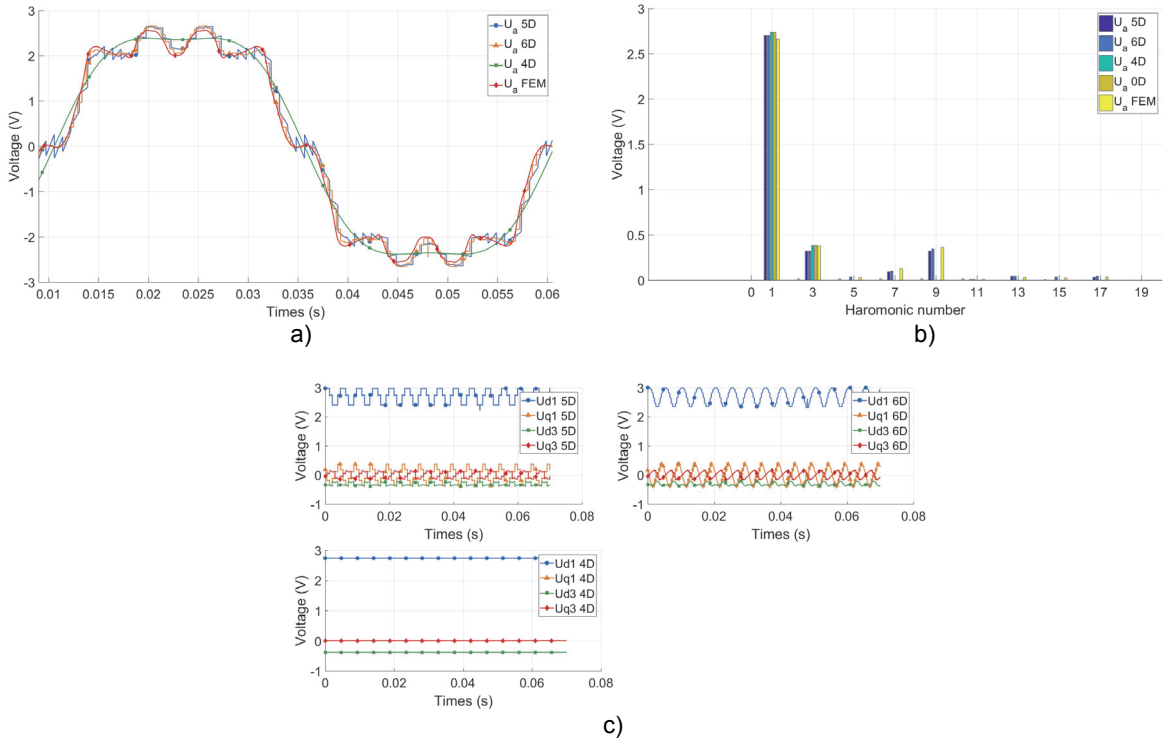

Figure 3.15. Open circuit voltage of five-phase PMaSynRM n-D vs FEM models, a) phase A, b) FFT of phase A c) dq1dq3

FEM identification, the maps are post-processed with off-line interpolations to virtually increase the resolution of extracted maps. In Table 3.2 a comparison of the computational load is shown for each model with distinction to FEM problem solving, results post-processing, and data extraction. The higher number of dimensions the larger the dataset is and more memory resources are needed.

3.6.1. Generator mode

First, the open phase condition was assessed in the models in Matlab 2019a. The rotor was accelerated to 200 rpm and the speed was maintained constant. The back-EMF measured in terminals of phase A and its FFT are depicted in Fig. 3.15 a) and b) respectively and in (c) the transformed *dq1dq3* voltages are shown. The 0D and 4D models overestimate 1st and 3rd harmonics and do not contain the 7th and the 9th ones, neither the higher-order harmonics are present. The results of 5D and 6D models match very well

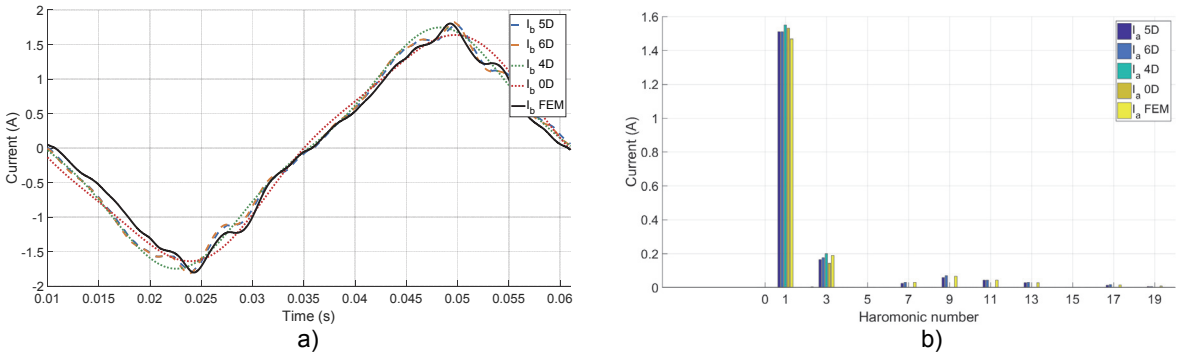

Figure 3.16. Short circuit current of five-phase PMaSynRM n-D vs FEM models, a) phase A, b) FFT of phase A

with FEM predictions. The 6D model is even closer to FEM simulations as it exhibits 5th and 15th harmonics which is not reflected in the 5D model. Thus, the 6D model is considered to be the most precise. Then, the motor terminals were shorted and again the motor was accelerated from standstill to a settled speed of 200 rpm. The dynamic short circuit scenario takes into account the initial condition, transient and steady-state responses. The current distorted shape is depicted in Fig. 3.16 a). Very good agreement is demonstrated between FEM and 5D and 6D models, while 4D and 0D again overestimate the 1st and 3rd harmonics (Fig. 3.16 b)) and do not show the higher-order ones.

3.6.2. Motor mode

To each model, a control algorithm in Matlab 2019a was hooked (i_{d1ref}=2, i_{q1ref}=6, i_{d3ref}=1, i_{q3ref}=0.5), however with an ideal power converter to focus just on machine imposed harmonics (geometry and saturation). The resulting command voltages are composed as inputs and shown in Fig. 3.17 a) together with one phase current response in time and frequency domain. The models are in close agreement, as expected the higher harmonic (9th and 11th) content is observed in 5D and 6D models. Torque ripple is not caught by the 0D and 4D models (Fig. 3.17 b)), moreover the 0D model substantially overestimates the

electromagnetic torque. This is a consequence of torque for this model not extracted from the FEM map. In Fig. 3.18 a), the flux linkages in stator reference planes of the 6D model are shown and in Fig. 3.18 b)

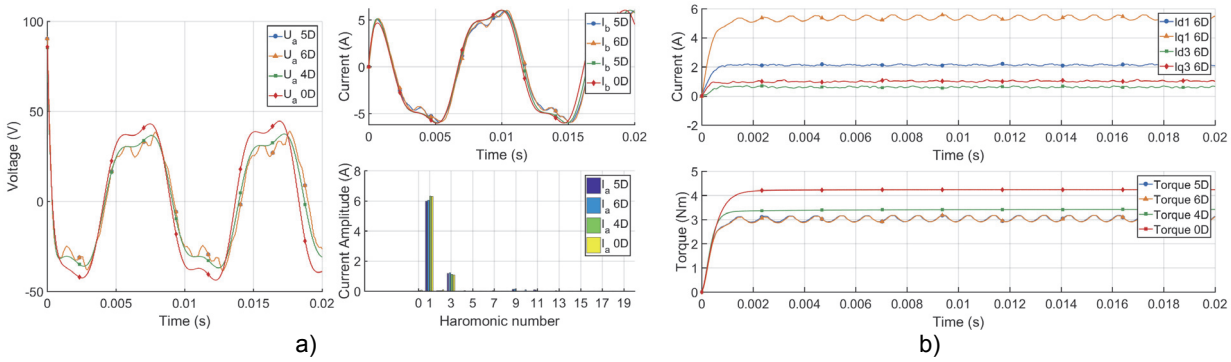

Figure 3.17. Five-five PMasynRM in current control mode a) Applied phase voltage (left), current response (top right) and its FFT print (bottom right), b) *Dq1dq3* current in 6D model (top) and comparison of generated torque (bottom)

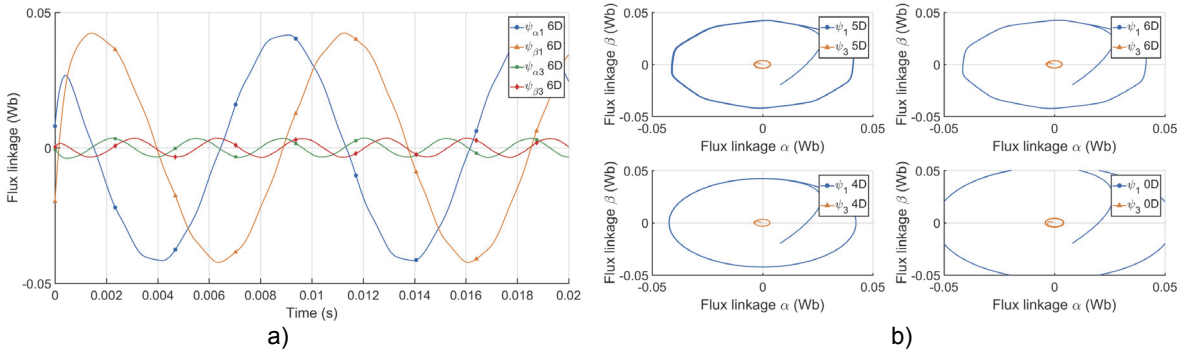

Figure 3.18. Five-five PMasynRM in current control mode, a) *αβ1αβ3* flux linkage waveform in 6D model, b) comparison of flux linkage trajectories

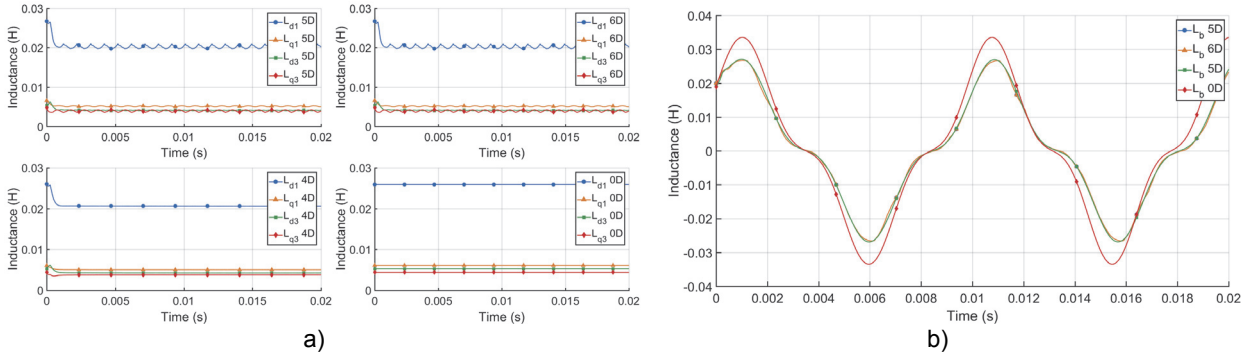

Figure 3.19. Comparison of a) dq1dq3 inductances and b) phase inductaces of a five-phase PMAsynRM

there is a comparison of flux trajectories between all models. The 0D and 4D models exhibit circular paths of the flux linkages in the 1st and 3rd harmonic plane whereas distortions are observed in 5D and 6D models. The inductances in *dq1dq3* are depicted in Fig 3.19 a) and in b) a one phase inductance is illustrated. The phase inductances were derived either directly from models either calculated with help of corresponding

rotators (for 1st and 3rd harmonic plane). Sinusoidal inductances from *dq1* and *dq3* frame result in a not distorted sum (as in 0D and 4D model). It is confirmed that the impact of higher harmonics is only preserved by 5D and 6D models.

3.6.3 Open phase mode

The same open-circuit test with the shaft speed of 200rpm was set for the motor with additional open phase faults. The single-phase, double adjacent, and double non-adjacent phase open were considered. The current waveforms for each case are depicted in Fig. 3.20. Excellent accordance is concluded between transient FEM and the 6D model. The models with high detailing described in the previous section, especially 4D and 5D, are valid only in healthy motor operation. Therefore, the main advantage of the 6D model is the prediction of the motor behavior under faults comprising saturation, winding distribution, slotting effects, and torque ripple.

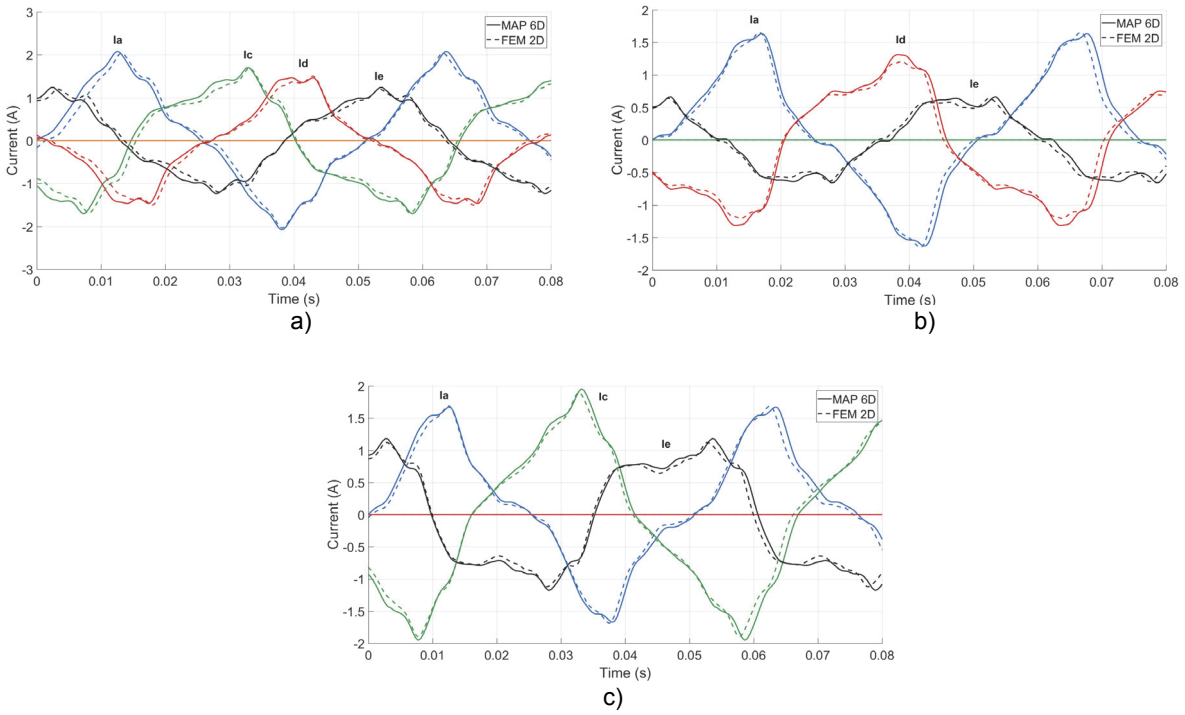

Figure 3.20. Five-phase PMaSynRM under faulty conditions, current waveforms of the 6D model vs FEM, a) B phase open, b) BC phases open c) BD phases open

3.7. FOC control of five-phase saturating PMaSynRM

The vector control algorithm of five-phase PMaSynRM with constant inductances and PM flux was presented in chapter 2.5. Two decoupled planes represent the motor's first and third harmonic in space vector quantities. This decoupling enables the application of standard FOC control for the two planes treated separately [34]. In the case of the constant parameter motor, the control strategies of Maximum Torque per

Ampere (MTPA) and Flux Weakening (FW) are derived directly from the motor equations (2.7) with voltage and current constraints [35]. However, when the parameters are variable (cross-coupling saturation) the inductances depend on all *dq1dq3* stator currents. In this section, a full vector control of cross-wise saturating five-phase prototype PMaSynRM will be presented.

3.7.1. Control strategy

The simplest MTPA approach is derived straight forward for machines with surface mounted magnets where torque decoupling enables the analogical strategy to DC motor control. The outset for synchronous reluctance motor is different since there is an optimal current angle that in the case of the magnet assisted motor is altered by PM flux and cross-saturation makes its identification even more complex. Current trajectories can be calculated from motor behavior maps that are derived from motor voltage equations in combination with voltage and current constraints [62]. This method is effective in implementation for three-phase motors. However, the five-phase PMaSynRM naturally exhibits more degrees of freedom which implies the search for the optimum trajectory more complex. This inspection can be made through an off-line scan of the torque-speed grid seeking the optimum current references in all working conditions. First, the voltage and current limit are set. The maximum RMS current results from the thermal limit and for the five-phase PMaSynRM it is compound by the 1st and 3rd harmonics:

$$I_{\max RMS} = \sqrt{\frac{I_1^2}{2} + \frac{I_3^2}{2}} = \sqrt{\frac{i_{d1}^2 + i_{q1}^2}{2} + \frac{i_{d3}^2 + i_{q3}^2}{2}} \tag{3.21}$$

where I_1 and I_3 stand for the amplitude of the first and third current harmonics respectively. The prototype machine was designed for a maximum RMS current of 7A and a maximum DC-link voltage of 320V. The voltage constraint is defined as follows:

$$\begin{aligned} U_{1\max}^2 &= u_{d1}^2 + u_{q1}^2 \\ U_{3\max}^2 &= u_{d3}^2 + u_{q3}^2 \end{aligned} \tag{3.22}$$

Where U_1 and U_3 stand for the voltage amplitude of the first and third harmonic. The limits of each harmonic depend on the modulation technique[54]–[56]. It may be assumed that the 1st harmonic is limited to 0.6155 of the DC-link, while the 3rd to 0.1453 provided decoupled multiple plane space vector modulation is employed and the phase shift angle between these harmonics is close to π what is equivalent to flat top voltage waveform [32]. In general, the maximum DC-link voltage utilization in a five-phase inverter drive depends also on the power factor. When the constraints are established the torque-speed mesh is generated for torques from 0.1 to 4.8 at the step of 0.1 and the range for angular velocity starts from 125 and ends at 8000 with a step of 100. Then, the iteration of the current sweep is selected. The scan is performed on the cross-saturating flux maps (3.10). These maps are pre-interpolated to achieve a very high resolution

adequate for the evaluation of all current combinations of each torque-speed point. In the procedure, the optimum currents which correspond to the torque point and satisfy the current constraint (3.21) are selected. Then, these candidate currents together with their associated flux linkages (3.10) and torque are evaluated against voltage constraint. The voltages are calculated as in (2.7) but with derivative terms disregarded. The voltage limit (3.22) is checked and if the candidate currents are inside of the boundary then they are

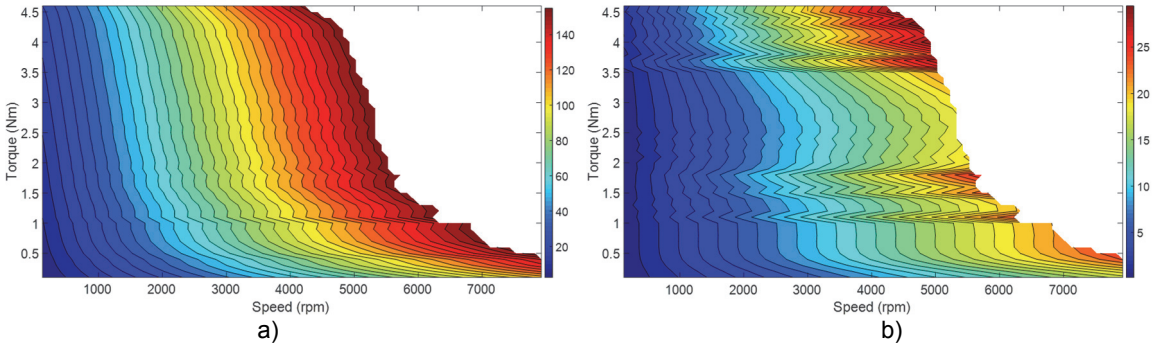

Figure 3.21. Voltage map of the five-phase PMaSynRM, a) 1st harmonic, b) 3rd harmonic

saved and may only be overwritten in another iteration with a lower RMS value. During this procedure, the maximum torque for each speed is obtained and stored in a 1D table. In the speed loop, it will be used to limit the command torque to maximum permissible speed that eventually depends on the DC-link voltage and motor behavior map. The optimum currents are saved in four (*d1*, *q1*, *d3*, *q3*) 2D maps with reference torque and actual speed as inputs provided in the control algorithm. The voltage amplitude of the 1st and 3rd harmonic is illustrated on the torque-speed grid in Fig. 3.21. The third harmonic injection does not have to be necessary in some of the operation regions, however, in such cases, these 3rd harmonics need to be compensated by the control algorithm by imposing 3rd harmonic voltages that accordingly rise with the rotor angular velocity speed-up due to increment of the third harmonic back-electromotive forces which are decoupled in (2.11). So far, the described method to derive motor maps does not consider losses in the iron elements. These losses due to hysteresis and eddy currents take a part of currents in each axis. Their estimation involves further FEM analysis.

3.7.2. Control algorithm

The motor with all non-linearities covered in Chapter 3.4 and its model depicted in Fig. 3.11 is employed as a plant of the control system. The control scheme is illustrated in Fig. 3.21. Currents are measured in four phases (the fifth results from star connection of the motor winding) and transformed to two stationary planes *αβ1* and *αβ3* and then to rotary planes dq1 and dq3 correspondingly fixed to the 1st and 3rd harmonics. The outer speed loop is classically controlled by linear PI which is however saturated against the wind-up mechanism. The saturation of the maximum torque available for current rotor speed is fed back from the control strategy block that derives permissible torque from torque-speed characteristics.

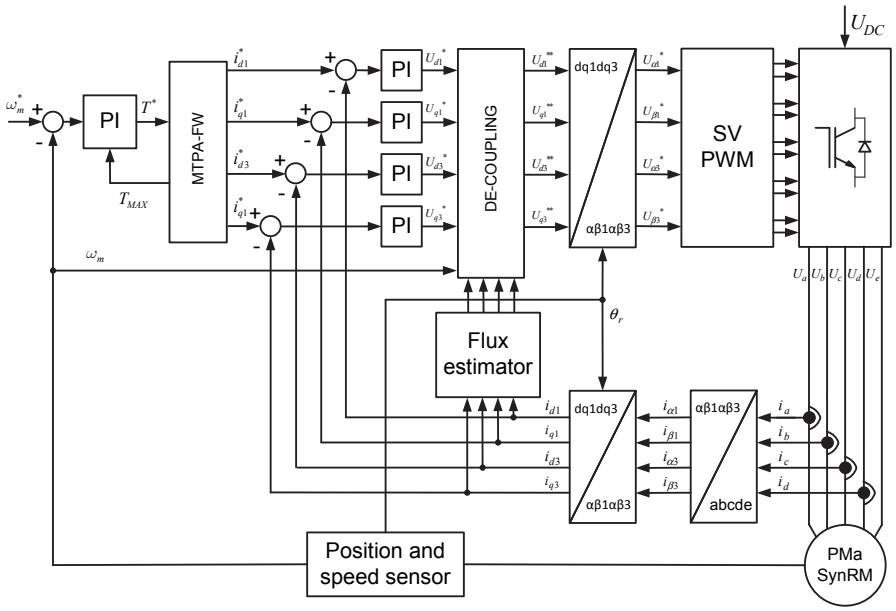

Figure 3.22. FOC control of cross saturating five-phase PMaSynRM

In the same block, the optimum currents provided by the implemented control strategy are calculated. The reference currents are cross-related, each of them contributes to the torque production (no as in S-PMSM). Both *dq* currents in each harmonic plane are as well regulated with PI controllers that generate a set of

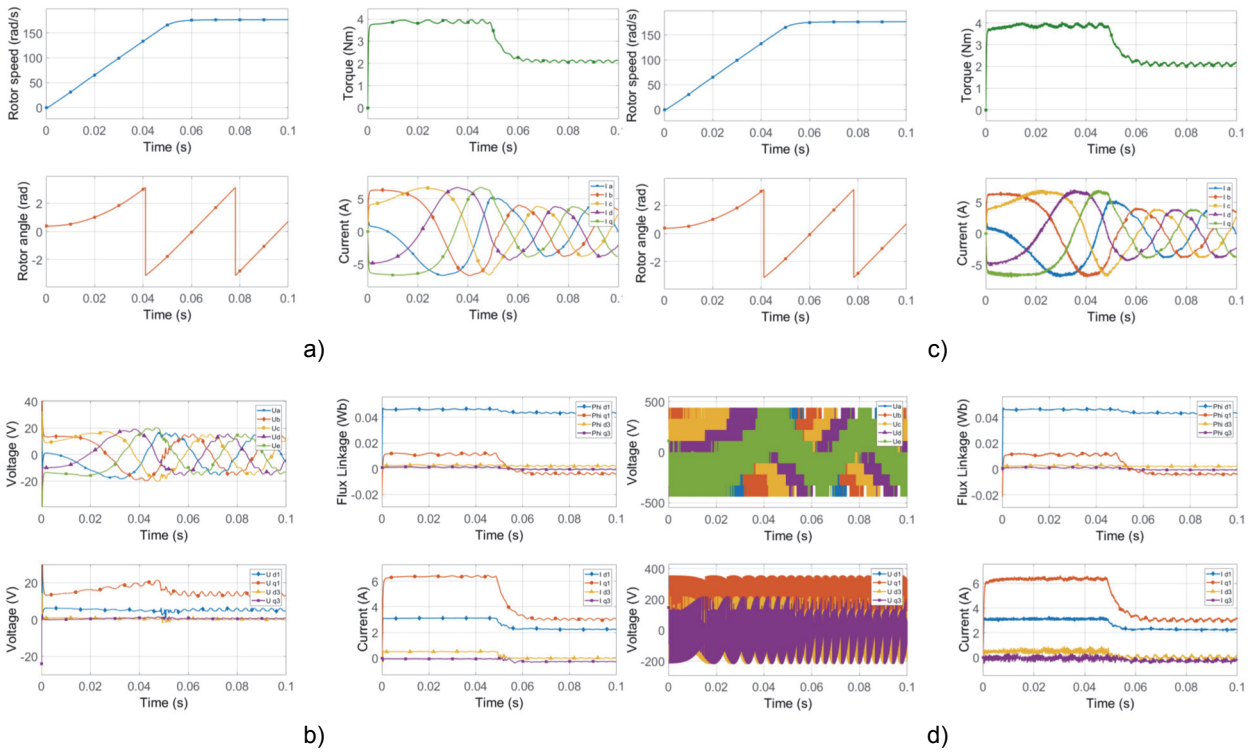

Figure 3.23. Five-phase PMaSynRM control, a), c) velocity, rotor angle, torque and currents, b), d) voltages in abcde and dq1dq3 frames, flux linkages and current waveforms, a), b) ideal power converter, c), d) switched power converter

command voltages that compensate current errors. These voltages need to be corrected with cross-coupling terms as in (2.11), however, the equation for the flux linages (2.8) does not hold any longer due to saturated conditions. Therefore, the flux linkages need to be obtained in the new flux estimator block that implements functions or maps (3.12). The adjusted voltages are ready to be synthesized in the modulator block as in Chapter 2.5.

The entire algorithm was implemented in 4D cross saturation mode i.e. all cross saturations are taken into account. The space harmonics, as discussed in detailed modeling, are present in the machine however they are not compensated by the control algorithm. Several scenarios have been considered. First, a simplified simulation was performed with an ideal power converter and a 5D saturating motor model. The additional harmonic content forced by the power electronic commutation is not present in the ideal converter case, however, the voltages must be distorted due to saturation and space harmonics given in the machine (back-EMF coupling and ripple). The motor was accelerated from standstill to 300 rpm with an applied load of 2 Nm. To accelerate mechanical response time, only the rotor inertia was considered. The same scenario was reproduced with the switched power converter and the switching frequency was set to 20kHz. In Fig. 3.23 the motor response with ideal power converter versus switched mode is shown. The graphs show rotor position, angular velocity, electromagnetic torque, voltage, and current waveforms. Current diagrams show oscillation caused by saturation phenomena and non-ideal field distribution in the airgap. These oscillations are translated to torque ripples. In the case of the ideal converter, the reference voltages are imposed directly on the motor terminals by controlled voltage sources. As expected, the voltage waveforms are as well distorted. The additional ripple provoked by the pulse train in the commutating

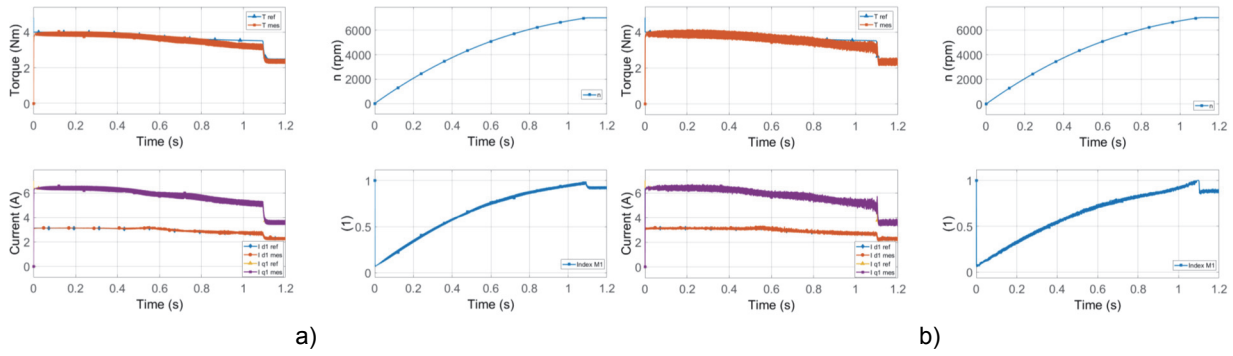

Figure 3.24. Five-phase PMaSynRM control in wide-speed range, torque, speed, current and modulation index, a) ideal power converter, b) switched power converter

power inverter is evident in the switched waveforms and more oscillations are perceived in current waveforms. Next, the response in wide speed was observed, the motor was accelerated from standstill to 7000 rpm. In Fig. 3.24 the speed, torque, currents, and modulation index are depicted for the ideal power converter (a) and the switched-mode (b). With the proposed algorithm the torque reference is followed in

the low and high-speed range provided the bandwidth of the PI regulators is high enough. The maximum torque from the torque-speed map is achieved in all working conditions.

3.8. Conclusions

New type of modeling of PMaSynRM motors was described in this chapter. The cross saturation 2D and space harmonics 3D were first implemented in the three-phase motor model. Then, the concept was extended to five-phase PMasynRM, which 4D model includes not only the classical cross-coupling but also traverse coupling between 1st and 3rd harmonic spaces. The inclusion of the field harmonics requires increment of dimension to 5D with the benefit of the non-sinusoidal winding distribution and cogging torque prediction.

A new 6D model with saturation induced and airgap field harmonics was elaborated in the stator phase description i.e. *abcde* phase quantities. It also covers iron saturations since flux linkages of each phase depend on currents from all phases, thus mutual saturation is reflected in the model. A comparison between previous models – 0D with constant parameters, 4D with cross harmonic saturations, 5D with additional space harmonics, and the 6D against transient FEM was performed. The non-sinusoidal winding distribution and the cogging torque may only be included when the flux linkages are obtained in function of the rotor position. The initial flux linkage also depends on the rotor angle. Higher the number of dimensions invokes longer computational time and exponentially more memory resources. The 6D model gives the best accuracy and offers additional benefit of the open phase faulty scenarios, which is impossible to predict by lower order models. The 5D model can be considered as a good compromise between precision and size.

Lastly, a control algorithm for a cross saturating five-phase PMaSynRM was implemented. The control strategy was developed from the motor behavior map computed from the flux maps established from the FEM analysis. It has been demonstrated that the control algorithm guarantees excellent tracking of the reference values in a wide speed range. The feasibility of the proposed algorithm was shown in a study with the ideal and switched-mode power converter.

4

4. Axial skew interface in PMaSynRM model

This chapter discusses methods to correct flux maps due to axial asymmetry provoked by rotor skewing. Two methods are proposed to account for the sliced rotor layout in the multi-plane and natural reference frame models. The experimental evaluation is carried on the test bench with a manufactured five-phase PMaSynRM prototype.

CONTENTS:

4.1. Introduction

The PMaSynRM machines exhibit three types of torque components, namely the field alignment, reluctance, and cogging torque. Field alignment is due to the interaction of magnets and stator MMF produced by currents flowing in the winding. Reluctance originates from the saliency in the rotor structure and this component is dominant in PMaSynRM. The cogging torque can be also attributed to local reluctance change and field attraction to the alternating detent and slotted iron structure. Additionally, the non-sinusoidal winding distribution and non-sinusoidal field in the airgap appear in the high harmonic content of the back EMF waveforms and thus provoke torque ripples. Additional higher-order harmonics are introduced by switching in the power electronic converter. The cogging component sums up to the electromagnetic torque and results in undesired vibrations and noise emission [63]. To minimize torque ripples the stator winding distribution may be optimized [64]. More sinusoidal distribution results in smooth torque generation. Another measure to minimize airgap field harmonics is well accepted in the industry and it is based on the introduction of axial skewing in stator or rotor mechanical design [65]. Usually, for the sake of lower production costs, the segmented step skewing is selected [66]. The rotor skewing is preferred also for simplicity and cost reduction. The rare-earth free five-phase PMaSynRM technology may be also equipped with the skewing segments. Nevertheless, the axial asymmetry makes the modeling even more challenging. The best precision is offered by 3D FEM analysis. However, the geometry of the sliced rotor is complex and the computation load is very high [67]. A common approach is to use the so-called 2D multi-slice FEA technique [68], [69]. In this method, the motor cross-section layout is replicated n times along the axial length. Each replica represents one skew segment of length l/n where l is the stack length. Every segment is shifted by the skew angle β. The finite element models are coupled electrically. Although 2D multi-slice is simplified it remains computationally intensive, especially with a higher number of segments [70].

So far, as described in Chapter 3 the flux map extraction from 2D FEM and consequent inversion to obtain current maps has become a very interesting option as it offers the best compromise between precision and computation time. The introduction of the skewing concept however makes the multidimensional modeling described in Chapter 3 even more complex since all approaches are valid only to the axially symmetric motor and do not include skewing. The analytic correction factor accounting for skewing was proposed in [71] and [72], however, the axial steps in saturation due to segmentation were neglected. A method to comprise axial saturation was proposed in [73] for a three-phase IPMSM motor resulting in good performance prediction close to 2D multi-slice FEM. In this chapter, a new model of the five-phase PMaSynRM accounting for skewing in the combination of cross-saturations and nonlinear field spectrum will be elaborated.

4.2. Skewing in 5D multi-plane maps of healthy motor

In Chapter 3 the investigated motor was axially symmetric. The flux map derived from 2D static FEM will be used to calculate flux linkages of the 1st and 3rd harmonic in all *n* skewing segments. To achieve axial permeability distribution in discrete steps, the appropriate harmonic rotators will be applied. The validity of the proposed method will be contrasted vs the 3D FEM model and checked in the experimental setup. The model is elaborated on the prototype five-phase PMaSynRM motor with parameters from Table

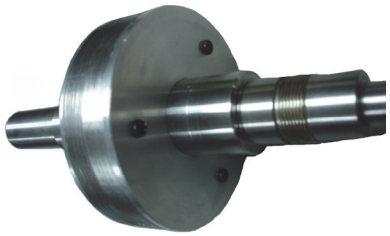

Figure 4.1. Skewed rotor with 2 segments of the five-phase PMaSynRM motor

3.1 and skew angle β of 6 mechanical degrees. In Fig. 3.9 the cross-section, stator assembly, and rotor layout are depicted and in Fig. 3.24 the actual rotor with two segments is shown. They are perforated and assembled by three soft magnetic screws. The skewing results in different flux density distribution in each

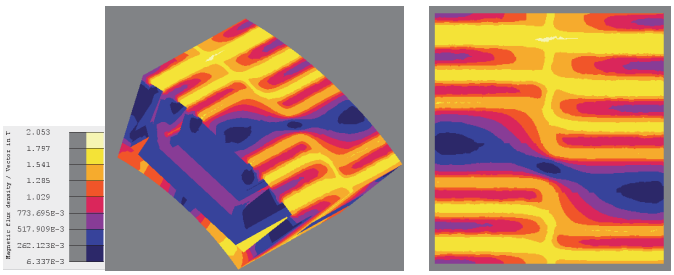

Figure 4.2. 3D FEM diagram of flux density distribution in the five-phase prototype motor

segment as illustrated in Fig. 4.2, where besides a shift, a soft fringing transition between two slices is observed. The flux curvature is neglected so in this analysis the flux distribution is uniform in every segment.

The modeling starting point is the axially symmetric 5D model based on flux map inversion described with the voltage equation (3.11), 5D flux maps (3.12) and 5D torque (3.13) acquired from the FEM scan of the 2D geometry with active stack length equal to total motor length divided by 2 (no. of skew segments). The model is depicted in Fig. 3.11. It should be recognized that the flux and torque maps (3.12) and (3.13) actually need to be replaced by corrected maps that comprise the skewing effect. The maps of (3.12) and (3.13) were calculated with defined coordinate space vectors of the 1st and 3rd harmonic plane $\vec{I}_{dq1}$ and $\vec{I}_{dq3}$ These ranges should be extended to cover rotating currents in both slices:

$$\vec{I}_{dq1(11)} = \vec{I}_{dq1} \cup \vec{I}_{dq1} e^{-jp\beta}, \quad \vec{I}_{dq3(11)} = \vec{I}_{dq3} \cup \vec{I}_{dq3} e^{-3jp\beta} \tag{4.1}$$

where $\vec{I}$ denotes the space vector of the 1st or 3rd harmonic plane and (xx) subscript the first digit stands for "of the x-th" slice and the second digit "seen by the x-th slice". Therefore, the FEM scan to obtain flux maps of the first segment $\vec{\psi}_{dq1(11)}$ and $\vec{\psi}_{dq3(11)}$ (and torque $T_{e(11)}$) is performed on the extended coordinate vectors in order to cover primary current vectors seen by the next slice. These current references (4.1) of the first segment are transformed with the rotator operation to attain the same current but seen by the second segment:

$$\vec{I}_{dq1(12)} = \vec{I}_{dq1(11)} e^{-jp\beta}, \quad \vec{I}_{dq3(12)} = \vec{I}_{dq3(11)} e^{-3jp\beta} \tag{4.2}$$

It should be noted that for the second segment the current vector of the 1st harmonic is electrically rotated with the angle $p\beta$ while the shift of the 3rd harmonic is $3p\beta$. Now it is possible to calculate the flux linkages

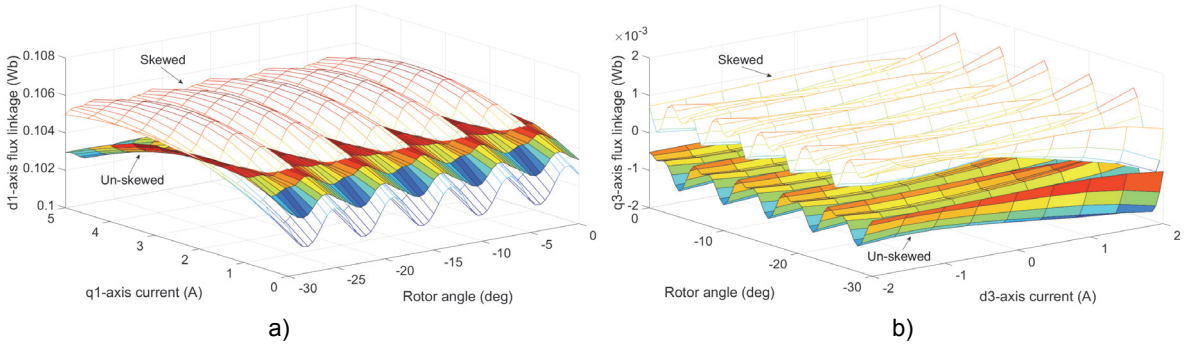

Figure 4.3. Five-phase PMaSynRM flux linkage 5D map with skewing a) ψ_{d1} at $i_{d1} = 5$, $i_{d3} = i_{q3} = 0$, b) ψ_{q3} at $i_{d1} = 0.5$ $i_{q1} = 4.5$

of the second segment $\vec{\psi}_{dq1(22)}$ and $\vec{\psi}_{dq3(22)}$ which are interpolated from the first segment maps $\vec{\psi}_{dq1(11)}$, $\vec{\psi}_{dq3(11)}$ with query points of the currents in the second segment (4.2) and appropriately shifted rotor angle θ_r (accordingly to the segment number and harmonic index). The torque of the second slice $T_{e(22)}$ is obtained analogically. Now the flux linkages of the second segment can be rotated back to the first segment:

$$\vec{\psi}_{dq1(21)} = \vec{\psi}_{dq1(22)} e^{jp\beta}, \quad \vec{\psi}_{dq3(21)} = \vec{\psi}_{dq3(22)} e^{3jp\beta} \tag{4.3}$$

This operation is needed to get all flux linkages referred to the first segment so it is possible to sum them and get the total flux linkages of the skewed motor:

$$\vec{\psi}_{dq1} = \vec{\psi}_{dq1(11)} + \vec{\psi}_{dq1(21)}, \quad \vec{\psi}_{dq3} = \vec{\psi}_{dq3(11)} + \vec{\psi}_{dq3(21)} \tag{4.4}$$

The resultant electromagnetic torque is also equal to the sum of the torque generated by each slice:

$$T_e = T_{e(11)} + T_{e(22)} \tag{4.5}$$

The flux linkages of the 1st and 3rd harmonics (4.4) and the torque (4.5) are stored as 5D function or LUT in the same way as (3.12) and (3.13). However, the maps of (4.4) and (4.5) account for not only the space harmonics and saturation but also skewing in the rotor and its impact on the PMaSynRM nonlinear parameters. The flux map sections depicted in the function of current and mechanical angle are shown in Fig. 4.3. The original maps (not comprising skewing) are contrasted with the new maps corrected by the described procedure for the prototype five-phase PMaSynRM with two rotor segments.

One can note that the global zero electrical position of the skewed motor does not necessarily coincide with the first skew segment zero position. For example, a two-stepped rotor of the prototype machine represent such a case and ideally, the zero position falls in the geometrical mean between the zeros of each slice. Some 3D effects (the end winding and segment transitions) can slightly move it from the symmetrical mean. Such a shift can be predicted by the 3D FEM only. The flux maps from the 3D FEM, however, are out of scope because of the computational load and the zero angle shift is minor. In general, the reference flux maps can be calculated with dq1dq3 currents referred to the real zero position of the skewed prototype motor. In this case, the procedure is a bit more complex as it requires a projection of the current vectors to the first segment (with angles $-p\beta/2$ and $-3p\beta/2$) and the second segment (with angles $+p\beta/2$ and $+3p\beta/2$). The described procedure can be adjusted and applied to multi-phase PMaSynRM (or IPMSM) motors with any rotor layout and an unrestricted number of skewing sliced N.

4.2.1. FEM comparison

The model schematic is shown in Fig. 3.10. It is based on (3.11) and the flux linkages are calculated with (4.4) and consequently inverted and the torque map (4.5) is implemented. The FEM model was created in Altair Flux 12.3 and the 5D skewed model was built in Matlab 2019a environment. The motor

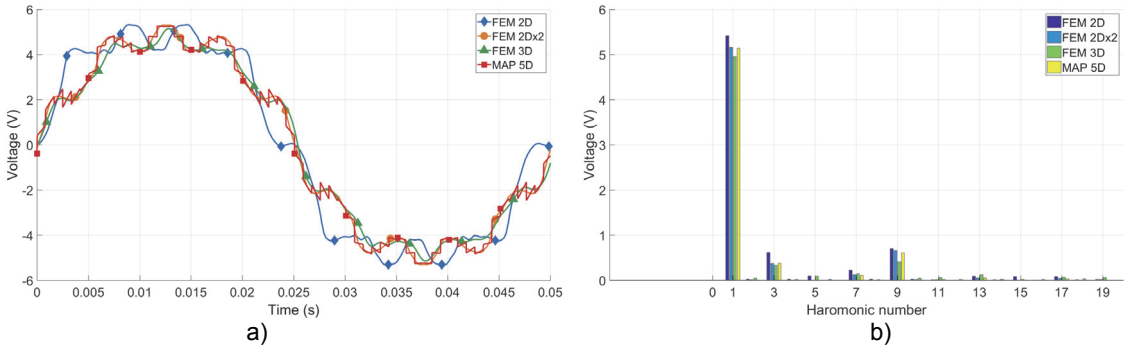

Figure 4.4. Phase A back-EMF of the prototype skewed PMaSynRM, a) waveform b) FFT

back-EMF was captured at a constant rotor velocity of 200rpm. Its waveform and FFT transform is shown in Fig. 4.4 (compare with Fig. 3.15). There is a very good agreement between multi-slice 2D FEM, 3D

FEM, and the skewed 5D map model. Especially, a very close response is observed between skewed 5D and multi-slice 2D FEM, which is logical for the sake of the flux map extraction from a single slice 2D FEM. Thus this result is considered to be very precise.

4.2.2. Experimental validation

In the experimental setup, the five-phase PMaSynRM prototype machine was mounted on the test bench. The drive consists of Siemens SC 120 Control with Smart and Single Motor Modules. The currents are measured in five phases by LEM IT 65-S and the voltages are monitored by CV3-1000 sensors. All

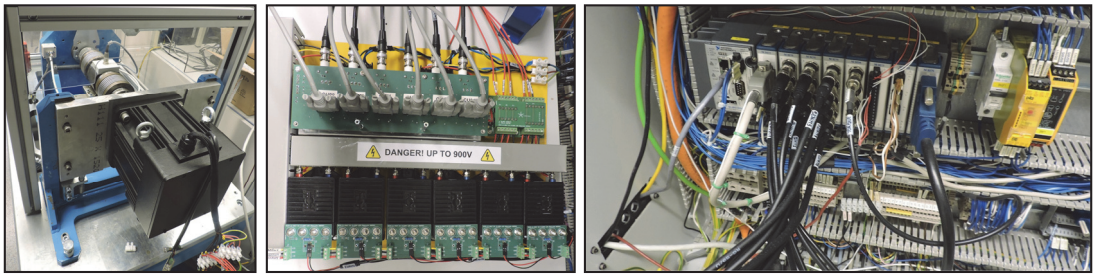

Figure 4.5. Experimental test bench: prototype machine, signal monitoring and conditioning, and acquisition box

signals are captured by analog inputs NI9234 connected to the NIcRIO real-time controller. The rotor angle is measured with Hengstler RI76TD 9000 lines/rev encoder. All measurement data is synchronously sampled using embedded LX50FPGA resources. The measurements are saved in binary files ready for importation and post-processing in the Matlab environment. The experimental drive bench is depicted in Fig. 4.5.

The motor was accelerated from a standstill in the short-circuit condition. The reference speed was adjusted by the commercial controller to 200rpm. The target of this test was to include the initial condition, transient response, and the steady-state behavior of the motor in certain operation modes and then compare

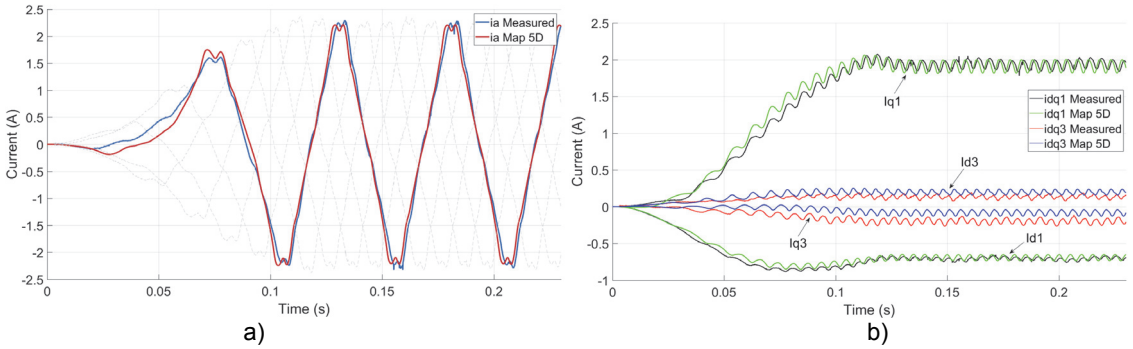

Figure 4.6. Comparison of experimental and 5D skewed model predicted currents at 200rpm, a) phase currents b) dq1dq3 currents

the experimental results with those predicted by the 5D model elaborated in this investigation. The measured and simulated results of the current waveforms are depicted in Fig. 4.6. The waveforms are shown in stator phase and *dq1dq3* reference frame and they match very well, what proves the fidelity of the skewed

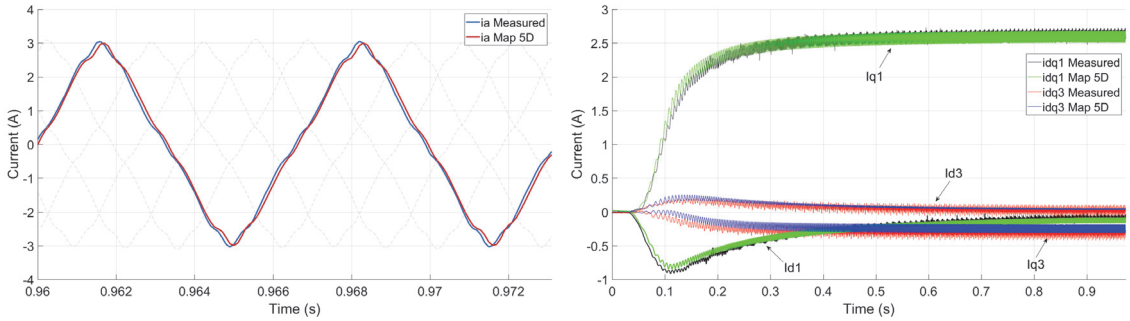

Figure 4.7. Comparison of experimental and 5D skewed model predicted currents at 2000rpm, a) phase currents b) dq1dq3 currents

5D modeling combined with space harmonics and cross saturations. Another scenario with the rotor accelerated to 2000 rpm is depicted in Fig. 4.7. Higher speed imposes higher current and thus lower permeability. The waveform change is observed accordingly in the motor response in the experimental setup as well as in the 5D skewed modeling. There is very little disparity perhaps due to interpolations that potentially could be further reduced with higher flux map step size. Another source of divergence comes from the prototype manufacturing tolerances (mechanical pieces, B(H) curve and, magnet remanent magnetization) and defects such as eccentricities and phases not perfectly balanced. Nevertheless, these imperfections in the prototype do not discard the validity of the model.

4.3. Skewing in 6D healthy and open phase faulty motor

The model developed in Section 4.2 is a skewed counterpart of the model in Section 3.4 and the latter one does not include the skewing. As already stated, the modeling in *dq1dq3* reference frames has resulted in very close to FEM precision, however only for the healthy motor conditions. For this reason, the model in natural *abcde* reference of the five-phase PMaSynRM was introduced in Section 3.5. This model accounts for the nonlinear air-gap field, slotting harmonics, and mutual saturations possible to predict in open-phase conditions. However, the skewing is not considered. In this section, the 6D model flux maps will be corrected to add axial asymmetry originated from skewing. Thus, it will be possible to evaluate the prototype skewed motor in single and double open phase scenarios with no loss of the nonlinear effects.

The cross-section, stator assembly, and rotor layout are depicted in Fig. 3.9 while in Fig. 4.1 the rotor with two segments is shown. This is the prototype motor of this study and the flux density of its rotor is illustrated in Fig. 4.2, where the flux distribution is axially non-uniform. The axially symmetric 6D model

based on the flux map inversion is used for the 6D modeling with skew. The model is described with the voltage equation (3.16) and 6D flux linkage maps (3.17) and 6D torque map (3.18) calculated in 2D FEM. To complete the model, the flux maps are inverted to obtain 6D current maps (3.20). The model scheme is depicted in Fig. 3.14. Until now, this approach can be implemented within the symmetrical flux distribution. To cover skewing in multiple-segmented rotor or stator, the flux maps (3.17) and the torque map (3.18) should be modified to include axial asymmetry. Since the prototype five-phase PMaSynRM motor contains a rotor with two segments, the procedure to include skewing will be shown in its example, however, it generally can be applied to any number of skewing segments. In terms of modeling, the motor discrete (segmented) skewing can be represented as several motors connected in series. Therefore, for every phase, the resultant total motor phase flux linkage can be calculated as a sum of the fluxes of each slice. The flux linkages and torque 6D maps are identified through the 2D FEM scan for the first slice (axially symmetric) and are referred to as $\psi_{x(1)}$ and $T_{(1)}$ respectively. For the sake of simplicity, the first slice is assumed to be located at the rotor angle $\theta_r = 0$. The second slice is displaced with respect to the first slice by the angle of mechanical shift β (electrically $p\beta$) equal to 6 deg. Therefore, the fluxes of the second slice $\psi_{x(2)}$ and its torque $T_{(2)}$ can be read out from the 6D maps of the first slice $\psi_{x(1)}$ and $T_{(1)}$ with the appropriate angle $\theta_r + p\beta$. This process is repeated for the complete rotor turn and the fluxes and torques of the two segments can be added to get new total fluxes and torque of the skewed motor:

$$\begin{aligned} \psi_{x-new} &= \psi_{x(1)} + \psi_{x(2)} \\ T_{new} &= T_{(1)} + T_{(2)} \end{aligned} \tag{4.6}$$

These new maps replace maps of (3.17) and (3.18). The new 6D current maps are obtained through the 6D inverse of the flux maps and then they are embedded in the model of Fig. 3.14.

4.3.1. Experimental validation

The experimental setup motor and measuring devices are described in Section 4.2.2. The same scenario with the motor speed settled at 200rpm was reproduced in the test bench with single and double open phase fault. The same conditions were simulated with the 6D skewed motor model and its maps derived as in (4.6). In Fig. 4.8 a comparison between 6D-skewed model predicted waveforms and experimental measurements is shown in scenarios of single open phase, two adjacent, and two non-adjacent. The simulated waveforms, considering so many non-linear components, match very well the monitored signal in the test bench. Further in Fig. 4.9, the phase currents in the BD open scenario are depicted in the frequency domain. Surprisingly, the first harmonic in measured waveforms is slightly higher than in the simulated model. Nevertheless, the spectrum of the simulated model very well reflects the reality from the measurements. The same higher-order harmonics are visible in Fig. 4.9. It shows how the skewing changes

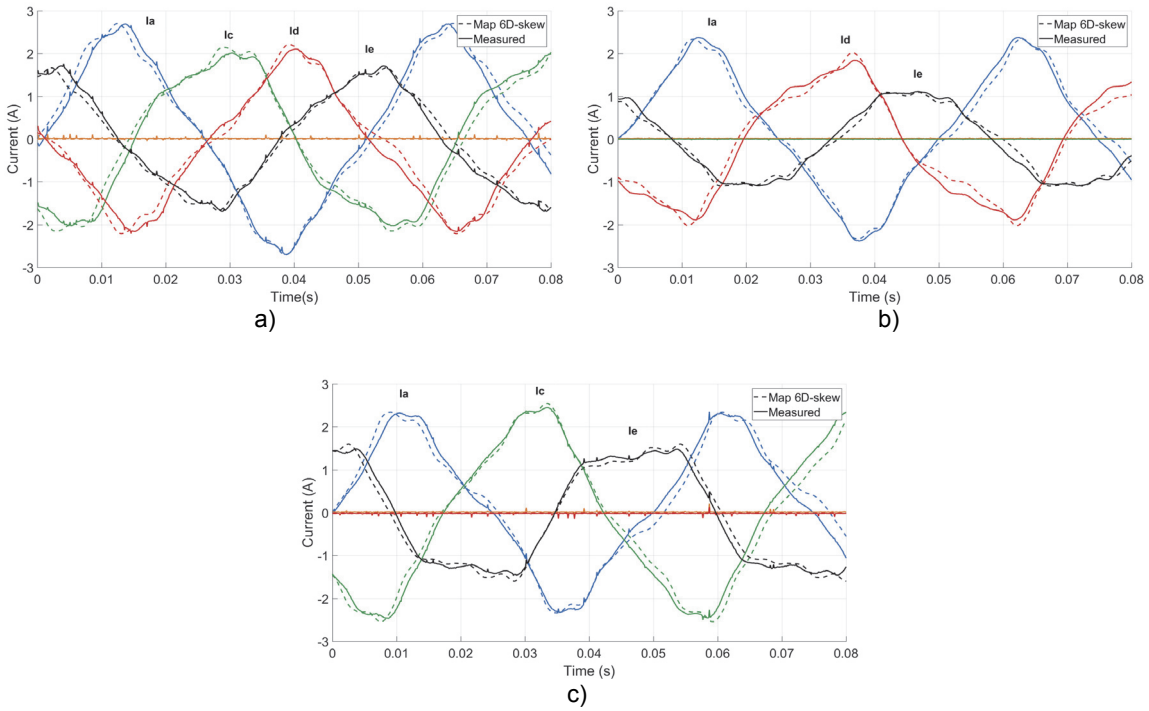

Figure 4.8. Five-phase PMaSynRM under faulty conditions, current waveforms of the 6D skewed model vs measurement, a) B phase open, b) BC phases open c) BD phases open

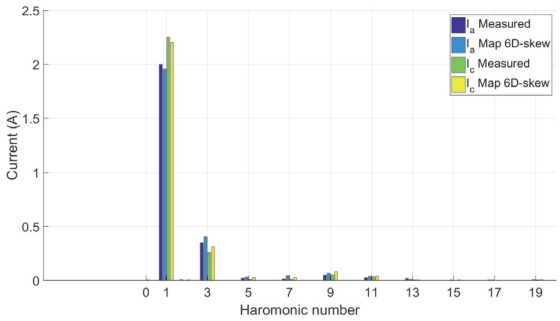

Figure 4.9. Five phase PMaSynRM current waveforms in frequency domain in non-adjacent phases open scenario

the dynamic behavior of the motor (see Fig. 3.20). The imperfections in the model originate from the discretized flux maps and interpolations between points. On the other hand, the prototype motor may have slightly different parameters than the FEM based model used for the flux map extraction due to:

- B(H) characteristics of the laminated stator (only first saturation curve considered in the model)
- Eddy currents in iron and magnets are not considered in the model
- Mechanical tolerances, displacement in collocation of magnets, and skew segments
- Eccentricity in the rotor shaft assembly

4.4. Conclusions

In this chapter new models of skewed five-phase Permanent Magnet Assisted Synchronous Reluctance Motor were derived. The first 5D one is developed in rotating reference frames fixed with the first and third harmonic components of the air-gap field, and the second 6D one is described in the natural stator phase quantities. Both modeling approaches comprise cross-saturation effects, air-gap field distortions, slotting effects (and discrete winding distribution) together with discrete axial skewing. The original flux maps are calculated in FEM for one skewing segment and then accordingly contribution of the consecutive segments is computed and projected to the new adjusted flux maps accounting for the full skewing. In the corrected 5D model both rotators of the 1^{st} and 3^{rd} harmonics need to be considered. In the 6D, model the shift of fluxes is derived from the rotor angle dependence. The modeling has been verified by transient FEA and experimental measurements. Very good agreement is observed for transient behavior with both models while the 6D can also predict open phase scenarios.

5

5. Multiphase PMaSynRM model with “Virtual Reluctance” map

This chapter introduces a novel PMaSynRM model established with the conversion of the flux maps to “virtual reluctance” maps. A discussion of the model sensitivity and singularities is provided. The performance of the proposed model is contrasted with the previous ones and evaluated with FEA and experimental test campaign. Finally, the advantages of the new model over the inverted flux maps are highlighted.

CONTENTS:

5.1. Virtual reluctance 5D multi-plane healthy PMaSynRM motor model

The models developed in Chapters 3 and 4 are proved to be credible along with FEA and experimental validation. However, they rely on the precise flux map inversion. The inversion itself is a cumbersome process for several reasons. Firstly, the inverted function may not exist due to the lack of bijection of the flux map. Secondly, the inversion of higher-order maps carries an accuracy shift which increases with dimension number more than 3, and thirdly the methods to invert flux maps require very long computational time. These were the motivating factors to propose a novel modeling method that would avoid the flux map inversion. Thus, the virtual reluctance concept was elaborated. It offers very high accuracy, does not suffer from residual flux drift and its pre-calculation is very fast. In this section, the concept will be developed for a five-phase PMasynRM model in dq1dq3 reference frames i.e. 5D approach.

To characterize the virtual reluctance concept, first the magnetic reluctance $\Re$ is defines as:

$$\Re = \frac{F}{\psi} \tag{5.1}$$

Where F stands for the magnetomotive force (MMF) and ψ is the flux flowing through the reluctance component. The MMF results from the effective ampere-turns and is a magnetic voltage. Actually, within one coil turn, the reluctance as defined in (5.1) is reciprocal to inductance. Therefore, it should be possible to mathematically describe motor equations with help of reluctances as inverted apparent inductances such as described in Section 3.1.1. This method results valid for a three-phase motor in which apparent inductances can be found to be always positive with proper fixation of the permanent magnet flux. However, for a five-phase PMasynRM, the separation of the permanent magnet flux in the 1^{st} and 3^{rd} harmonic cannot suffice for the apparent inductances to be strictly positive. Thus, with the apparent inductance approach, the model will suffer from singularities at some points of operation. To overcome this problem, virtual reluctance is proposed and defines as:

$$\Re = \frac{i + k_1}{\psi + k_2} \tag{5.2}$$

where the coefficients k_1 and k_2 stand for the translation of the current vector and flux map respectively. The virtual reluctance can be calculated for every current flux pair that was used for the primary flux map extraction (3.12). The virtual reluctances for the 5D model are computed accordingly:

$$\Re_{dn} = \frac{i_{dn} + k_{1dn}}{f_{dn}\left(i_{d1}, i_{q1}, i_{d3}, i_{q3}, \theta_r\right) + k_{2dn}} \tag{5.3}$$

$$\Re_{qn} = \frac{i_{qn} + k_{1qn}}{f_{qn}\left(i_{d1}, i_{q1}, i_{d3}, i_{q3}, \theta_r\right) + k_{2qn}}$$

where i_{dn} and i_{qn} stand for the self-exciting currents of the corresponding virtual reluctance in the d and q axis for each harmonic. The flux linkage functions f_{dn} and f_{qn} are calculated through multi-static FEM analysis as in (3.12), and they depend on all currents and the rotor position. Therefore, the cross saturations

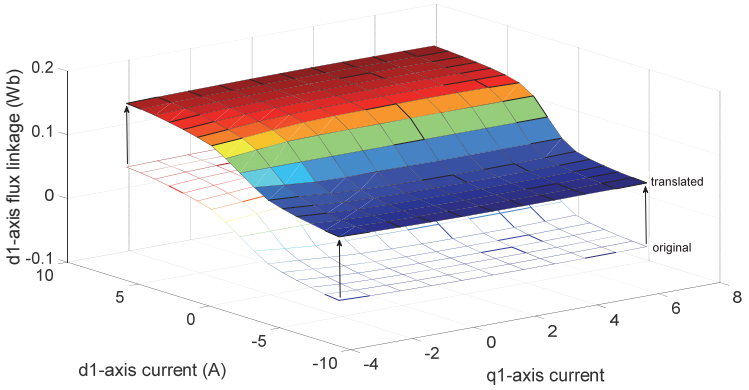

Figure 5.1. Primary and translated *d1* flux map at i_{d3}=*0* A, i_{q3} =*0* A and rotor position =0 rad.

and space harmonic content is preserved in the virtual reluctance maps. An example of translation is depicted in Fig. 5.1 where the original flux map is illustrated together with its translation. It is shown that the shifted map is above the ZO plane so there are no negative elements. This is essential to avoid singularities in the time-stepping simulation. The coefficient k_2 must satisfy the condition of being higher than the absolute of the minimum value of the whole flux map. On the other hand, k_1 moves the self-current coordinate to the positive side, thus together with properly selected k_2 , it guarantees the resultant reluctances (5.3) to be always positive. The k_2 , therefore, needs to reach the value of the absolute of the

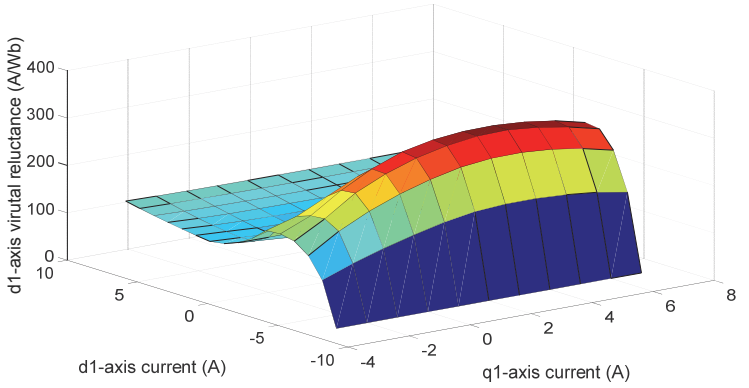

Figure 5.2. Virtual reluctance map in *d1* axis at i_{d3}=*0* A, i_{q3} =*0* A and rotor position =0 rad.

lowest current coordinate in the whole flux linkage map. The corresponding example of the virtual reluctance map to the flux map in Fig. 5.1 is depicted in Fig. 5.2. Once the flux maps are obtained, the

computation of virtual reluctances is virtually instant. The motor model (3.11-3.12) based on inverted flux maps is reconstructed, the inverted flux maps are replaced by the current calculation from the virtual reluctance maps:

$$\begin{aligned} i_{dn} &= \left[\int \left(U_{dn} - R_s i_{dn} + n\omega_r \psi_{qn}\right)dt + k_{2dn}\right]\cdot \Re_{dn} - k_{1dn} \\ i_{qn} &= \left[\int \left(U_{qn} - R_s i_{qn} - n\omega_r \psi_{dn}\right)dt + k_{2qn}\right]\cdot \Re_{qn} - k_{1qn} \end{aligned} \tag{5.4}$$

The coefficient k_2 is decoupled to offset the flux linkage calculated from the voltage integral and then the k_1 compensates the offset of the resulting current. This way is numerically stable, the singularities are

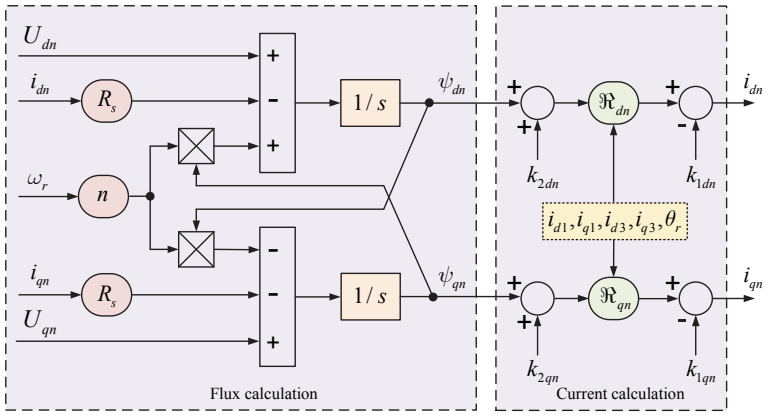

Figure 5.3. PMaSynRM model based on virtual reluctance map in rotating reference frames.

avoided and the algebraic loop can be easily handled by the state-of-the-art solvers (e.g. used in Matlab Simulink). The model is depicted in Fig. 5.3 with separated flux linkage computation and current calculation from the obtained fluxes.

5.1.2. Implantation of skewing in harmonic fixed frames

In Chapter 4 the axial skew interface was introduced to correct the flux maps and account for magnetic axial asymmetry introduced by segmented rotor construction. The same procedure can be used before the virtual reluctances are calculated. Therefore, the virtual reluctance as well may additionally include the skewing effect. In Fig. 5.4 a diagram of the algorithm to include two-segmented skew is illustrated. The inputs are the vector coordinates for which the flux maps were extracted $\left[i_{d1}, i_{a1}, i_{d3}, i_{q3}, \theta_r\right]$. These coordinates are projected in two local coordinates of each segment using Concordia transformation:

$$\vec{k}_{dqn(x)} = \vec{k}_{dqn} e^{-njp\beta_{(x)}} \tag{5.5}$$

where k represents the space vector of the n-th harmonic plane, *(x)* stands for the skewing segment, and β is the skewing mechanical angle. Then, the flux maps of each segment are interpolated from the primary

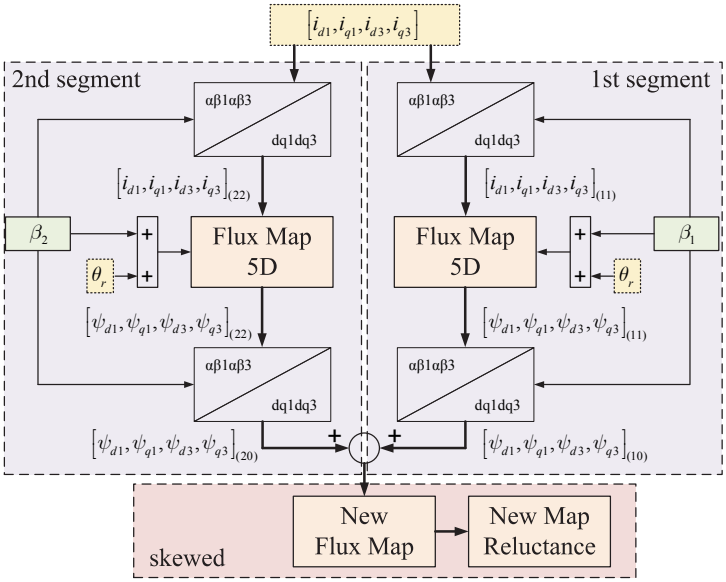

Figure 5.4. Algorithm to calculate 5D skewed virtual reluctance maps

axially symmetric map with the local current coordinates and the shifted rotor angle. Eventually, the local flux linkages are rotated back and summed to give the full flux linkage of the skewed motor:

$$\vec{k}_{dqn} = \vec{k}_{dqn(1)} e^{njp\beta_{(1)}} + \vec{k}_{dqn(2)} e^{njp\beta_{(2)}} \tag{5.6}$$

Finally, the 5D skewed flux map is used to calculate reluctance map such as in (5.3), however this time the reluctances account for the discrete skewing effect. An example of the skewed VR map is given in Fig. 5.5.

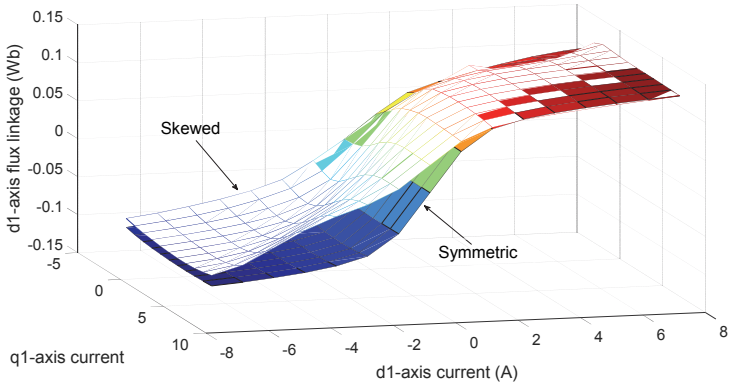

Figure 5.5. Example of un-skewed and skewed 5D virtual reluctance map

5.2. Virtual reluctance 6D healthy and open phase faulty PMaSynRM motor model

The 6D flux map inversion is even more prone to accuracy errors, takes a much longer time to calculate, and may be indefinite. The concept of the virtual reluctance proposed in Section 5.1 can be adapted to be

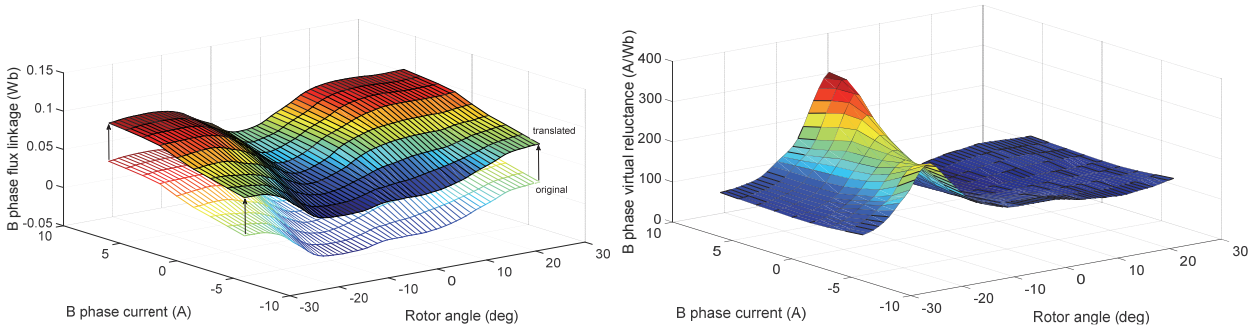

a) b)

Figure 5.6. Primary and translated a) *a-phase* flux map and b) virtual reluctance map at $i_a = i_c = i_d = i_e = -3$ *A.* and rotor position =0 rad.

implemented within the motor description in natural phase quantities. Thus, every phase of the five-phase PMaSynRM has its associated virtual reluctance calculated as following:

$$\Re_x = \frac{i_x + k_{1x}}{f_x\left(i_a, i_b, i_c, i_d, i_e, \theta_r\right) + k_{2x}} \tag{5.7}$$

where f_x is an *x*-phase flux linkage function dependent on all currents and rotor position, the coefficients k_{2x} and k_{1x} stand for the translation vector components (similarly as in the 5D case). The primary and shifted flux map example is depicted in Fig. 5.6 a) while its interrelated virtual reluctance map is shown in b). The electromagnetic torque is interpolated from the FEA extracted torque map (3.18). Then, the mechanical system is modeled along with the II Newton principle:

$$\omega_r = \int \frac{T_e - T_L - D\omega_r}{J_r} dt \tag{5.7}$$

where T_L stands for the load torque, J_r is the rotor and load inertia, and D represents the viscous friction factor proportional to the angular velocity. The motor model schematic is depicted in Fig. 5.7.

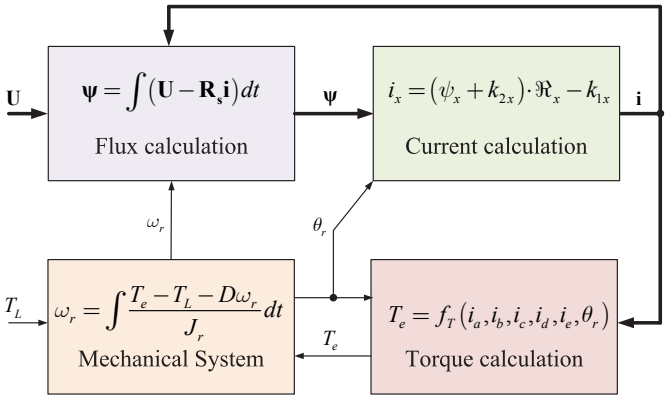

Figure 5.7. PMaSynRM model based on virtual reluctance map in abcde natural reference.

5.2.1. Skewing in natural reference frame

As was discussed in Section 5.1, the skewing technique is widely adopted in the motor design to reduce torque ripples. The VR map in the 6D model can as well be corrected to contemplate the skewing effect. Similarly, to the 5D approach, first, the flux map is corrected and then the virtual reluctances are calculated. The original 6D flux map is derived as in (3.17). Consequently, the flux linkages of each segment are interpolated from the original flux map. The flux linkages differ for all coordinates by the

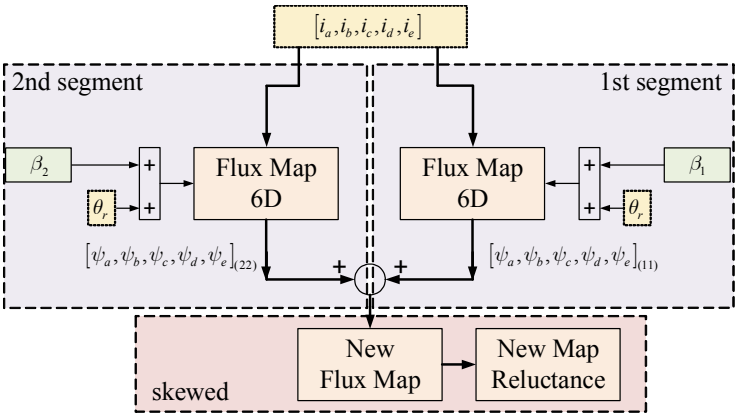

Figure 5.8. Algorithm to calculate 6D skewed virtual reluctance maps

rotor position shift only. This is because the currents do not undergo a transformation and are virtually the same for each skewing segment since electrically the segments are connected in series and see the same current excitation. The algorithm for the VR map skewing correction is depicted in Fig. 5.8. There are current coordinates inputs $[i_a, i_b, i_c, i_d, i_e]$ and rotor angle of each slice correspondingly shifted by $p\beta_{(x)}$ electrical skewing angle of the slice. With these inputs the flux linkages contributed by each skewing slice are interpolated and then summed to obtain the global skewed motor flux linkage. Finally, the VR map is computed as defined in (5.7).

5.3. Models validation

5.3.1. Finite Element Validation

The 5D and 6D flux maps were established by post-processing of the 2D static Finite Element Model of the prototype motor (Fig. 3.9). The model was built in Altair Flux 2019 and the flux map calculation was performed using 8 parallel workers. In the next step, the flux map inversion was obtained through an iterative process, and then the inverted flux map model was completed as described in Chapter 3. In the next step, the virtual reluctances for the 5D and 6D maps were calculated as explained in this chapter. The FEM validation is performed without skew since the FEM model is axially symmetric and the asymmetry imposed by the skewing effect would have to be simulated in 3D FEM requiring enormous calculation time. The inverted map and virtual reluctance map models were constructed in Matlab Simulink 2020a package.

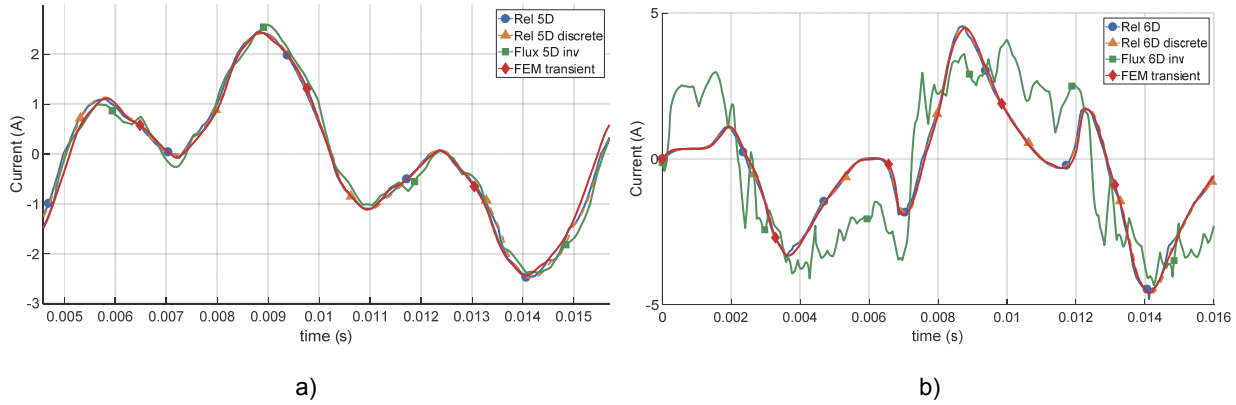

a) b)

Figure 5.9. Comparison of five-phase PMasynRM motor model responses in a) healthy and b) open phase conditions.

Provided the initial conditions for currents and flux linkages are introduced in the model, the algebraic loops get resolved by the Simulink solvers without issues. Apart, the discrete model was added as a standalone C function. The virtual test bench is composed of field-oriented current control (FOC) drive with current and rotor angle measurement and feedback to the control algorithm, ideal power converter imposing ideal voltage commanded by the control algorithm sampled at 10kHz. The same algorithm was run in the coupled Simulink-FEM transient simulation. Thus, the same scenario was reproduced for the inverted flux map, virtual reluctance map, and transient FEM models, and the motor responses were captured and superimposed in Fig. 5.9, where the currents are compared. Already in healthy operation, the 5D model shows some deviation that could be considered as a cliff point because in the 6D the discrepancy is observable and not acceptable for the motor simulation. At the same time, the virtual reluctance models give results very close to transient FEM. This is observed for healthy and open phase conditions.

5.3.2. Experimental Validation

Since the motor prototype possesses two skewed segments in the rotor construction as captured in Fig. 4.1, the experimental validation of the motor models based on the virtual reluctance concept can only be

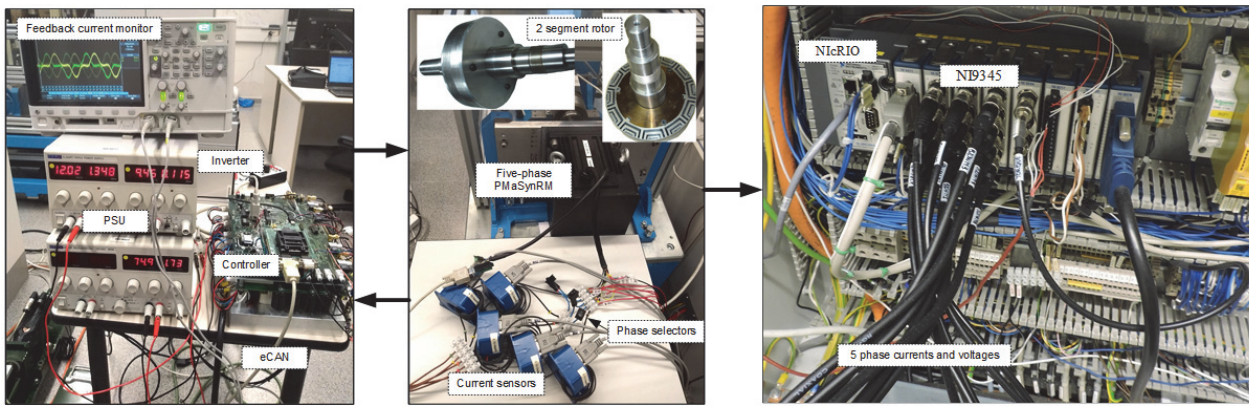

Figure 5.10. Experimental five phase PMaSynRM drive and monitoring system

validated with the skewing component incorporated in the VR maps. This was achieved following the methodology for skewing correction described in this chapter. The experimental setup of the test drive is depicted in Fig. 5.10. It is built with the prototype motor drive bench, load drive based on Siemens SC120 Control with Smart and Single Motor Modules. The voltages and currents are measured for the monitoring system with LEM IT 65-S and CV3-1000 sensors respectively and the signals are captured by the NIcRIO real-time controller through NI9345 analog inputs. Position and velocity are calculated synchronously from the Hengstler RI76TD 9000 lines/rev encoder using embedded LX50 FPGA. Data is saved in binary files for further post-processing. The closed-loop current control is implemented in F28335 DSC from Texas Instruments. The control cycle and switching frequency are set to 10kHz. The measured phase to neutral voltages are filtered and saved to be injected in the virtual reluctance motor model. In such a way, the

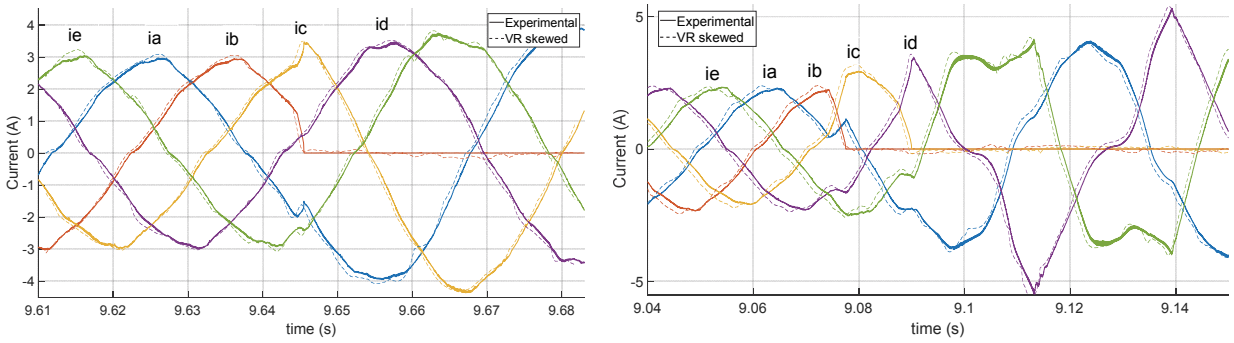

Figure 5.11. Experimental and skewed VR map motor model response a) B-phase open, b) BC-phases open

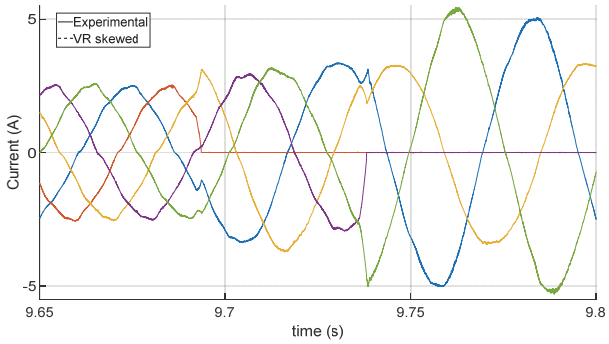

Figure 5.12. Experimental and skewed VR map motor model response a) BD phases open

experimental scenario is one to one reproduced in the simulation environment. Then the measured real currents are compared to those predicted by the skewed VR motor model. In Fig. 5.11 and 5.12 the measured currents, together with predicted by the virtual reluctance 6D skewed motor model, are depicted. In all example scenarios, the predicted currents closely match those observed in the experimental monitoring system. Thus, the skewed VR motor model gives waveforms in close correlation to the real ones proving the validity of the VR concept.

5.4. Conclusions

Novel modeling of five-phase PMaSynRM based on the virtual reluctance concept was introduced in this chapter. The method can be applied to PMSMs of three or more phases, including IPMSM as well. All of the nonlinear phenomena included in the FEM extracted flux maps are captured in the virtual reluctances. Therefore, the cross and phase to phase saturations, field space harmonics, and axial asymmetry imposed by skewing are taken into account in the proposed modeling technique. After flux map identification the virtual reluctances are calculated straight forward and there is no need for cumbersome and not always definite flux map inversion. Finite Element and experimental verification were performed to validate the concept of VR. It has been proved to be effective, accurate, and outperforming models based on multidimensional inversion. The new concept contributes to accurate motor modeling for simulation and implantation in rapid prototyping platforms such as SIL and HIL.

6

6. Sensorless control of saturating PMaSynRM

This chapter describes a sensorless PMaSynRM drive implementation based on the observer method. The Kalman Filter topology is derived for the motor model with constant parameters. The same approach is examined for the cross saturating PMaSynRM. The application is followed by a discussion of the parameter sensitivity.

CONTENTS:

6.1 Observer design with constant PMaSynRM motor parameters

The vector control algorithm with speed and torque control of PMaSynRM was described in Chapter 2.3. The rotor position measurement is required to perform effective current control. This information is usually obtained through sensors mounted on the rotor shaft such as resolvers or incremental encoders. One of the faulty scenarios considered in this study accounts for the position sensor malfunction. In this case, the rotor angle θ_r is no longer available in the feedback loop and thus the drive train is not possible to continue its operation. In other applications, especially where a high safety level is required, the measurement is redundantly performed by hardware and software estimation hybrid solutions. In any case, the sensorless position estimation needs to be implemented. The three-phase motors, especially PMSM machines were thoroughly investigated in terms of their sensorless capabilities. Methods for the rotor position reconstruction include back-EMF techniques, high-frequency signals injection, or observer implementation. The latter could be in the framework of Extended Luenberger Observer (ELO) or Extended Kalman Filter (EKF) for nonlinear systems. As an example, a PI compensated error between the real and virtual reference frame was introduced in [74]. The rotor angle can be also derived from the stator flux linkage estimation [75]. The back-EMF observer is documented in [76], [77]. Some advanced methods based on adaptive input-output feedback linearization were implemented in [78]. These methods were chronologically first developed for the three-phase synchronous machines and then adapted to their five-phase cousins. In both cases, the application in motors with constant parameters was performed. Thus, sensorless control for variable parameters PMaSynRM motor is still a subject of investigation. The Extended Kalman Filter allows correcting for the so-called "system noise" [79], therefore to some extent the non-linearities in the inductances could be filtered out in the observing scheme. In this chapter, first, the Kalman filter structure will be derived and then applied to saturating PMaSynRM. The predicted and corrected estimation of the state vector will be injected into the control algorithm.

The objective of the EKF is to estimate values of the system states which are not measured, by measurement of other states and statistics in the measurement, system, and the state vector. This observer technique requires special care in tuning covariance matrices.

6.1.1. Continuous State Space Model

The model of a three-phase PMaSynRM was given in Chapter 2.2 and its cross-saturating counterpart in Chapter 3.1. Provided constant inductances, the derivatives of the motor currents are linearly related to both axes currents and applied voltages. Moreover, the dynamic state-space model of the motor is derived with the assumption of infinite inertia which is equal to cancel the acceleration part. A state-space model is given in the matrix form as:

$$\begin{cases} \dot{x} = Ax + Bu \\ y = Cx \end{cases} \tag{6.1}$$

where $x = [i_d, i_q, \omega_r, \theta_r]$ is the stator vector, $y = [i_\alpha, i_\beta]$ is the output vector and $u = [U_\alpha, U_\beta]$ the input vector. Furthermore, A is the state matrix, B the input matrix, and C the transformation matrix, and they are defined as:

$$A = \begin{bmatrix} -\frac{R}{L_d} & \omega_r \frac{L_q}{L_d} & -\frac{\psi_{PM}}{L_d} & 0 \\ -\omega_r \frac{L_d}{L_q} & -\frac{R}{L_q} & 0 & 0 \\ 0 & 0 & 0 & 0 \\ 0 & 0 & 1 & 0 \end{bmatrix}, \; B = \begin{bmatrix} \frac{\cos\theta_r}{L_d} & \frac{\sin\theta_r}{L_d} \\ -\frac{\sin\theta_r}{L_q} & \frac{\cos\theta_r}{L_q} \\ 0 & 0 \\ 0 & 0 \end{bmatrix}, \; C = \begin{bmatrix} \cos\theta_r & -\sin\theta_r & 0 & 0 \\ \sin\theta_r & \cos\theta_r & 0 & 0 \end{bmatrix} \tag{6.2}$$

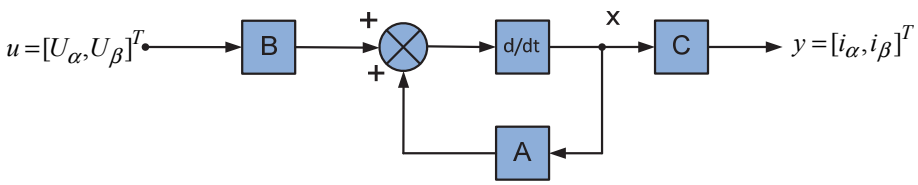

Figure 6.1. Block diagram of the time domain state-space model of PMaSynRM (no cross saturations)

The whole system depicted in Fig. 6.1 is not linear since the output matrix C contains a sub-matrix that transforms stator currents components from the stationary reference frame to the rotor reference frame. Besides, the state matrix A contains the time-variant rotor angular velocity component.

6.1.2. Discrete model

The EKF digital implementation requires discretization of the state space model. The time-discrete state-space model is obtained in the following form:

$$\begin{cases} x(k+1) = A_d x(k) + B_d(k)\,\mathrm{u}(k) \\ y(k) = C_d(k) x(k) \end{cases} \tag{6.3}$$

Where k is the sampling interval ($100\mu s$) and A_d, B_d and C_d are discretized system matrix, input matrix, and transformation matrix respectively and they are defined as:

$$\begin{aligned} A_d &= e^{A(k)} \approx I + A(k)T \\ B_d &= B(k)T \\ C_d &= C(k) \end{aligned} \tag{6.4}$$

Where I denotes the identity matrix and T the sampling time. In form (6.3) the EKF is an ideal deterministic time discrete model. However, the state vector is disturbed by the noise vector v (system

noise vector) and the output vector (measured vector) is disturbed by the noise vector w (measurement noise). They are added to the discretized state-space model to be more realistic (stochastic model):

$$\begin{cases} x(k+1) = A_d x(k) + B_d(k)\,\mathrm{u}(k) + v(k) \\ y(k) = C_d(k) x(k) + w(k) \end{cases} \tag{6.5}$$

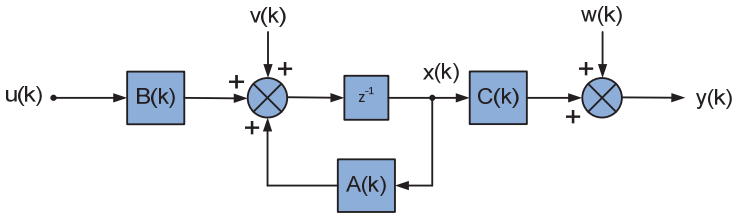

Figure 6.2. Block diagram of the discretized stochastic state-space model of PMaSynRM

The system noise vector v and the measurement noise vector w can be assumed to be zero-mean white Gaussian noises and they have covariance matrices denoted as Q and R respectively. The discrete state, input, and transformation matrices (6.4) result to have the following form:

$$A_d = \begin{bmatrix} 1 - T_s\frac{R}{L_d} & \omega_r \frac{L_q}{L_d} T_s & -\frac{\psi_{PM}}{L_d} T_s & 0 \\ -\omega_r \frac{L_d}{L_q} T_s & 1 - T_s\frac{R}{L_q} & 0 & 0 \\ 0 & 0 & 1 & 0 \\ 0 & 0 & T_s & 1 \end{bmatrix},\ B_d = \begin{bmatrix} T_s\frac{\cos\theta_r}{L_d} & T_s\frac{\sin\theta_r}{L_d} \\ -T_s\frac{\sin\theta_r}{L_q} & T_s\frac{\cos\theta_r}{L_q} \\ 0 & 0 \\ 0 & 0 \end{bmatrix},\ C_d = \begin{bmatrix} \cos\theta_r & -\sin\theta_r & 0 & 0 \\ \sin\theta_r & \cos\theta_r & 0 & 0 \end{bmatrix} \tag{6.6}$$

To complete the mathematical apparatus, the Jacobian matrices are introduced:

$$G(k+1) = I + \left.\frac{\partial\left[A_d(k) + B_d(k)u(k)\right]}{\partial x}\right|_{x=\tilde{x}(k+1)} =$$

$$= \begin{bmatrix} 1 - T_s\frac{R}{L_d} & \tilde{\omega}_r(k+1)\frac{L_q}{L_d} T_s & \frac{L_q \tilde{i}_q(k+1) - \psi_{PM}}{L_d} T_s & \frac{-U_\alpha \sin\tilde{\theta}_r(k+1) + U_\beta \cos\tilde{\theta}_r(k+1)}{L_d} T_s \\ -\tilde{\omega}_r(k+1)\frac{L_d}{L_q} T_s & 1 - T_s\frac{R}{L_q} & -\frac{L_d \tilde{i}_d(k+1)}{L_q} T_s & \frac{-U_\alpha \cos\tilde{\theta}_r(k+1) - U_\beta \sin\tilde{\theta}_r(k+1)}{L_q} T_s \\ 0 & 0 & 1 & 0 \\ 0 & 0 & T_s & 1 \end{bmatrix} \tag{6.7}$$

$$H(k+1) = \left.\frac{\partial\left[C_d(k)\right]}{\partial x}\right|_{x=\tilde{x}(k+1)} = \begin{bmatrix} \cos\tilde{\theta}_r(k+1) & -\sin\tilde{\theta}_r(k+1) & 0 & -\tilde{i}_d(k+1)\sin\tilde{\theta}_r(k+1) \\ \sin\tilde{\theta}_r(k+1) & \cos\tilde{\theta}_r(k+1) & 0 & \tilde{i}_d(k+1)\cos\tilde{\theta}_r(k+1) \end{bmatrix} \tag{6.8}$$

For the sake of simplicity a notation of priori (first) $\tilde{X}$ and posteriori (second) $\hat{X}$ is used, where X denotes every matrix and vector (or variable) used in the algorithm.

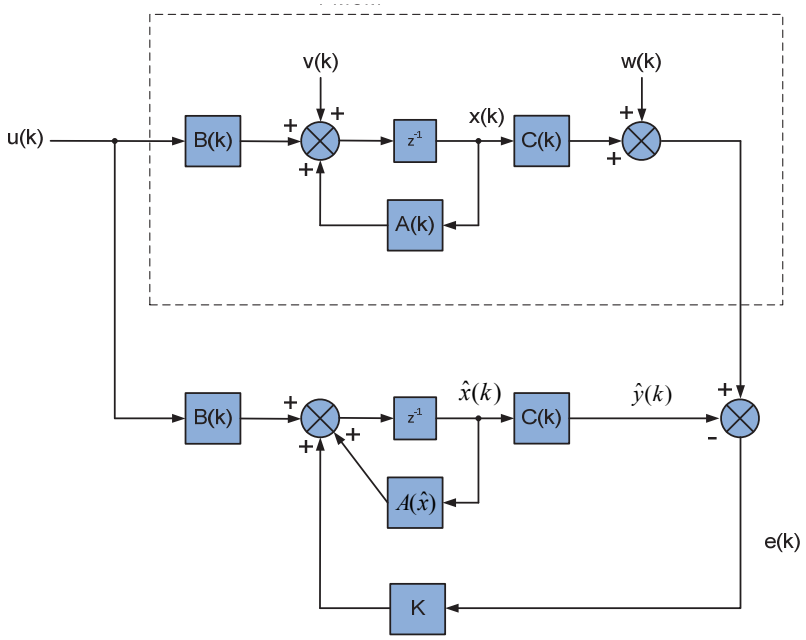

Figure 6.3. Complete structure of the EKF applied to PMaSynRM

The EKF contains two general steps i.e. prediction and correction (also termed as innovation). During the prediction step, the next predicted values of the state vector $\tilde{x}(k+1)$, state covariance matrix $\tilde{P}(k+1)$, and output currents $\tilde{y}(k+1)$ are obtained. In the innovation step, the predicted values are corrected with a product of Kalman gain K , and the error of measured values $y(k+1)-\tilde{y}(k+1)$ is minimized. The corrected values are then fed back to the execution of the next sampling interval. The complete procedure is summarized below:

- Priori state vector estimation (prediction)

$$\tilde{x}(k+1)=A_d(k)\hat{x}(k)+B_d(k)u(k) \tag{6.9}$$

- Output current estimation (prediction)

$$\tilde{y}(k+1)=C_d(k)\tilde{x}(k+1) \tag{6.10}$$

- Priori state error covariance matrix estimation (prediction)

$$\tilde{P}(k+1)=G(k+1)\hat{P}(k)G^T(k+1)+Q \tag{6.11}$$

- Kalman gain computation (innovation)

$$K(k+1)=\tilde{P}(k+1)H^T(k+1)\left[H(k+1)\tilde{P}(k+1)H^T(k+1)+R\right]^{-1} \tag{6.12}$$

- Posteriori state vector estimation (innovation)

$$\hat{x}(k+1)=\tilde{x}(k+1)+K(k+1)\left[y(k+1)-\tilde{y}(k+1)\right] \tag{6.13}$$

- Posteriori state error covariance estimation (innovation)

$$\hat{P}(k+1)=\tilde{P}(k+1)-K(k+1)H(k+1)\tilde{P}(k+1) \tag{6.14}$$

The complete structure of the motor model with disturbance and the EKF algorithm is depicted in Fig. 6.3. It can be seen that actually, the observer implements a replica of the plant (PMaSynRM motor) and controls the error between estimated and measured currents. Once the error is compensated, the estimated currents and other estimated variables in the state vector (position and velocity) can be considered as real values.

6.2. Kalman Filter projection on saturating PMaSynRM

The sensorless control scheme is shown in Figure 6.3. The position sensor is replaced by the estimator block. The input signals come from the sensed currents and reference voltages (so there is no need to measure the rotor position and motor terminal voltages). The covariance matrices P, Q, and R tuning is crucial to achieving filter convergence and stability of tracking. The initial approach assumes a constant diagonal unitary matrix [80], often a trial and error approach is recommended to search for the stable values [81]. The model described by (6.5)-(6.8) is valid for the PMaSynRM motor with constant inductances.

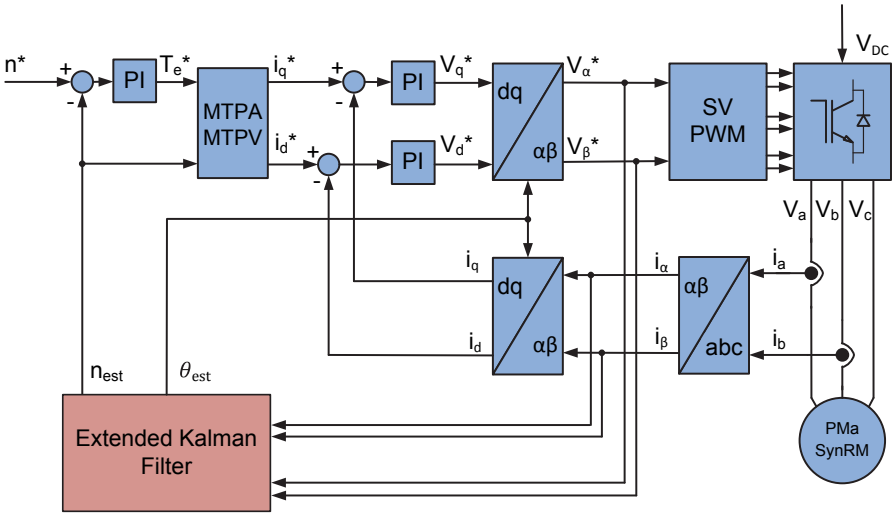

Figure 6.4. PMaSynRM sensorless FOC scheme based on EKF

However, the intrinsic characteristic of the EKF observer is to cope with disturbances also in the state matrix, thus saturation is considered as a disturbance that could be filtered out. In this sense, the EKF filter is implemented and evaluated in cross-saturating PMaSynRM with a non-linear flux map identified in Chapter 3 i.e. the motor model is cross-saturating but the Kalman Filter matrices *A, B, C, G,* and *H* are fed with initial constant inductances only. Several scenarios have been performed. From Fig. 6.5, where EKF was applied on a three-phase real prototype motor, it can be observed that the initial convergence is more

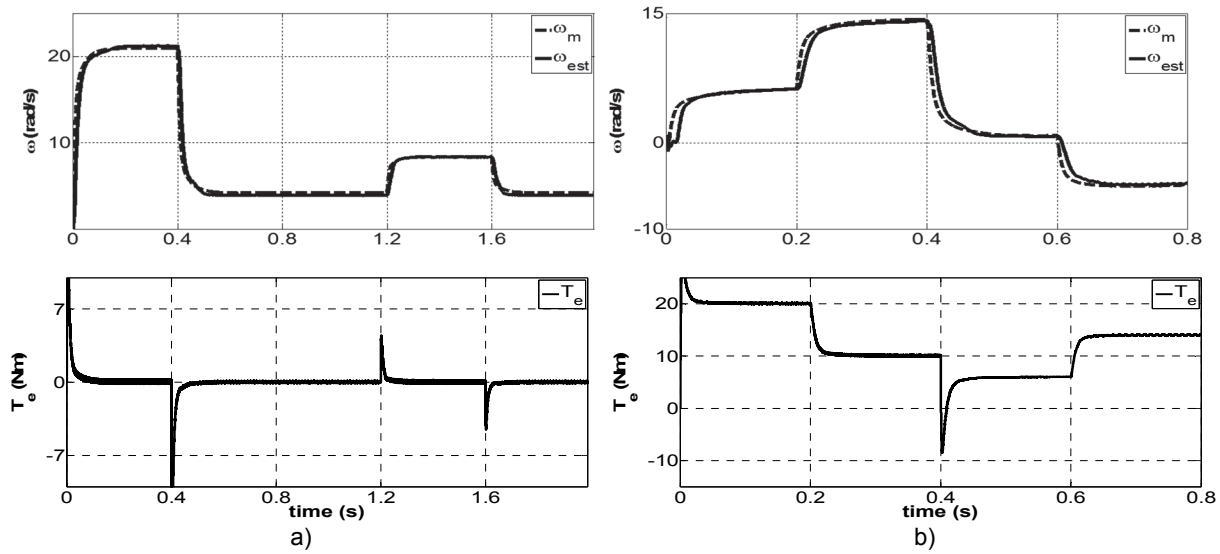

Figure 6.5. Sensorless control of three-phase PMaSynRM, estimated and measured speed and estimated torque a) no-load condition, b) variable load

difficult when the motor is loaded during the startup condition. Nevertheless, the measured speed is well estimated by the EKF algorithm. Stable speed tracking is achieved and maintained within the load profile imposed on the machine shaft. Thus, it can be concluded that the initial convergence is critical for the observer's performance.

Next, the EKF observer was applied to an unsaturated (0D) five-phase PMaSynRM which currents of the third harmonic plane were compensated and the torque controlled through the first harmonic only. In

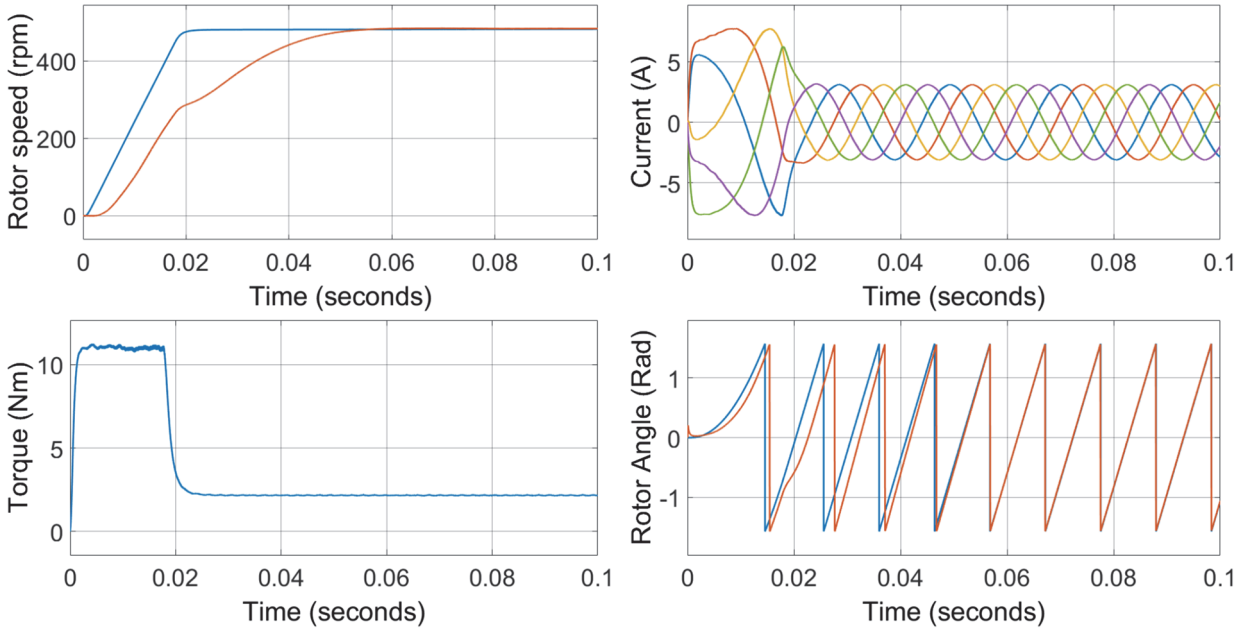

Figure 6.6. EKF velocity and rotor angle tracking of un-saturated five-phase PMaSynRM with torque and current response

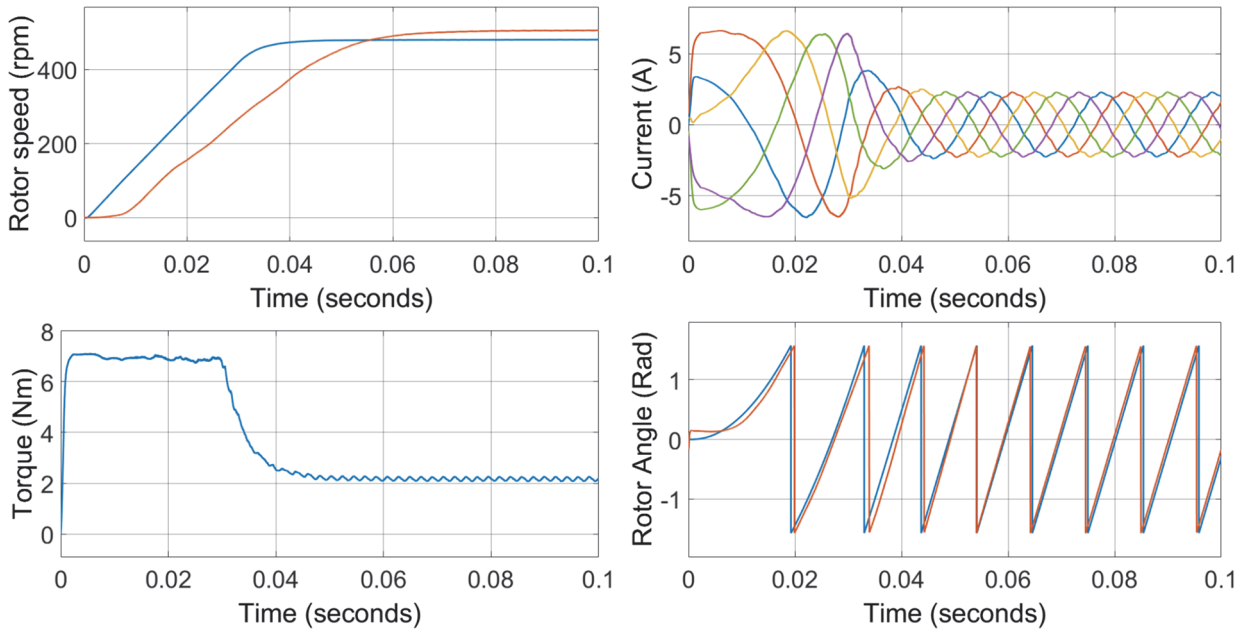

Figure 6.7. EKF velocity and rotor angle tracking of 4D saturated five-phase PMaSynRM with torque and current response

Fig. 6.6 the performance during a loaded motor startup is depicted. The estimated rotor position initially carries a phase lag which is corrected after four electrical cycles. The convergence of the angle and speed may be accelerated by the adjustment of the system covariance matrix. The same scenario was evaluated with saturating PMaSynRM model (4D) and the corresponding results are shown in Fig. 6.7. It should be noted that in this case, the EKF needs to correct for the saturating inductances uncertainties in the system matrix. Initial convergence is achieved after 4 electric cycles as well, but consequent tracking is noticeable with higher error and the speed is overestimated in the steady-state regime. Potentially to improve this response the covariance matrices could be incremented or the system matrix could take into account the nonlinear inductances, which is foreseen in future work. It can be concluded that saturating PMaSynRM models developed in this thesis could be used in sensorless systems EKF-based with adjustments in the system matrix, to reconstruct the unmeasured mechanical magnitudes.

6.3. Conclusions

In this chapter, an implementation of the observer method for the rotor position and speed reconstruction was analyzed and projected at cross-saturating PMaSynRM. The results show that the EKF structure copes well and corrects disturbances in the state vector provoked by saturating motor nature.

7

7. Overall conclusions and future work

In this section, the general conclusions drawn from the thesis are presented concerning defined research problems, hypotheses, and objectives. In addition, the future work initiated by this research is proposed.

CONTENTS:

7.1. Thesis conclusions

At the end of the conduct of this research project, regarding the proposed methods and techniques supported by the experimental results, the global conclusions are drawn:

- The state-of-the-art regarding PMSM and PMaSynRM drive control was revised for three and five-phase motors. The conventional modeling is based on the assumptions of linear magnetic behavior and suffices provided motor works only in the unsaturated zone. The approaches to control the 1st and 3rd harmonics are widely described in the literature and recapitulated in this thesis.

- The inclusion of cross saturation effects in rotating field and mutual saturation in natural stator phase quantities was derived upon the basis of FEA extracted flux maps, posteriori inverted for implementation in the time-stepping simulation. This technique was successfully implemented in the motor drive enabling high accuracy virtual bench replica of the experimental setup.

- In the next stage, space harmonics were included by adding one dimension of the flux function with respect to rotor angle. It has been shown that motor healthy and open phase faulty behavior is accurately predicted by the elaborated models in generator and motor mode.

- Additional complexity in the magnetic flux distribution introduced by skewing was tackled by correction of the single slice flux map with contribution from each skewing segment. Thus, the model was proved to handle this phenomenon as well.

- A novel method for PMaSynRM and PMSM motor modeling based on the virtual reluctance (VR) concept was proposed, implemented, applied, and verified by FEA and experimental results. The main advantage of this new technique is the avoidance of the flux map inversion calculation, which is encumbered by large errors when performed on multi-dimension problems. The VR maps are always definite and free of these accumulated residual errors, and they offer extremely fast pre-calculation time.

- The derived models are applicable for the fault-tolerant and sensorless approaches, especially where high motor model accuracy is of great concern, that is for motors intrinsically saturating such as PMaSynRM of three or more phases.

7.3. Future work

High fidelity models of three and five-phase cross saturating PMaSynRM have been developed with field space harmonics and axial asymmetry provoked by skewing. The research lines parting from the conclusions of this thesis groundwork can be formulated as follows:

- Further improve and optimize the control trajectories based on the flux maps. Especially, higher efficiency may be achieved upon the inclusion of the iron losses in the soft magnetic parts of the stator and rotor construction. The higher efficiency aspect is very promising in terms of battery range e.g. in the automotive and battery-powered industrial sectors.

- Analyze and enhance drives with fault-tolerant capabilities considering nonlinearities discussed in this research work.

- Implement derived models in fast prototyping platforms comprising SIL or/and HIL setup in sense of virtual prototyping before timely and costly hardware implementation.

- Upgrade algorithms for rotor position and speed estimation based on motor models such as observers. Include, saturation effects in the sensorless scheme.

- Apply the proposed models to the new types of PMaSynRM which adopt different shapes of magnets and new typologies resulting in completely filled flux barriers with a mix of magnetic material and a polymer binder.

8

8. Thesis results dissemination

This chapter shows the list of papers of international journals and conferences that were published in the scope of this thesis. Next, additional publications arisen from collaboration related to the thesis study are registered. Further, this thesis work resulted in principal research in public research projects and lead engineering in private development projects, that are listed consequently. Finally, the short info about R&D scientific and industrial conducts accomplished during thesis development is summarized.

CONTENTS:

8.1 Publications from this thesis work

8.1.1 Journal papers

T. D. Michalski, J. L. Romeral, G. Mino-Aguilar, “Magnetic Skew Interface in Five-Phase Ferrite Assisted Synchronous Reluctance Motor Model”, in *Elsevier Journal of Magnetism and Magnetic Materials*, **Under review**

T. D. Michalski, J. L. Romeral, G. Mino-Aguilar, “Open-Phase Faulty Five-Phase Permanent Magnet Assisted Synchronous Reluctance Motor Model with Axial Skew”, in *IEEE Transactions on Magnetics*, **In revision**

T. D. Michalski, J. L. Romeral, G. Mino-Aguilar, “Virtual Reluctance Concept to model Healthy and Open Phase PMaSynRM”, in *IEEE Transactions on Industrial Electronics*, **In revision**

8.1.2 Conference papers

T. Michalski, F. Acosta-Cambranis, L. Romeral, J. Zaragoza and G. Mino-Aguilar, “Vector Control of Crosswise Saturating Five-Phase PMaSynRM in Wide Speed Range,” *IECON 2020 - 46th Annual Conference of the IEEE Industrial Electronics Society*, Singapore, 2020

T. Michalski, F. Acosta-Cambranis, L. Romeral and J. Zaragoza, "Multiphase PMSM and PMaSynRM Flux Map Model with Space Harmonics and Multiple Plane Cross Harmonic Saturation," *IECON 2019 - 45th Annual Conference of the IEEE Industrial Electronics Society*, Lisbon, Portugal, 2019, pp. 1210-1215, doi: 10.1109/IECON.2019.8927421.

T. Michalski, C. Lopez, A. Garcia and L. Romeral, "Sensorless control of five phase PMSM based on extended Kalman filter," *IECON 2016 - 42nd Annual Conference of the IEEE Industrial Electronics Society*, Florence, 2016, pp. 2904-2909, doi: 10.1109/IECON.2016.7793740.

T. Michalski, C. Lopez, A. Garcia and L. Romeral, "Dynamic nonlinear reluctance network analysis of five phase outer rotor BLDC machine," *IECON 2016 - 42nd Annual Conference of the IEEE Industrial Electronics Society*, Florence, 2016, pp. 1790-1795, doi: 10.1109/IECON.2016.7793256.

8.2. Publications from collaboration related to the thesis work

8.2.1 Conference papers

F. Acosta-Cambranis, J. Zaragoza, L. Romeral, **T. Michalski** and V. Pou-Muñoz, "A Versatile Workbench Simulator: Five-phase Inverter and PMa-SynRM performance evaluation," *IECON 2019 - 45th Annual Conference of the IEEE Industrial Electronics Society*, Lisbon, Portugal, 2019, pp. 886-891, doi: 10.1109/IECON.2019.8927088.

C. López Torres, **T. Michalski**, A. Garcia Espinosa and L. Romeral, "Fast optimization of the magnetic model by means of reluctance network for PMa-SynRM," *IECON 2016 - 42nd Annual Conference of the IEEE Industrial Electronics Society*, Florence, 2016, pp. 1642-1647, doi: 10.1109/IECON.2016.7793291.

C. López, **T. Michalski**, A. Espinosa and L. Romeral, "New SynRM design approach based on behaviour maps analysis," *2016 XXII International Conference on Electrical Machines (ICEM)*, Lausanne, 2016, pp. 1915-1921, doi: 10.1109/ICELMACH.2016.7732785.

C. López, **T. Michalski**, A. Espinosa and L. Romeral, "Rotor of synchronous reluctance motor optimization by means reluctance network and genetic algorithm," *2016 XXII International Conference on Electrical Machines (ICEM)*, Lausanne, 2016, pp. 2052-2058, doi: 10.1109/ICELMACH.2016.7732805.

8.3. Collaboration in public and private projects related with this research

8.3.1 Public research projects

"Fault Tolerant Powertrain based on multiphase PMa_SynRM driven by a SiC inverter for a reliable Electric Vehicle operation", (J-02278), MIN DE ECONOMIA Y COMPETITIVIDAD, TRA2016-80472-R, 2016.12.30 – 2019.12.29

"High Efficiency Powertrain for Electric Vehicle based on the latest technologies of synchronous motors and silicon carbide power converters", (J-01872), MIN DE ECONOMIA Y COMPETITIVIDAD, TRA2013-46757-R, 2014.01.01 – 2017.06.30

8.3.2 Private research projects

"Diseño de Motor de reluctancia PMAS_synRM para propulsión PHEV", (C-10953), SEAT - Centro Técnico, 2017.11.01 – 2018.02.28

"Electromagnetic design and control of PMa-SynRM for PHEV propulsion", Volkswagen AG, SEAT - Centro Técnico, 2015.11.01 – 2016.12.31

"Diseño de motor PMaSYNRM para vehículo Eléctrico", (C-10280), SEAT - Centro Técnico, 2014.11.21 – 2016.12.20

8.4. R&D stays during development of this thesis

"Research, Investigation and modeling of multi-phase Permanent Magnet Assisted Synchronous Reluctance Motors", in *Facultad en Ciencias de la Electrónica, Benemérita Universidad Autónoma de Puebla*, Puebla, Mexico, 2019.12.10-2020.01.15

"Research, Investigation and modeling of 3-phase Permanent Magnet Assisted Synchronous Reluctance Motor for Traction Applications", in *Facultad en Ciencias de la Electrónica, Benemérita Universidad Autónoma de Puebla, Puebla, Mexico*, 2017.06.26-2017.08.25

References

[1] Krishnan, R. (2010), “Permanent Magnet Synchronous and Brushless DC Motor Drives” in *Boca Raton: CRC Press*, doi: 10.1201/9781420014235.

[2] P.Vas, “Sensorless vector and direct torque control” in *Oxford University Press*, 1998

[3] P. Pillay and R. Krishnan, "Modeling, simulation, and analysis of permanent-magnet motor drives. I. The permanent-magnet synchronous motor drive," in *IEEE Transactions on Industry Applications*, vol. 25, no. 2, pp. 265-273, March-April 1989, doi: 10.1109/28.25541.

[4] G. Capolino and A. Cavagnino, "New trends in electrical machines technology - Part I," in *IEEE Transactions on Industrial Electronics*, vol. 61, no. 8, pp. 4281-4285, Aug. 2014, doi: 10.1109/TIE.2013.2295770.

[5] G. Pellegrino, A. Vagati, P. Guglielmi and B. Boazzo, "Performance Comparison Between Surface-Mounted and Interior PM Motor Drives for Electric Vehicle Application," in *IEEE Transactions on Industrial Electronics*, vol. 59, no. 2, pp. 803-811, Feb. 2012, doi: 10.1109/TIE.2011.2151825.

[6] P. Ramesh and N. C. Lenin, "High Power Density Electrical Machines for Electric Vehicles—Comprehensive Review Based on Material Technology," in *IEEE Transactions on Magnetics*, vol. 55, no. 11, pp. 1-21, Nov. 2019, Art no. 0900121, doi: 10.1109/TMAG.2019.2929145.

[7] A. Wang, Y. Jia and W. L. Soong, "Comparison of Five Topologies for an Interior Permanent-Magnet Machine for a Hybrid Electric Vehicle," in *IEEE Transactions on Magnetics*, vol. 47, no. 10, pp. 3606-3609, Oct. 2011, doi: 10.1109/TMAG.2011.2157097.

[8] L. Parsa and H. A. Toliyat, "Five-phase permanent-magnet motor drives," in *IEEE Transactions on Industry Applications*, vol. 41, no. 1, pp. 30-37, Jan.-Feb. 2005, doi: 10.1109/TIA.2004.841021.

[9] Z. Liu, Z. Zheng and Y. Li, "Enhancing Fault-Tolerant Ability of a Nine-Phase Induction Motor Drive System Using Fuzzy Logic Current Controllers," in *IEEE Transactions on Energy Conversion*, vol. 32, no. 2, pp. 759-769, June 2017, doi: 10.1109/TEC.2017.2692528.

[10] H. Tahanian, M. Aliahmadi and J. Faiz, "Ferrite Permanent Magnets in Electrical Machines: Opportunities and Challenges of a Non-Rare-Earth Alternative," in *IEEE Transactions on Magnetics*, vol. 56, no. 3, pp. 1-20, March 2020, Art no. 900120, doi: 10.1109/TMAG.2019.2957468.

[11] E. E. Ward and H. Härer, "Preliminary investigation of an invertor-fed 5-phase induction motor," in *Proceedings of the Institution of Electrical Engineers*, vol. 116, no. 6, pp. 980-984, June 1969, doi: 10.1049/piee.1969.0182.

[12] M. Onsal, Y. Demir and M. Aydin, "A New Nine-Phase Permanent Magnet Synchronous Motor With Consequent Pole Rotor for High-Power Traction Applications," in *IEEE Transactions on Magnetics*, vol. 53, no. 11, pp. 1-6, Nov. 2017, Art no. 8700606, doi: 10.1109/TMAG.2017.2709788.

[13] A. K. M. Arafat and S. Choi, "Optimal Phase Advance Under Fault-Tolerant Control of a Five-Phase Permanent Magnet Assisted Synchronous Reluctance Motor," in *IEEE Transactions on Industrial Electronics*, vol. 65, no. 4, pp. 2915-2924, April 2018, doi: 10.1109/TIE.2017.2750620.

[14] Z. Liu, Y. Li and Z. Zheng, "A review of drive techniques for multiphase machines," in *CES Transactions on Electrical Machines and Systems*, vol. 2, no. 2, pp. 243-251, June 2018, doi: 10.30941/CESTEMS.2018.00030.

[15] E. Levi, "Multiphase Electric Machines for Variable-Speed Applications," in *IEEE Transactions on Industrial Electronics*, vol. 55, no. 5, pp. 1893-1909, May 2008, doi: 10.1109/TIE.2008.918488.

[16] C. López-Torres, A. Garcia Espinosa, J. Riba and L. Romeral, "Design and Optimization for Vehicle Driving Cycle of Rare-Earth-Free SynRM Based on Coupled Lumped Thermal and Magnetic Networks," in *IEEE Transactions on Vehicular Technology*, vol. 67, no. 1, pp. 196-205, Jan. 2018, doi: 10.1109/TVT.2017.2739020.

[17] M. Kimiabeigi *et al*., "High-Performance Low-Cost Electric Motor for Electric Vehicles Using Ferrite Magnets," in *IEEE Transactions on Industrial Electronics*, vol. 63, no. 1, pp. 113-122, Jan. 2016, doi: 10.1109/TIE.2015.2472517.

[18] N. Bianchi, H. Mahmoud and S. Bolognani, "Fast synthesis of permanent magnet assisted synchronous reluctance motors," in *IET Electric Power Applications*, vol. 10, no. 5, pp. 312-318, 5 2016, doi: 10.1049/iet-epa.2015.0240.

[19] P. Guglielmi, B. Boazzo, E. Armando, G. Pellegrino and A. Vagati, "Permanent-Magnet Minimization in PM-Assisted Synchronous Reluctance Motors for Wide Speed Range," in *IEEE Transactions on Industry Applications*, vol. 49, no. 1, pp. 31-41, Jan.-Feb. 2013, doi: 10.1109/TIA.2012.2229372.

[20] G. Pellegrino, Th. M. Jahns, N. Bianchi, W. Soong, F. Cupertino, "The Rediscovery of Synchronous Reluctance and Ferrite Permanent Magnet Motors," in *SpringerBriefs in Electrical and Computer Engineering*, Springer 2016, ISBN 978-3-319-32202-5, doi: 10.1007/978-3-319-32202-5.

[21] S. D. Sudhoff, B. T. Kuhn, K. A. Corzine and B. T. Branecky, "Magnetic Equivalent Circuit Modeling of Induction Motors," in *IEEE Transactions on Energy Conversion*, vol. 22, no. 2, pp. 259-270, June 2007, doi: 10.1109/TEC.2006.875471.

[22] N. Bracikowski, M. Hecquet, P. Brochet and S. V. Shirinskii, "Multiphysics Modeling of a Permanent Magnet Synchronous Machine by Using Lumped Models," in *IEEE Transactions on Industrial Electronics*, vol. 59, no. 6, pp. 2426-2437, June 2012, doi: 10.1109/TIE.2011.2169640.

[23] M. Amrhein and P. T. Krein, "3-D Magnetic Equivalent Circuit Framework for Modeling Electromechanical Devices," in *IEEE Transactions on Energy Conversion*, vol. 24, no. 2, pp. 397-405, June 2009, doi: 10.1109/TEC.2009.2016134.

[24] T. Michalski, C. Lopez, A. Garcia and L. Romeral, "Dynamic nonlinear reluctance network analysis of five phase outer rotor BLDC machine," *IECON 2016 - 42nd Annual Conference of the IEEE Industrial Electronics Society*, Florence, 2016, pp. 1790-1795, doi: 10.1109/IECON.2016.7793256.

[25] Gyu-Hong Kang, Jung-Pyo Hong, Gyu-Tak Kim and Jung-Woo Park, "Improved parameter modeling of interior permanent magnet synchronous motor based on finite element analysis," in *IEEE Transactions on Magnetics*, vol. 36, no. 4, pp. 1867-1870, July 2000, doi: 10.1109/20.877809.

[26] B. Stumberger, G. Stumberger, D. Dolinar, A. Hamler and M. Trlep, "Evaluation of saturation and cross-magnetization effects in interior permanent-magnet synchronous motor," in *IEEE Transactions on Industry Applications*, vol. 39, no. 5, pp. 1264-1271, Sept.-Oct. 2003, doi: 10.1109/TIA.2003.816538.

[27] K. M. Rahman and S. Hiti, "Identification of machine parameters of a synchronous motor," in *IEEE Transactions on Industry Applications*, vol. 41, no. 2, pp. 557-565, March-April 2005, doi: 10.1109/TIA.2005.844379.

[28] M. Hadžiselimović, G. Štumberger, B. Štumberger, and I. Zagradišnik, "Magnetically nonlinear dynamic model of synchronous motor with permanent magnets," in Journal of Magnetism and Magnetic Materials, vol. 316, no. 2, pp. e257-e260, 200

[29] X. Chen, J. Wang, B. Sen, P. Lazari and T. Sun, "A High-Fidelity and Computationally Efficient Model for Interior Permanent-Magnet Machines Considering the Magnetic Saturation, Spatial Harmonics, and Iron Loss Effect," in *IEEE Transactions on Industrial Electronics*, vol. 62, no. 7, pp. 4044-4055, July 2015, doi: 10.1109/TIE.2014.2388200.

[30] M. Boesing, M. Niessen, T. Lange and R. De Doncker, "Modeling spatial harmonics and switching frequencies in PM synchronous machines and their electromagnetic forces," *2012 XXth International Conference on Electrical Machines*, Marseille, 2012, pp. 3001-3007, doi: 10.1109/ICElMach.2012.6350315.

[31] L. Quéval and H. Ohsaki, "Nonlinear abc-Model for Electrical Machines Using N-D Lookup Tables," in *IEEE Transactions on Energy Conversion*, vol. 30, no. 1, pp. 316-322, March 2015, doi: 10.1109/TEC.2014.2358854.

[32] Hyung-Min Ryu, Jang-Hwan Kim and Seung-Ki Sul, "Analysis of multiphase space vector pulse-width modulation based on multiple d-q spaces concept," in *IEEE Transactions on Power Electronics*, vol. 20, no. 6, pp. 1364-1371, Nov. 2005, doi: 10.1109/TPEL.2005.857551.

[33] E. Levi, "Multiphase Electric Machines for Variable-Speed Applications," in *IEEE Transactions on Industrial Electronics*, vol. 55, no. 5, pp. 1893-1909, May 2008, doi: 10.1109/TIE.2008.918488.

[34] Y. Hu, Z. Zhu and K. Liu, "Current Control for Dual Three-Phase Permanent Magnet Synchronous Motors Accounting for Current Unbalance and Harmonics," in *IEEE Journal of Emerging and Selected Topics in Power Electronics*, vol. 2, no. 2, pp. 272-284, June 2014, doi: 10.1109/JESTPE.2014.2299240.

[35] T. Kamel, D. Abdelkader, and B. Said, "Vector control of five-phasepermanent magnet synchronous motor drive," in *2015 4th International Conference on Electrical Engineering (ICEE)*, 13-15 Dec. 2015 2015, pp.1-4.

[36] C. Gupta, S. Marwaha, and M. S. Manna, “Finite element method as an aid to machine design: A computational tool,” in *Proc. COMSOL Conf.*, 2009, pp. 1-6.

[37] S. W. Nam and M. N. Uddin, "Model-Based Loss Minimization Control of an Induction Motor Drive," *2006 IEEE International Symposium on Industrial Electronics*, Montreal, Que., 2006, pp. 2367-2372, doi: 10.1109/ISIE.2006.295942.

[38] C. Shumei, D. Ying and S. Liwei, "Rotor Slots Design of Induction Machine for Hybrid Electric Vehicle Drives," *2006 IEEE Vehicle Power and Propulsion Conference*, Windsor, 2006, pp. 1-3, doi: 10.1109/VPPC.2006.364375.

[39] B. K. Bose, "Chapter 1 - Introduction and Perspective," in Power Electronics And Motor DrivesBurlington: Academic Press, 2006, pp. 1-24.

[40] C. C. Chan, "An overview of electric vehicle technology," in *Proceedings of the IEEE*, vol. 81, no. 9, pp. 1202-1213, Sept. 1993, doi: 10.1109/5.237530.

[41] O. D. Momoh and M. O. Omoigui, "An overview of hybrid electric vehicle technology," in *2009 IEEE Vehicle Power and Propulsion Conference*, 2009, pp. 1286-1292.

[42] H. Cai, B. Guan and L. Xu, "Low-Cost Ferrite PM-Assisted Synchronous Reluctance Machine for Electric Vehicles," in *IEEE Transactions on Industrial Electronics*, vol. 61, no. 10, pp. 5741-5748, Oct. 2014, doi: 10.1109/TIE.2014.2304702.

[43] S. Taghavi and P. Pillay, "A mechanically robust rotor with transverse-laminations for a synchronous reluctance machine for traction applications," *2014 IEEE Energy Conversion Congress and Exposition (ECCE)*, Pittsburgh, PA, 2014, pp. 5131-5137, doi: 10.1109/ECCE.2014.6954105.

[44] A. Yamada and I. Miki, "New permanent magnet synchronous motor with reduced rare earth magnets," *2014 17th International Conference on Electrical Machines and Systems (ICEMS)*, Hangzhou, 2014, pp. 391-396, doi: 10.1109/ICEMS.2014.7013502.

[45] W. Kakihara, M. Takemoto and S. Ogasawara, "Rotor structure in 50 kW spoke-type interior permanent magnet synchronous motor with ferrite permanent magnets for automotive applications," *2013 IEEE Energy Conversion Congress and Exposition*, Denver, CO, 2013, pp. 606-613, doi: 10.1109/ECCE.2013.6646757.

[46] S. Ooi, S. Morimoto, M. Sanada and Y. Inoue, "Performance evaluation of a high power density PMASynRM with ferrite magnets," *2011 IEEE Energy Conversion Congress and Exposition*, Phoenix, AZ, 2011, pp. 4195-4200, doi: 10.1109/ECCE.2011.6064341.

[47] P. Niazi, H. A. Toliyat, D. Cheong and J. Kim, "A Low-Cost and Efficient Permanent-Magnet-Assisted Synchronous Reluctance Motor Drive," in *IEEE Transactions on Industry Applications*, vol. 43, no. 2, pp. 542-550, March-april 2007, doi: 10.1109/TIA.2006.890033.

[48] J. H. Lee, Tae Won Yun and Ah Ram Jeon, "Characteristic analysis & optimum design of Permanent Magnet Assisted Synchronous Reluctance Motor for premium efficiency performance," *Digests of the 2010 14th Biennial IEEE Conference on Electromagnetic Field Computation*, Chicago, IL, 2010, pp. 1-1, doi: 10.1109/CEFC.2010.5480556.

[49] M. Paradkar and J. Boecker, "Design of a high performance ferrite magnet-assisted synchronous reluctance motor for an electric vehicle," *IECON 2012 - 38th Annual Conference on IEEE Industrial Electronics Society*, Montreal, QC, 2012, pp. 4099-4103, doi: 10.1109/IECON.2012.6389234.

[50] E. Schmidt, "Synchronous reluctance machines with high-anisotropy rotors — Comparison of their operational characteristics," *2014 Australasian Universities Power Engineering Conference (AUPEC)*, Perth, WA, 2014, pp. 1-6, doi: 10.1109/AUPEC.2014.6966496.

[51] M. Obata, S. Morimoto, M. Sanada and Y. Inoue, "Performance of PMASynRM With Ferrite Magnets for EV/HEV Applications Considering Productivity," in *IEEE Transactions on Industry Applications*, vol. 50, no. 4, pp. 2427-2435, July-Aug. 2014, doi: 10.1109/TIA.2013.2294999.

[52] M. Obata, M. Shigeo, M. Sanada and Y. Inoue, "High-performance PMASynRM with ferrite magnet for EV/HEV applications," *2013 15th European Conference on Power Electronics and Applications (EPE)*, Lille, 2013, pp. 1-9, doi: 10.1109/EPE.2013.6631814.

[53] E. K. Beser, S. Camur, B. Arifoglu, and E. Beser, “Comparison of Two Rotor Configurations by Changing the Amount of Magnet and Reluctance Components,” *Journal of Electrical Engineering and Technology*, vol. 10, no. 1, pp. 155–164, Jan. 2015, doi: 10.5370/jeet.2015.10.1.155.

[54] J. W. Kelly, E. G. Strangas and J. M. Miller, "Multi-phase inverter analysis," *IEMDC 2001. IEEE International Electric Machines and Drives Conference (Cat. No.01EX485)*, Cambridge, MA, USA, 2001, pp. 147-155, doi: 10.1109/IEMDC.2001.939290.

[55] M. J. Duran and E. Levi, "Multi-Dimensional Approach to Multi-Phase Space Vector Pulse Width Modulation," *IECON 2006 - 32nd Annual Conference on IEEE Industrial Electronics*, Paris, 2006, pp. 2103-2108, doi: 10.1109/IECON.2006.347436.

[56] A. Lega, M. Mengoni, G. Serra, A. Tani and L. Zarri, "General theory of space vector modulation for five-phase inverters," *2008 IEEE International Symposium on Industrial Electronics*, Cambridge, 2008, pp. 237-244, doi: 10.1109/ISIE.2008.4677169.

[57] E. S. Obe, "Direct computation of ac machine inductances based on winding function theory," in *Energy Conversion and Management, Elsevier,* Volume 50, Issue 3, March 2009, Pages 539-542

[58] R. Dutta, M. F. Rahman and L. Chong, "Winding Inductances of an Interior Permanent Magnet (IPM) Machine With Fractional Slot Concentrated Winding," in *IEEE Transactions on Magnetics*, vol. 48, no. 12, pp. 4842-4849, Dec. 2012, doi: 10.1109/TMAG.2012.2203140.

[59] T. Lubin, T. Hamiti, H. Razik and A. Rezzoug, "Comparison Between Finite-Element Analysis and Winding Function Theory for Inductances and Torque Calculation of a Synchronous Reluctance Machine," in *IEEE Transactions on Magnetics*, vol. 43, no. 8, pp. 3406-3410, Aug. 2007, doi: 10.1109/TMAG.2007.900404.

[60] V. Bobek, "PMSM Electrical Parameters Measurement", *Freescale Semiconductor Application Note*, Document Number:AN4680, Rev. 0, 02/2013

[61] A. Cavagnino, S. Vaschetto and E. Agamloh, "Practical considerations on the off-line measurements of PMSM and SyRM inductances," *2017 IEEE Energy Conversion Congress and Exposition (ECCE)*, Cincinnati, OH, 2017, pp. 1175-1182, doi: 10.1109/ECCE.2017.8095922.

[62] C. López-Torres, C. Colls, A. Garcia, J. Riba and L. Romeral, "Development of a Behavior Maps Tool to Evaluate Drive Operational Boundaries and Optimization Assessment of PMa-SynRMs," in *IEEE Transactions on Vehicular Technology*, vol. 67, no. 8, pp. 6861-6871, Aug. 2018, doi: 10.1109/TVT.2018.2823339.

[63] Y. Dai, L. Song and S. Cui, "Development of PMSM Drives for Hybrid Electric Car Applications," in *IEEE Transactions on Magnetics*, vol. 43, no. 1, pp. 434-437, Jan. 2007, doi: 10.1109/TMAG.2006.887718.

[64] L. Parsa and L. Hao, "Interior Permanent Magnet Motors With Reduced Torque Pulsation," in *IEEE Transactions on Industrial Electronics*, vol. 55, no. 2, pp. 602-609, Feb. 2008, doi: 10.1109/TIE.2007.911953.

[65] In-Soung Jung, Jin Hur and Dong-Seok Hyun, "3-D analysis of permanent magnet linear synchronous motor with magnet arrangement using equivalent magnetic circuit network method," in *IEEE Transactions on Magnetics*, vol. 35, no. 5, pp. 3736-3738, Sept. 1999, doi: 10.1109/20.800648.

[66] J. Urresty, J. Riba, L. Romeral and A. Garcia, "A Simple 2-D Finite-Element Geometry for Analyzing Surface-Mounted Synchronous Machines With Skewed Rotor Magnets," in *IEEE Transactions on Magnetics*, vol. 46, no. 11, pp. 3948-3954, Nov. 2010, doi: 10.1109/TMAG.2010.2062529.

[67] E. Schmidt and A. Eilenberger, "Calculation of Position-Dependent Inductances of a Permanent Magnet Synchronous Machine With an External Rotor by Using Voltage-Driven Finite Element

Analyses," in *IEEE Transactions on Magnetics*, vol. 45, no. 3, pp. 1788-1791, March 2009, doi: 10.1109/TMAG.2009.2012822.

[68] F. Piriou and A. Razek, "A model for coupled magnetic-electric circuits in electric machines with skewed slots," in *IEEE Transactions on Magnetics*, vol. 26, no. 2, pp. 1096-1100, March 1990, doi: 10.1109/20.106510.

[69] R. Carlson, C. A. da Silva, N. Sadowski, Y. Lefevre and M. Lajoie-Mazenc, "The effect of the stator-slot opening on the interbar currents of skewed cage induction motor," in *IEEE Transactions on Magnetics*, vol. 38, no. 2, pp. 1285-1288, March 2002, doi: 10.1109/20.996328.

[70] H. De Gersem, K. Hameyer and T. Weiland, "Skew interface conditions in 2-D finite-element machine models," in *IEEE Transactions on Magnetics*, vol. 39, no. 3, pp. 1452-1455, May 2003, doi: 10.1109/TMAG.2003.810543.

[71] Y. S. Chen, Z. Q. Zhu and D. Howe, "Calculation of d- and q-axis inductances of PM brushless ac machines accounting for skew," in *IEEE Transactions on Magnetics*, vol. 41, no. 10, pp. 3940-3942, Oct. 2005, doi: 10.1109/TMAG.2005.854976.

[72] G. Qi, J. T. Chen, Z. Q. Zhu, D. Howe, L. B. Zhou and C. L. Gu, "Influence of Skew and Cross-Coupling on Flux-Weakening Performance of Permanent-Magnet Brushless AC Machines," in *IEEE Transactions on Magnetics*, vol. 45, no. 5, pp. 2110-2117, May 2009, doi: 10.1109/TMAG.2009.2013244.

[73] P. Lazari, B. Sen, J. Wang and X. Chen, "Accurate \(d\) – \({q}\) Axis Modeling of Synchronous Machines With Skew Accounting for Saturation," in *IEEE Transactions on Magnetics*, vol. 50, no. 11, pp. 1-4, Nov. 2014, Art no. 8105704, doi: 10.1109/TMAG.2014.2327918.

[74] H. Chen, C. Hsu and D. Chang, "Position sensorless control for five-phase permanent-magnet synchronous motors," *2014 IEEE/ASME International Conference on Advanced Intelligent Mechatronics*, Besacon, 2014, pp. 794-799, doi: 10.1109/AIM.2014.6878176.

[75] L. Parsa and H. A. Toliyat, "Sensorless Direct Torque Control of Five-Phase Interior Permanent-Magnet Motor Drives," in *IEEE Transactions on Industry Applications*, vol. 43, no. 4, pp. 952-959, July-aug. 2007, doi: 10.1109/TIA.2007.900444.

[76] G. Fabri, C. Olivieri and M. Tursini, "Observer-based sensorless control of a five-phase brushless DC motor," *The XIX International Conference on Electrical Machines - ICEM 2010*, Rome, 2010, pp. 1-6, doi: 10.1109/ICELMACH.2010.5607818.

[77] C. Olivieri, G. Fabri and M. Tursini, "Sensorless control of five-phase brushless DC motors," *2010 First Symposium on Sensorless Control for Electrical Drives*, Padova, 2010, pp. 24-31, doi: 10.1109/SLED.2010.5542805.

[78] A. M. Tabrizchi, J. Soltani, J. Shishehgar and N. R. Abjadi, "Direct torque control of speed sensorless five-phase IPMSM based on adaptive input-output feedback linearization," *The 5th Annual International Power Electronics, Drive Systems and Technologies Conference (PEDSTC 2014)*, Tehran, 2014, pp. 43-48, doi: 10.1109/PEDSTC.2014.6799341.

[79] J. L. R. Martinez, R. S. Arashloo, M. Salehifar, and J. M. Moreno, "Predictive current control of outer-rotor five-phase BLDC generators applicable for off-shore wind power plants," *Electric Power Systems Research*, vol. 121, pp. 260-269, 4// 2015.

[80] S. Bolognani, R. Oboe and M. Zigliotto, "Sensorless full-digital PMSM drive with EKF estimation of speed and rotor position," in *IEEE Transactions on Industrial Electronics*, vol. 46, no. 1, pp. 184-191, Feb. 1999, doi: 10.1109/41.744410.

[81] D. Janiszewski, "Extended Kalman Filter Based Speed Sensorless PMSM Control with Load Reconstruction," *IECON 2006 - 32nd Annual Conference on IEEE Industrial Electronics*, Paris, 2006, pp. 1465-1468, doi: 10.1109/IECON.2006.347852.